University of Kentucky
UKnowledge

Theses and Dissertations--Earth and Environmental Sciences

Earth and Environmental Sciences

2021

Timing of Regional Metamorphism in the Inner Piedmont and Blue Ridge of North Carolina: Evidence From Monazite U-Pb Geochronology

Nicholas Edwin Powell
University of Kentucky, nepowell97@gmail.com
Author ORCID Identifier:
https://orcid.org/0000-0003-3654-8759
Digital Object Identifier: https://doi.org/10.13023/etd.2021.333

Right click to open a feedback form in a new tab to let us know how this document benefits you.

Recommended Citation

Powell, Nicholas Edwin, "Timing of Regional Metamorphism in the Inner Piedmont and Blue Ridge of North Carolina: Evidence From Monazite U-Pb Geochronology" (2021). *Theses and Dissertations--Earth and Environmental Sciences*. 88.
https://uknowledge.uky.edu/ees_etds/88

This Master's Thesis is brought to you for free and open access by the Earth and Environmental Sciences at UKnowledge. It has been accepted for inclusion in Theses and Dissertations--Earth and Environmental Sciences by an authorized administrator of UKnowledge. For more information, please contact UKnowledge@lsv.uky.edu.

STUDENT AGREEMENT:

I represent that my thesis or dissertation and abstract are my original work. Proper attribution has been given to all outside sources. I understand that I am solely responsible for obtaining any needed copyright permissions. I have obtained needed written permission statement(s) from the owner(s) of each third-party copyrighted matter to be included in my work, allowing electronic distribution (if such use is not permitted by the fair use doctrine) which will be submitted to UKnowledge as Additional File.

I hereby grant to The University of Kentucky and its agents the irrevocable, non-exclusive, and royalty-free license to archive and make accessible my work in whole or in part in all forms of media, now or hereafter known. I agree that the document mentioned above may be made available immediately for worldwide access unless an embargo applies.

I retain all other ownership rights to the copyright of my work. I also retain the right to use in future works (such as articles or books) all or part of my work. I understand that I am free to register the copyright to my work.

REVIEW, APPROVAL AND ACCEPTANCE

The document mentioned above has been reviewed and accepted by the student's advisor, on behalf of the advisory committee, and by the Director of Graduate Studies (DGS), on behalf of the program; we verify that this is the final, approved version of the student's thesis including all changes required by the advisory committee. The undersigned agree to abide by the statements above.

Nicholas Edwin Powell, Student

Dr. J. Ryan Thigpen, Major Professor

Dr. Michael M. McGlue, Director of Graduate Studies

TIMING OF REGIONAL METAMORPHISM IN THE INNER PIEDMONT AND BLUE RIDGE OF NORTH CAROLINA: EVIDENCE FROM MONAZITE U-PB GEOCHRONOLOGY

THESIS

A thesis submitted in partial fulfillment of the
requirements for the degree of Master of Science in the
College of Arts and Sciences
at the University of Kentucky

By

Nicholas Edwin Powell

Lexington, Kentucky

Director: Dr. J. Ryan Thigpen, Associate Professor of Geology

Lexington, Kentucky

2021

Copyright © Nicholas Edwin Powell 2021
https://orcid.org/0000-0003-3654-8759

ABSTRACT OF THESIS

TIMING OF REGIONAL METAMORPHISM IN THE INNER PIEDMONT AND BLUE RIDGE OF NORTH CAROLINA: EVIDENCE FROM MONAZITE U-PB GEOCHRONOLOGY

Channel and escape flow, or lower crustal ductile flow and redirection from orogen-normal to orogen-parallel flow, are among the most impactful concepts introduced to explain shortening accommodation in large, hot orogens. In the Inner Piedmont (IP), southern Appalachians, channel and escape flow were proposed to have occurred during the Neo-Acadian (376–340 Ma) orogeny. However, the polymetamorphic history of the southern Appalachians makes it difficult to isolate thermal and deformational events for process-focused studies necessary to test these ideas in the IP. To address this, we used *in situ* laser ablation split stream (LASS) monazite U-Pb geochronology alongside new garnet chemical data and existing P-T-t data to define the footprints of Paleozoic metamorphism in the southern Appalachians. Eastern Blue Ridge (BR) data indicate primarily Taconic (~458 Ma) with secondary Neo-Acadian metamorphism (373–335 Ma) whereas the western IP shows only Neo-Acadian metamorphism (~356 Ma). This indicates that the Brevard fault zone (BFZ) was a thermal and potentially rheological boundary during Neo-Acadian metamorphism, supporting earlier interpretations that the BFZ acted as a buttress to channel flow. Additionally, the southeastern IP records mostly Neo-Acadian (380–350 Ma) and secondary Alleghanian (339–325 Ma) metamorphism, allowing each orogenic event to be spatially separated.

KEYWORDS: Inner Piedmont, monazite geochronology, southern Appalachians, Neoacadian, Alleghanian, Taconic

Nicholas Edwin Powell

(Name of Student)

08/04/2021

Date

TIMING OF REGIONAL METAMORPHISM IN THE INNER PIEDMONT AND BLUE RIDGE OF NORTH CAROLINA: EVIDENCE FROM MONAZITE U-PB GEOCHRONOLOGY

By

Nicholas Edwin Powell

Dr. J. Ryan Thigpen

Director of Thesis

Dr. Michael M. McGlue

Director of Graduate Studies

08/04/2021

Date

ACKNOWLEDGEMENTS

This thesis is the culmination of my research throughout the two years I have spent completing my master's degree at the University of Kentucky, however this contribution would not have been possible if not for a number of people. First, my advisor Dr. J. Ryan Thigpen has been an immense help in not only the quality of my writing and science in this thesis, but also to my quality of life as a graduate student. Without the encouragement, teaching, and guidance Ryan offered me over the course of the past two years, I certainly would not have achieved nearly as much as I have. I would also like to greatly thank my committee members Dr. Dave P. Moecher and Dr. Harold H. Stowell for all of their insight, help with instrument use, and assistance with metamorphic interpretations. Beyond this, I also extend my thanks to Arthur J. Merschat from the USGS for joining us on field sampling trips, providing one of the samples in this study, and for his help with data interpretation. Importantly, this work was supported financially by the National Science Foundation (NSF-EAR-1802730), which was instrumental to my success as a graduate student.

My thanks go out to the numerous graduate and undergraduate friends and colleagues in the UK Structure and Geodynamics research group for their moral support and advice. However, I want to give particular thanks to Brandon Spencer, who has not only been a great friend and mentor, but also a significant help to much of the work in the field and in the lab that made this thesis possible. I would also like to thank my roommate throughout graduate school, Taylor Arrowood, for helping me talk through research problems. Finally, I would like to thank my family who have all been there for me to keep my mental health up and who have supported me over the past two years.

TABLE OF CONTENTS

ACKNOWLEDGEMENTS..... iii

TABLE OF CONTENTS.....iv

LIST OF TABLES.....v

LIST OF FIGURES..... vi

LIST OF ADDITIONAL FILES..... viii

CHAPTER 1. INTRODUCTION & BACKGROUND.....1

1.1 Introduction.....1
1.2 Background.....4
1.2.1 Channel and escape flow in the Himalayas and Inner Piedmont..... 4
1.2.2 Tectonic setting..... 6
1.2.3 Metamorphic and deformational conditions in the interpreted channel.....10

CHAPTER 2. METHODS.....20

2.1 Overview..... 20
2.2 Laser ablation split stream (LASS) geochronology..... 20
2.3 Garnet chemical analyses..... 22

CHAPTER 3. RESULTS.....26

3.1 Chattahoochee-Holland Mountain-Gossan Lead thrust sheet..... 26
3.2 Brevard fault zone..... 28
3.3 Brevard thrust sheet.....29
3.4 Sauratown Mountains window.....30
3.5 Brindle Creek thrust sheet..... 31

CHAPTER 4. DISCUSSION & CONCLUSIONS.....83

4.1 Interpretation of age data.....83
4.2 Integration of LASS results with P-T-t data.....85
4.3 Implications for the significance of the Brevard fault zone..... 92
4.4 Southern Appalachian channel flow..... 94
4.5 Future research..... 95
4.6 Conclusions..... 96

REFERENCES..... 98

VITA.....111

LIST OF TABLES

Table 1 Summary of sample locations, analyses, and ages.....23

LIST OF FIGURES

Figure 1.1 Model of channel flow initiation..... 13
Figure 1.2 GPS velocity vector data capturing escape flow..... 15
Figure 1.3 Magnetotelluric survey results of the Tibetan Plateau..... 16
Figure 1.4 Magnetotelluric survey results of the Tibetan Plateau..... 17
Figure 1.5 Regional map of the southern Appalachians..... 18
Figure 2.1 Simplified geologic map of the southern Appalachians.....25
Figure 3.1 SK440 mineralogy and texture photomicrographs.....35
Figure 3.2 SK440 monazite SEM backscatter electron images.....36
Figure 3.3 SK440 colorized monazite zoning images and ages..... 37
Figure 3.4 SK440 KDE, concordia diagram, and weighted mean.....39
Figure 3.5 SK440 monazite REE plots.....40
Figure 3.6 BR-20-10 mineralogy and texture photomicrographs.....41
Figure 3.7 BR-20-10 colorized monazite zoning images and ages..... 43
Figure 3.8 BR-20-10 monazite SEM backscatter electron images.....45
Figure 3.9 BR-20-10 concordia diagram and KDE..... 46
Figure 3.10 BR-20-10 weighted means..... 47
Figure 3.11 BR-20-10 monazite REE plots.....48
Figure 3.12 BR-20-14 mineralogy and texture photomicrographs.....49
Figure 3.13 BR-20-14 garnet photomicrographs and SEM images.....50
Figure 3.14 BR-20-14 monazite SEM backscatter electron images.....51
Figure 3.15 BR-20-14 colorized monazite zoning images and ages..... 52
Figure 3.16 BR-20-14 KDE, concordia diagram, and weighted mean.....53
Figure 3.17 BR-20-14 monazite REE plots.....54
Figure 3.18 IP-18-05 mineralogy and texture photomicrographs.....55
Figure 3.19 IP-18-05 garnet compositional maps and traverse data.....56
Figure 3.20 IP-18-05 colorized monazite zoning images and ages..... 57
Figure 3.21 IP-18-05 KDE, concordia diagram, and weighted mean.....59
Figure 3.22 IP-18-05 monazite REE plots.....60
Figure 3.23 IP-20-19 mineralogy and texture photomicrographs.....61
Figure 3.24 IP-20-19 hand sample.....62
Figure 3.25 IP-20-19 monazite SEM backscatter electron images.....63
Figure 3.26 IP-20-19 colorized monazite zoning images and ages..... 64
Figure 3.27 IP-20-19 KDE, concordia diagram, and weighted mean.....65
Figure 3.28 IP-20-19 monazite REE plots.....66
Figure 3.29 IP-18-09 mineralogy and texture photomicrographs.....67
Figure 3.30 IP-18-09 garnet compositional maps.....68

Figure 3.31 IP-18-09 colorized monazite zoning images and ages..... 69
Figure 3.32 IP-18-09 monazite SEM backscatter electron images.....71
Figure 3.33 IP-18-09 concordia diagrams and KDE..... 72
Figure 3.34 IP-18-09 weighted means.....73
Figure 3.35 IP-18-09 monazite REE plots.....74
Figure 3.36 IP-19-01 mineralogy and texture photomicrographs.....76
Figure 3.37 IP-19-01 garnet compositional maps.....77
Figure 3.38 IP-19-01 colorized monazite zoning images and ages..... 78
Figure 3.39 IP-19-01 concordia diagrams and KDE..... 79
Figure 3.40 IP-19-01 weighted means.....80
Figure 3.41 IP-19-01 monazite REE plots.....81

LIST OF ADDITIONAL FILES

Table S1 LASS U-Pb results for all monazite analyses.....PDF 75 KB
Table S2 Monazite REE results for all analyses.....PDF 470 KB

CHAPTER 1. INTRODUCTION & BACKGROUND

1.1 Introduction

For the past two decades, the concept of long wavelength ductile flow of lower crustal material during orogenesis, or channel flow, has been widely considered as a mechanism of accommodating shortening in large hot orogens (Grujic et al., 1996; Beaumont et al., 2001; Grujic and Parrish, 2002; Beaumont et al., 2004; Jamieson et al., 2004; Cottle et al., 2015). The channel flow mechanism has been interpreted for numerous orogens worldwide, including the Himalayan-Tibetan (HT) orogen (e.g., Grujic et al., 1996, Beaumont et al., 2001; Grujic et al., 2002), the Andean orogen (e.g., Gerbault et al., 2005), the southern Appalachians (e.g., Merschat et al., 2005; Hatcher and Merschat, 2006), and the Petermann orogen (Raimondo et al., 2009). Of these, the HT system remains at the center of this discussion because the channel flow model is able to account for multiple yet seemingly unrelated observations, including: coeval thrust and normal sense motion along the Main Central Thrust and South Tibetan Detachment, respectively, an apparent inversion of metamorphic isograds in the Greater Himalayan sequence above the Main Central thrust, the presence of migmatites and anatectic granites within the Greater Himalayan sequence, and the presence of gneiss domes within the Tibetan Plateau (Beaumont et al., 2001).

Numerical models showed that orogen-normal crustal channel flow in large hot orogens such as the HT system could be driven by the interplay between melt-weakened crust, long-wavelength gradients in gravitational potential energy beneath the growing orogenic plateau, and intense erosion at the topographic break between the plateau and the foreland (Fig. 1.1; Beaumont et al., 2004; Jamieson et al., 2004). Notably, motion along both the Main Central thrust and the South Tibetan detachment, which are interpreted to bound the channel complex, may have ceased by 15 Ma, leading to the interpretation that surficial extrusion of the channel stopped between ~22 and ~12 Mya (Searle and Szulc, 2005; Hodges, 2006; Cottle et al., 2007; Cottle et al., 2015). Furthermore, recent motion along the Main Boundary and Main Frontal thrusts indicates that more recent shortening accommodation has transitioned to a deformation process more akin to critical wedge deformation in the HT system (Avouac, 2015). To account for this in numerical models of channel flow, Beaumont et al. (2004) implemented a

substantial and rapid decrease in erosion rates at the modeled topographic break, which in turn led to cessation of channel flow.

Despite an interpreted lack of channel extrusion in the past 15 Ma in the HT system, magnetotelluric data show the presence of low resistivity material that is interpreted as partially molten crust beneath the modern Tibetan Plateau, indicating that likely melt-weakened crust remains at depth (Unsworth et al., 2005). Furthermore, GPS data and magnetotelluric data from eastern Tibet indicate active east- to southeast-directed motion of upper crustal material presumed to be linked with lower crustal flow on the southeastern margin of the Tibetan Plateau (Fig. 1.2), a possible indicator that channel material that has been redirected from orogen-normal to orogen-parallel flow after the end of channel extrusion along the Himalayan front – a process termed "escape" flow (Clark and Royden, 2000; Zhang et al., 2004, Clark et al., 2005; Royden et al., 2008; Bai et al., 2010; Zhang et al., 2010). Despite this, critical components and questions related to an "escape" flow hypothesis remain unresolved, including: 1) what conditions or mechanisms are necessary to facilitate a transition from orogen-normal channel flow to critical wedge dynamics as the primary method of accommodating shortening, 2) are these same conditions responsible for driving the onset of orogen-parallel escape flow, and 3) what characterizes these boundary conditions and how do they interact with orogen-parallel flow mechanics? Addressing these questions requires a closer examination of each component in the system, including the rheologically weak crustal escape flow channel, the buttress that prevents surface extrusion and drives flow deflection (the frontal critical wedge thrust stack?), and the structurally overlying "lid"; however, each of these components is either mostly or almost entirely buried in the HT system which precludes such an investigation. It is necessary, then, to examine a similar system, albeit with the orogenic "lid" removed.

Hatcher and Merschat (2006) suggested that the southern Appalachian IP may have experienced crustal escape flow during Neoacadian (376-340 Ma) orogenesis. The observations of that study that lead to this interpretation include: (1) an apparent inversion of metamorphic grade across the structurally lower parts of the IP (channel), culminating in a large swath of sillimanite grade metamorphism in the orogenic core, (2)

extensive migmatization and synorogenic anatectic granitic intrusions throughout the central IP (channel), and (3) a macroscopic curved mineral lineation pattern defined by aligned high-grade mineral assemblages such as sillimanite that may indicate a transition towards southwest-directed escape flow. Most importantly, the IP is currently exhumed to a much deeper structural level than the modern HT system, and so if it is in fact an exhumed channel, it would serve as an ideal location to examine the escape flow hypothesis. However, the southern Appalachians have experienced a complex polyorogenic history, with three major Paleozoic orogenic events (Taconic, Neoacadian, Alleghanian) producing complex deformational and metamorphic histories that must be unraveled. Therefore, in order to determine if the IP is indeed a potential exhumed channel, it is necessary to first resolve the complex *P-T-t* histories that have been experienced by these terranes.

In this contribution, we present new monazite LASS U-Th-Pb ages and trace element data that are integrated with new and previously reported hornblende $^{40}Ar/^{39}Ar$ ages (Levine et al., 2018, 2020; Spencer et al., 2021) and *P-T* data (Davis, 1993; Yanagihara, 1994; Bier et al., 2002; Merschat and Kalbas, 2002; Merschat, 2003; Wilson, 2006; Gatewood, 2007; Gilliam 2010) from multiple structural levels throughout the southern Appalachian IP and central-eastern BR, inferred to represent the advancing channel and foreland buttressing components of this system, respectively. Specifically, these data are intended to constrain any "footprints" of the Taconic, Neoacadian, and Alleghanian orogenies in the IP and eastern Blue Ridge study area. Though previously published studies have applied similar methods to various individual locations within the Appalachians, this study will integrate LASS data into a synthesis of IP and BR metamorphism, which provides the unique ability to discriminate diagnostic chemical processes in the petrogenetic assemblage. This should allow for the direct association of monazite ages with specific prograde and retrograde metamorphic reactions and melting events, thereby allowing for geochronologic interpretations that have not been possible before in this region, allowing us to better define the extent and magnitude of these metamorphic events and more clearly determine their overprinting relationships.

1.2 Background

1.2.1 Channel and escape flow in the Himalayas and Inner Piedmont

The channel flow concept was first applied to the HT orogen by Nelson et al. (1996) after INDEPTH seismic imaging indicated a possible large mass of partially molten crust beneath southern Tibet. Grujic et al. (1996) demonstrated simultaneous motion along the Main Central thrust and the South Tibetan detachment and used these findings to suggest that the Greater Himalayan sequence is channel material that is being extruded, causing coeval motion of these two structures. In a groundbreaking modeling effort, Beaumont et al. (2001, 2004) and Jamieson et al. (2004) used coupled thermal-mechanical models to propose that melt-weakened lower crustal material in the collision zone became mobilized by long wavelength gradients in gravitational potential energy and flowed toward the HT topographic break, linking channel extrusion to surface denudation at the Himalayan front. In the HT1 model of Beaumont et al. (2004) and Jamieson et al. (2004), heating of the thermally-blanketed overthickened crust leads to channel flow initiation after 30 Myr of collision, and this process remains active for 24 Myr before Miocene to recent reduction in denudation rate stops surface-directed channel extrusion. In this modeling, channel material required an effective viscosity reduction to $\leq 10^{19}$ Pa·s to form a well-developed channel, which those studies interpreted to result from the addition of small partial melt percentages within the channel. To do this, the modeled channel material had to reach temperatures of 700 – 750 °C, leading to the interpretation that crustal anatexis and migmatization ultimately facilitates channel flows (Beaumont et al., 2004).

In the HT1 model, two zones with contrasting *P-T-t* paths are developed (Beaumont et al., 2004; Jamieson et al., 2004). Towards the foreland and in front of the channel, modeled material interpreted as Lesser Himalayan sequence is buried and exhumed without reaching sufficient depth to be incorporated into the channel. This produces *P-T-t* paths with maximum *P-T* of ~740 °C and ~7.6 kbar just outside the channel, decreasing with distance and short residence times of ~10 Myr just outside the channel, decreasing with distance (Jamieson et al., 2004). In comparison, the channel material, interpreted to represent the Greater Himalayan Sequence, is predicted by the

models to reach much higher maximum *P-T* conditions of ~830 °C and ~13.3 kbar, longer residence times at high-*T* of ~20 m.y., and near isothermal decompression (Jamieson et al., 2004). These model predictions may be key diagnostic indicators for determining whether or not the channel flow model is suitable for this system and others.

A key challenge for the channel flow model is its apparent cessation and/or redirection during the Miocene, which is inferred from studies that examine the timing of slip along the STD and MCT. In the Dzakaa Chu section of the STD, motion is interpreted to be complete by ~20 Ma, as leucogranites of that age post-date normal-sense mylonitic fabrics (Cottle et al., 2007). Further east, Edwards and Harrison (1997) reported metamorphic U-Th-Pb zircon ages as young as 12.5 ± 0.4 Ma from a leucogranite cut by the STD, constraining this as either the most recent recorded ductile motion or the earliest brittle motion of the STD. Catlos et al. (2001) suggest that the most recent motion of the MCT was also during the late Miocene.

Although this documented Miocene to Recent inactivity on the MCT and STD indicates that orogen-normal channel flow may no longer be occurring, magnetotelluric data show the presence of substantial low resistivity material present beneath the southern Tibetan Plateau (Fig. 1.3), suggesting that the partially molten channel may remain at depth (Unsworth et al., 2005). Clark and Royden (2000) proposed that this melt-weakened crustal material was "escaping" eastward from underneath the weight of the Tibetan plateau, a concept that is supported by GPS velocity data showing ESE-directed motion of the southeastern Tibetan Plateau relative to Eurasia (Fig. 1.2; Zhang et al., 2004; Clark et al., 2005; Gan et al., 2007; Zhang et al., 2010). Additionally, magnetotelluric imaging and seismic data both suggest the presence of weak lower crustal channels underneath the southeastern Tibetan Plateau (Royden et al., 2008; Bai et al., 2010). In summary, these ideas suggest that in the Middle to Late Miocene, the channel shifted from orogen-normal to orogen-parallel escape flow. At its current exhumational level, however, the HT orogen limits studies of channel flow to using geophysical and remote sensing techniques, making it difficult to test the geodynamics, flow/deflection mechanics, and rheology of crustal material beneath Tibet.

A similar scenario has been proposed for the southern Appalachian IP (Merschat et al., 2005; Hatcher and Merschat, 2006), where the terrane is dominated by sillimanite I

(muscovite-present, potassium feldspar-absent) and sillimanite II (muscovite-absent, potassium feldspar-present) metamorphism and pervasive migmatization, indicating sufficient temperatures to facilitate widespread partial melting (Beaumont et al., 2004; Hatcher and Merschat, 2006; Merschat et al., 2017). The IP also preserves a subhorizontal lineation pattern defined by elongated sillimanite, hornblende, quartz, and muscovite that forms a curved pattern bearing N-S near the Central Piedmont suture (CPS) and curving counterclockwise to SW-NE near the Brevard fault zone (BFZ; Fig. 1.4; Merschat et al., 2005; Hatcher and Merschat, 2006). Foliation throughout the IP, which is defined primarily by micas and ribboned quartz, also dips gently to the southeast. Additionally, multiple detailed mapping studies have recognized the presence of a SW-directed imbricated thrust stack within the northern IP, which Hatcher and Merschat (2006) also attribute to the southwest directed flow of crustal material. The driver for this flow is currently interpreted to result from oblique obduction of the Carolina superterrane to the east of the IP, which would have tectonically forced melt-weakened material in the IP to escape to the southwest, with the BFZ acting as a buttress to flow and the overriding Carolina superterrane acting as a lid. If the IP is an exhumed channel that has experienced this redirection from orogen-normal to orogen-parallel flow as suggested by lineation patterns, then the IP would be an ideal location to constrain the mechanics of deformation and metamorphism in channel material.

1.2.2 Tectonic Setting

The southern Appalachians have experienced a complex metamorphic history comprising numerous orogenic pulses between the late Precambrian and Permian, including the Grenville (1.25 – 0.9 Ga), the Taconic (480 – 440 Ma), the Neoacadian (376 – 340 Ma; Merschat et al., 2017), and the Alleghanian (330 – 260 Ma; Hatcher et al., 2007). Each Paleozoic orogeny is recorded in distinct metamorphic cores in the southern Appalachians within numerous terranes that are now juxtaposed as a result of thrusting along the Blue Ridge-Piedmont megathrust and related Alleghanian thrusts during the Late Paleozoic (Hatcher, 2005; Hatcher et al., 2007; Merschat et al., 2017). The Taconic metamorphic core is located in the Blue Ridge west of the Chattahoochee-

Holland Mountain fault in southwestern NC, northern GA, and southeastern TN, and comprises a complete Barrovian sequence from chlorite to hypersthene (Eckert et al., 1989; Merschat et al., 2017). This Taconic core is discontinuous from northeast to southwest, potentially including the Hollins Line thrust sheet in northeastern Alabama (Merschat et al., 2017). The Neoacadian metamorphic core is located roughly within center of the IP and reaches sillimanite II grade metamorphism discontinuously in both western NC and central GA (Merschat et al., 2012; Merschat et al., 2017). The Alleghanian metamorphic core is located to the east of the CPS in central NC and extends northward into central VA (Russel et al., 1985). As a result of these sequential orogenic events, from the Great Smoky thrust to the CPS, provinces within the BR and IP have been amalgamated into a structural stack of east- and southeast-dipping thrust sheets and the spatial extent of metamorphism that occurred during each orogenic event is complex (Fig. 1.5). Three of these thrust sheets that are particularly key for this study, listed from northwest to southeast, include: (1) the Chattahoochee-Holland Mountain-Gossan Lead (CHMGL) thrust sheet in the eastern BR, (2) the Brevard thrust sheet in the western IP, and (3) the Brindle Creek thrust sheet in the eastern IP.

The CHMGL thrust sheet is the easternmost thrust sheet in the BR and is bound to the southeast by the BFZ and to the northwest by the Chattahoochee, Holland Mountain, Gossan Lead, and Burnsville faults (Fig. 1.4). The CHMGL consists of Neoproterozoic to Cambrian rocks of the Tallulah Falls-Ashe Formation (Hatcher, 1971; Abbott and Raymond, 1984) intruded by later Ordovician and Devonian anatectic igneous plutons (Miller et al., 2000; Hatcher, 2002; Bream, 2003; Miller et al., 2006). Structurally beneath the Tallulah Falls Formation, basement gneiss of the Toxaway and Tallulah Falls domes are preserved, as is the Grandfather Mountain window, which exposes Grenville basement rocks (Miller et al., 2006). This large expanse of Tallulah Falls-Ashe Formation rocks has been designated as the Tugaloo terrane, and is divided by the BFZ into the western Tugaloo terrane in the CHMGL thrust sheet and eastern Tugaloo terrane in the Brevard thrust sheet (Hatcher, 2002). The Tugaloo lithologies are interpreted to represent distal Laurentian equivalents of the Neoproterozoic-Cambrian rift-to-drift sequences preserved in the western and central BR (Bream et al., 2004). The CHMGL thrust sheet records evidence of all three Paleozoic orogenies. Goldberg and Dallmeyer (1997)

presented Sm-Nd and Rb-Sr garnet and hornblende ages of 472 – 451 Ma, indicating that the CHMGL thrust sheet was affected by regional metamorphism during the Ordovician. There are also several examples of magmatism from the Ordovician to the Silurian, concurrent with Taconic metamorphic ages throughout the BR and IP (Meschter McDowell et al., 2002; Miller et al., 2006; Merschat, 2009). Furthermore, eclogite near the Grandfather Mountain window yields a U-Pb zircon age of 459 +1.5/-0.6 Ma, which was interpreted to reflect the timing of eclogite-facies metamorphism during Taconic island arc subduction (Miller et al., 2010). Merschat et al. (2017) also suggested that the Acadian and Neoacadian orogenies are recorded as a protracted metamorphic event from 395 – 340 Ma with peak metamorphism limited to 375 – 358 Ma. This is supported by Dallmeyer (1988) who reported hornblende $^{40}Ar/^{39}Ar$ ages of 362 – 341 Ma. Furthermore, Trupe et al. (2003) reported U-Pb zircon crystallization ages of 377 – 360 Ma from a pegmatite that was sheared by the Burnsville fault, which they interpret as representing the most recent motion along this fault. They also propose that the Burnsville fault may correlate with the Chattahoochee fault (Trupe et al., 2003), which would place the final motion of CHMGL thrust sheet in the Neoacadian. Miller et al. (2006) obtained a crystallization age in the Rabun pluton of 335.1 ± 2.8 Ma. Because the Rabun pluton is cut by the Chattahoochee-Holland Mountain fault, Miller et al. (2006) interpret this as an indicator that the latest motion along the Chattahoochee-Holland Mountain fault was Alleghanian. Eclogite near the Grandfather Mountain window also gave rutile U-Pb ages of 335 Ma, which were interpreted as cooling following Alleghanian thrust loading (Miller et al., 2010). This may suggest motion along the Chattahoochee-Holland Mountain fault, though there is no record of Alleghanian metamorphism at the Chattahoochee-Holland Mountain fault. Also, Dallmeyer (1988) reports hornblende $^{40}Ar/^{39}Ar$ ages ranging from 333 – 322 near the Tallulah Falls dome, indicating that by the start of the Alleghanian, the CHMGL thrust sheet was cooling, either from residual Neoacadian heat or from later reheating.

The eastern border of the CHMGL thrust sheet is bound by the BFZ, which has played an important role throughout Paleozoic orogenesis in the southern Appalachians. The BFZ is interpreted to have experienced multiple deformation events, including: 1) Taconic mylonitization that occurred from 460–440 Ma (Roper and Dunn, 1973; Clark et

al., 1978; Sinha and Glover, 1978), 2) dextral motion associated with pre-Neoacadian to peak Neoacadian metamorphism (403 – 345 Ma), emplacement of the IP, and west-directed flow in the IP (Odom and Fullagar, 1973; Bond and Fullagar, 1974; Dallmeyer, 1988; Davis 1993; Hatcher, 2001; Merschat et al., 2005; Hatcher and Merschat 2006; Hatcher et al., 2017; Merschat et al., 2017), 3) dextral reactivation under lower greenschist facies conditions as a result of late Alleghanian (~280 Ma) orogenesis (Sinha et al., 1988; Hatcher, 2001; Hatcher et al., 2017), and 4) brittle dip-slip motion that occurred post-cooling during the late Alleghanian (Hatcher, 2001; Hatcher et al., 2017).

The IP lies east of the BR and extends from the Sauratown Mountains window in northwestern North Carolina to the Alabama coastal plain. It is bounded to the west by the BFZ and to the east by the CPS. The interior of the IP contains a large zone of sillimanite I and II metamorphism and has been interpreted as the core of Neoacadian metamorphism in the southern Appalachians (Wilson, 2006; Merschat et al., 2012). The IP is divided by the Brindle Creek fault zone which separates the Brevard thrust sheet of the western IP from the Brindle Creek thrust sheet of the eastern IP. Both the CHMGL thrust sheet and the Brevard thrust sheet contain Ordovician and Devonian plutons (Hatcher, 2005). Merschat et al. (2017) also report U-Pb metamorphic zircon and rim ages of 386 – 328 Ma from Poor Mountain Formation, Tallulah Falls Formation, and Hibriten mylonite throughout the Brevard thrust sheet.

The Brindle Creek thrust sheet structurally overlies the Brevard thrust sheet, and is primarily composed of biotite gneiss, sillimanite schist, and amphibolite intruded by Devonian granites (Hatcher, 2002). Rocks of the Brindle Creek thrust sheet are considered to have both a Laurentian and Gondwanan affinity, and were separated from the Laurentian terranes to the west based on differences in lithology and detrital zircon populations (Bream, 2002; Bream et al., 2004), leading the Brindle Creek thrust to be interpreted as a suture (Bream, 2002). Additionally, granitic plutons within the Brindle Creek thrust sheet are unique from those in the Brevard thrust sheet in that Ordovician plutons are only present in the Brindle Creek thrust sheet (Bream, 2002). One prominent feature in the Brindle Creek thrust sheet is the Newton window, which is located near the CPS and exposes structurally lower rocks from the underlying Brevard thrust sheet

(Gilliam, 2010). The IP as a whole is known to include rocks with three metamorphic peaks at ~360, ~345, and ~330 – 325 Ma (Gatewood, 2007; Byars, 2010; Gilliam, 2010). Gilliam (2010) interpreted peak metamorphic conditions to fall within this range followed by Alleghanian overprinting in some locations between 325 and 320 Ma. These overlap with Merschat et al. (2017), who reported U-Pb metamorphic zircon and rim ages of 391 – 300 Ma and 426 – 314 Ma for the Brindle Creek thrust sheet and Tugaloo terrane exposed in the Newton window, respectively. However, Alleghanian ages in the IP are almost exclusively reported from either near the CPS (e.g. Merschat, 2009), or in the southern IP (e.g. metamorphic zircon rims from central-eastern GA, Merschat et al., 2017).

1.2.3 Metamorphic and deformational conditions in the interpreted orogenic channel

In the channel flow interpretation for the IP, the southern Appalachian thrust sheets are comparable in metamorphism and structural position to major thrust sheets in the HT orogen. The main components of the channel flow interpretation in the HT orogen used for comparison are: (1) the Greater Himalayan sequence, which is the exhumed channel core; (2) the structurally lower Lesser Himalayan sequence, which is interpreted as Indian crust that was not incorporated into the channel; (3) the Main Central thrust which bounds the bottom of the channel; (4) the South Tibetan Detachment which separates the channel from its structural lid; and (5) the Tibetan Plateau, which overlies and buries the majority of the channel (Beaumont et al., 2001, 2004). The juxtaposed thrust sheets in the southern Appalachians can be interpreted as similar components of channel flow during the Neoacadian orogeny, as interpreted by Merschat et al. (2005) and Hatcher and Merschat (2006). (1) The Inner Piedmont comprises the channel core; (2) the CHMGL thrust sheet comprises the underlying material that did not get fully caught up into the channel; (3) the BFZ bounds the bottom of the channel akin to the Main Central thrust; (4) the CPS bounds the top of the channel similar to the South Tibetan Detachment; and (5) the Carolina Superterrane acts as the structural lid (Hatcher and Merschat, 2006). There are important differences between the channel flow interpretations in the southern Appalachian and the HT orogen, however. The most

notable examples being the curved flow pattern proposed in the IP channel and lack of normal-sense motion along the CPS (Hatcher and Merschat, 2006).

The core of the IP primarily preserves sillimanite I and II metamorphic assemblages, with kyanite to garnet grade rocks preserved at the eastern- and western-most margins (Gilliam, 2010; Merschat et al., 2012) along the BFZ and CPS, respectively. Most of the IP preserves extensive migmatization (Byars, 2008; Merschat et al., 2012) and there are a few locations, notably in the northern core of the IP, in which rocks may have locally reached granulite-facies conditions (Merschat et al., 2012). The complex history of IP deformation is reflected in the BFZ, which is interpreted to have experienced an early phase of both thrusting and dip-slip motion during the Neoacadian and near peak metamorphism in the IP (Hatcher 1972; Roper and Justus 1973; Hatcher, 2002), dextral strike-slip motion in the late Paleozoic/early Alleghanian (Reed and Bryant 1964; Edelman et al., 1987; Hatcher, 2002), and later thrust reactivation during the late Alleghanian that is associated with retrograde overprinting and brittle thrusting (e.g., the Rosman fault; Edelman et al., 1987; Hatcher, 2002).

Garnet chemical zoning patterns in the IP capture evidence of high temperature metamorphism followed by cooling. Bier et al. (2002) examined garnet from both the Brevard and Brindle Creek thrust sheets and found compositionally homogenous cores that increase in almandine and spessartine near the rims, which they suggested to be the result of decompressional, post-peak reequilibration. Bier et al. (2002) also report mean temperatures ranging from 580 – 670 °C and pressures of 5.1 and 5.3 kbar, which are interpreted to result from Neoacadian thrust faulting (metamorphic event M3 of Abbott and Raymond, 1983). Davis (1993) found similar retrograde zoning patterns in the Brevard thrust sheet, corresponding to post-peak conditions of 535 – 670 °C and 3 – 5 kbar. In the Brindle Creek thrust sheet, Merschat and Kalbas (2002) determined P-T conditions ranging from 585 – 710 °C and from 2.8 – 4.7 kbar in garnet rims, and 450 – 570 °C and 1.3 – 2.5 kbar in garnet cores, indicating prograde garnet growth along a counterclockwise curved P-T path. In the western Newton window, Gilliam (2010) reported P-T estimates of 620 – 710 °C and 4.1 – 6.3 kbar from the Cat Square terrane as well as 570 – 690 °C and 4.1 – 6.3 kbar from the lower Tallulah Falls Formation. These

high-grade conditions as well as the apparent inversion of metamorphic isograds across the IP, are similar to those found in the Greater Himalayan sequence (Beaumont et al., 2001; Hatcher and Merschat, 2006).

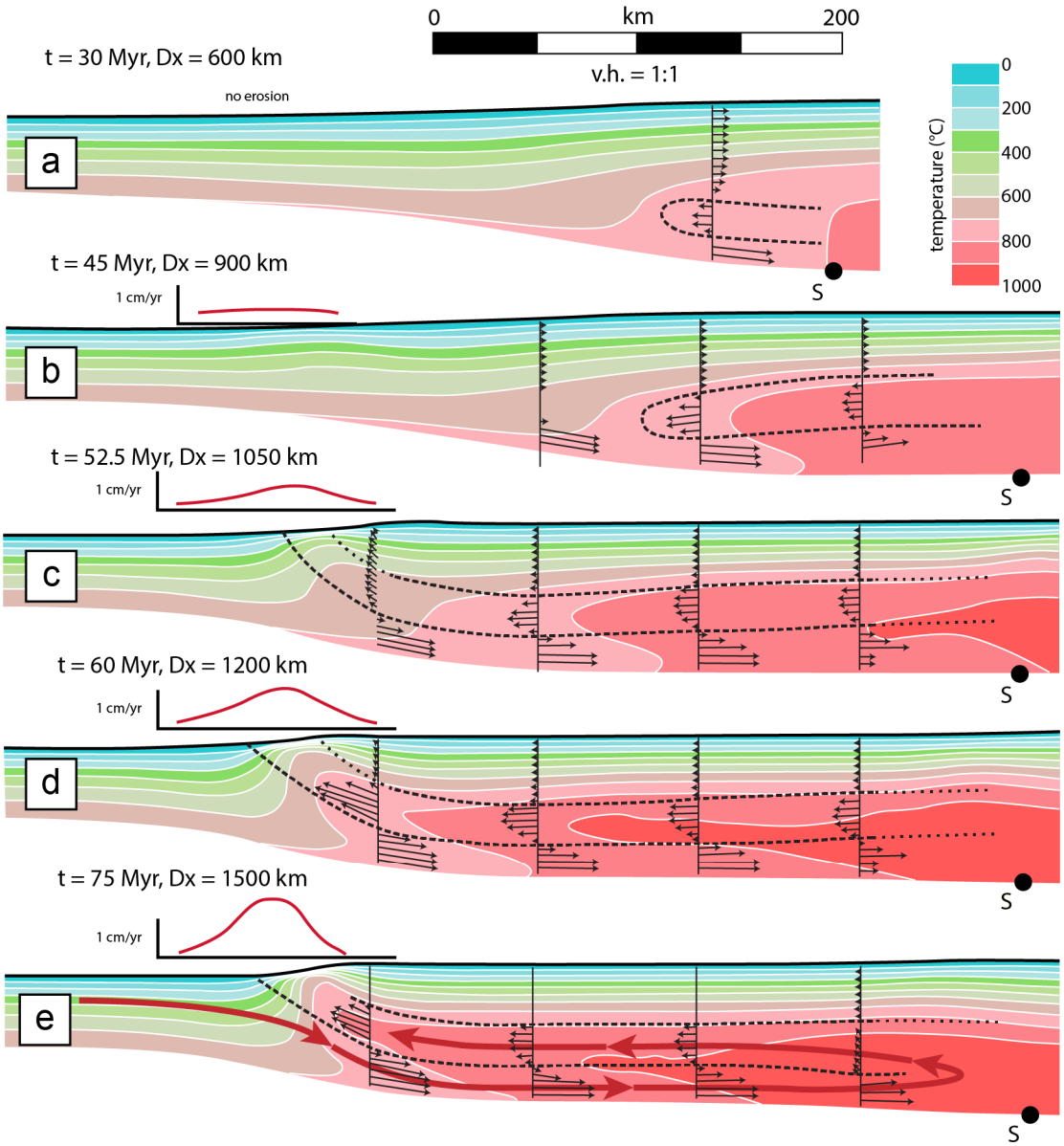
0
km
200
v.h. = 1:1
t = 30 Myr, Dx = 600 km
no erosion
a
S
temperature (°C)
0
200
400
600
800
1000
t = 45 Myr, Dx = 900 km
1 cm/yr
b
S
t = 52.5 Myr, Dx = 1050 km
1 cm/yr
c
S
t = 60 Myr, Dx = 1200 km
1 cm/yr
d
S
t = 75 Myr, Dx = 1500 km
1 cm/yr
e
S

Figure 1.1 Modified thermal-mechanical finite element model results from Beaumont et al. (2004) with a thermal field showing migration of isotherms during channel motion. Dashed black lines indicate approximate channel boundaries in each stage of the model, interpreted from instantaneous flow velocities recorded by black arrows. Inset graph shows erosion rate at each stage of the model and S represents the suture point at which mantle lithosphere breaks off and subducts. (a) The earliest stage of channel development, indicated by reversed flow velocity vectors, that forms following 30 Myr of collision, crustal thickening, and subsequent heat generation. (b) As a result of gravitational potential energy, the developing channel migrates away from the thickened crust by melt weakening the crust at the channel tip. (c) The channel continues migrating toward the surface, thinning isotherms slightly near the front of the channel. (d-e) Increased erosion in tandem with continued gravitational potential energy drives channel extrusion, establishing a well-developed channel and further compressing isotherms near the surface. In this mature channel system, collision drives lower crustal material beneath the channel which provides a steady source of material to maintain the actively flowing channel.

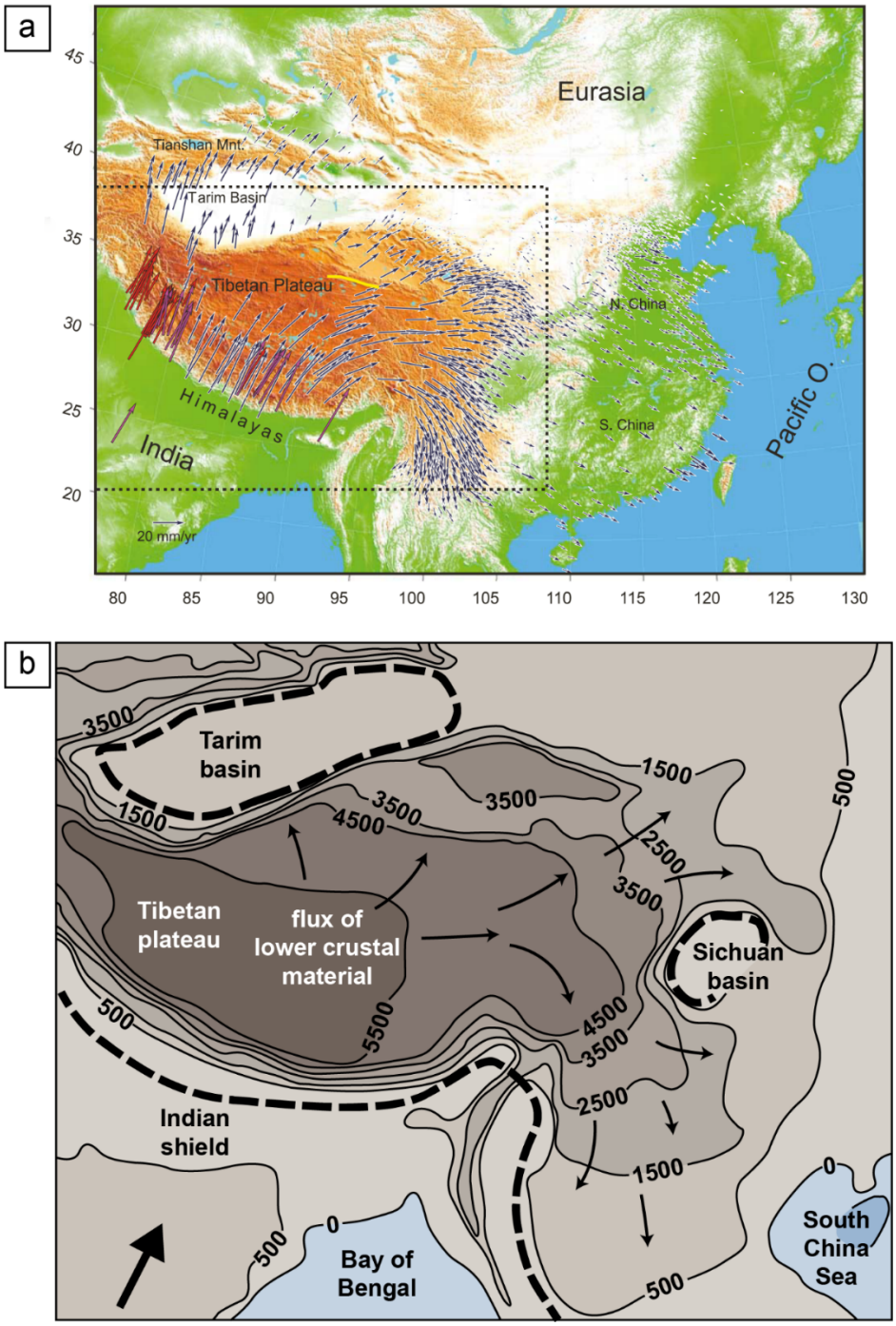

Figure 1.2 (a) GPS velocity vectors with Eurasia fixed, from Gan et al. (2007). Near the front of the HT orogen, velocity vectors show motion away from the orogen, roughly normal to the strike of the orogen. In the eastern Tibetan Plateau, velocity vectors curve from NE to E, then to the SE and S. (b) Simplified map view of the Tibetan Plateau, modified from Clark and Royden (2000), highlighting the motion of lower crustal material away from the orogen and as it is deflected to the E and SE. The outlined basins emphasize their role in hindering crustal motion, particularly near the Sichuan basin which seemingly divides the path of crustal motion.

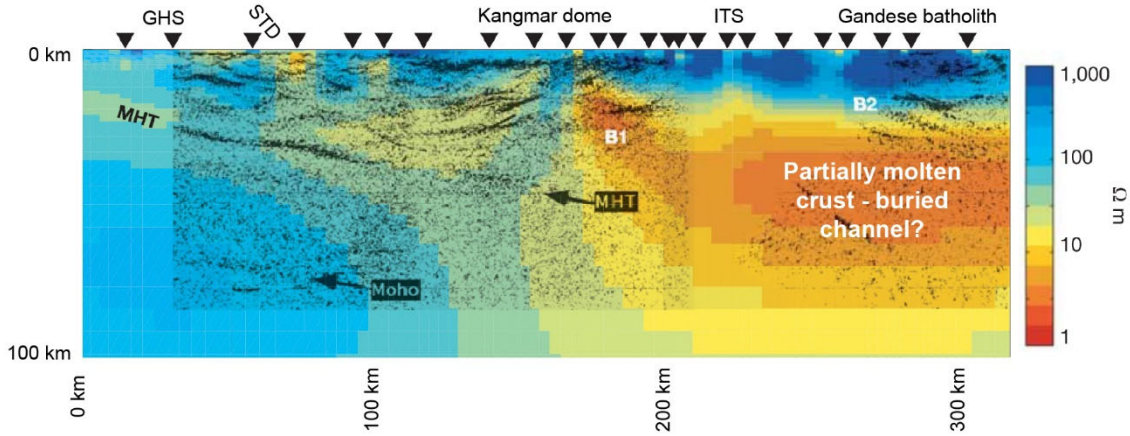

Figure 1.3 Resistivity model overlayed onto seismic profile from project INDEPTH, modified from Unsworth et al. (2005). Low resistivity layer underneath the Tibetan Plateau is interpreted as partially molten crust, which may support the presence of formerly-extruding channel material. B1 and B2 are bright spots in seismic data, which Unsworth et al. (2005) interpreted as capturing high fluid content. GHS = Greater Himalayan sequence, STD = South Tibetan detachment, MHT = main Himalayan thrust, ITS = Indus-Tsangpo suture. Inverted triangles indicate the locations of magnetotelluric stations.

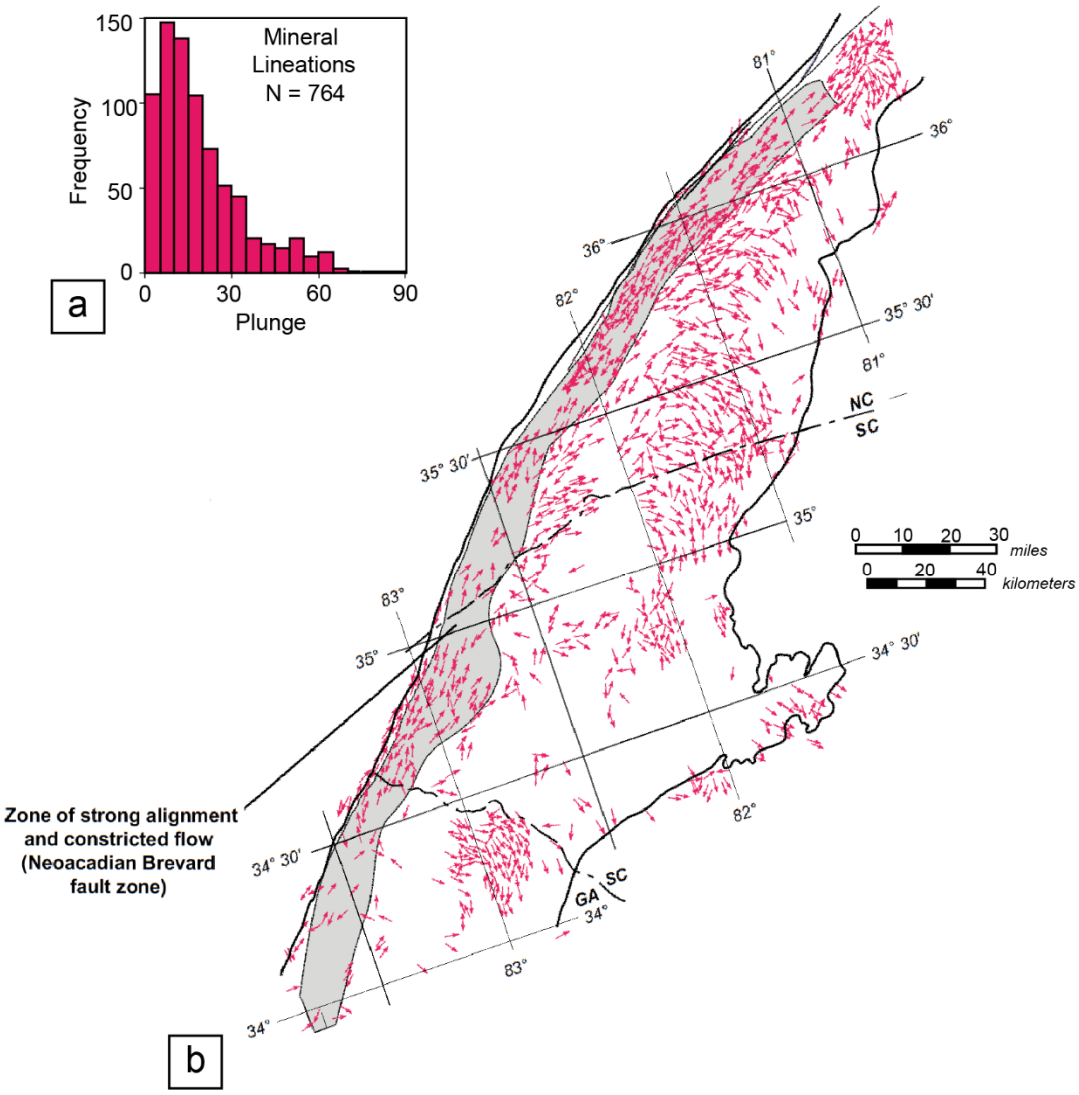

Figure 1.4 Map of the IP showing curved lineation pattern, modified from Merschat et al. (2005). (a) Histogram showing the plunge angle of all 764 lineations shown on the map. (b) Map of the IP with lineations plotted. Lineations with arrows on both ends of the line indicate horizontal plunge.

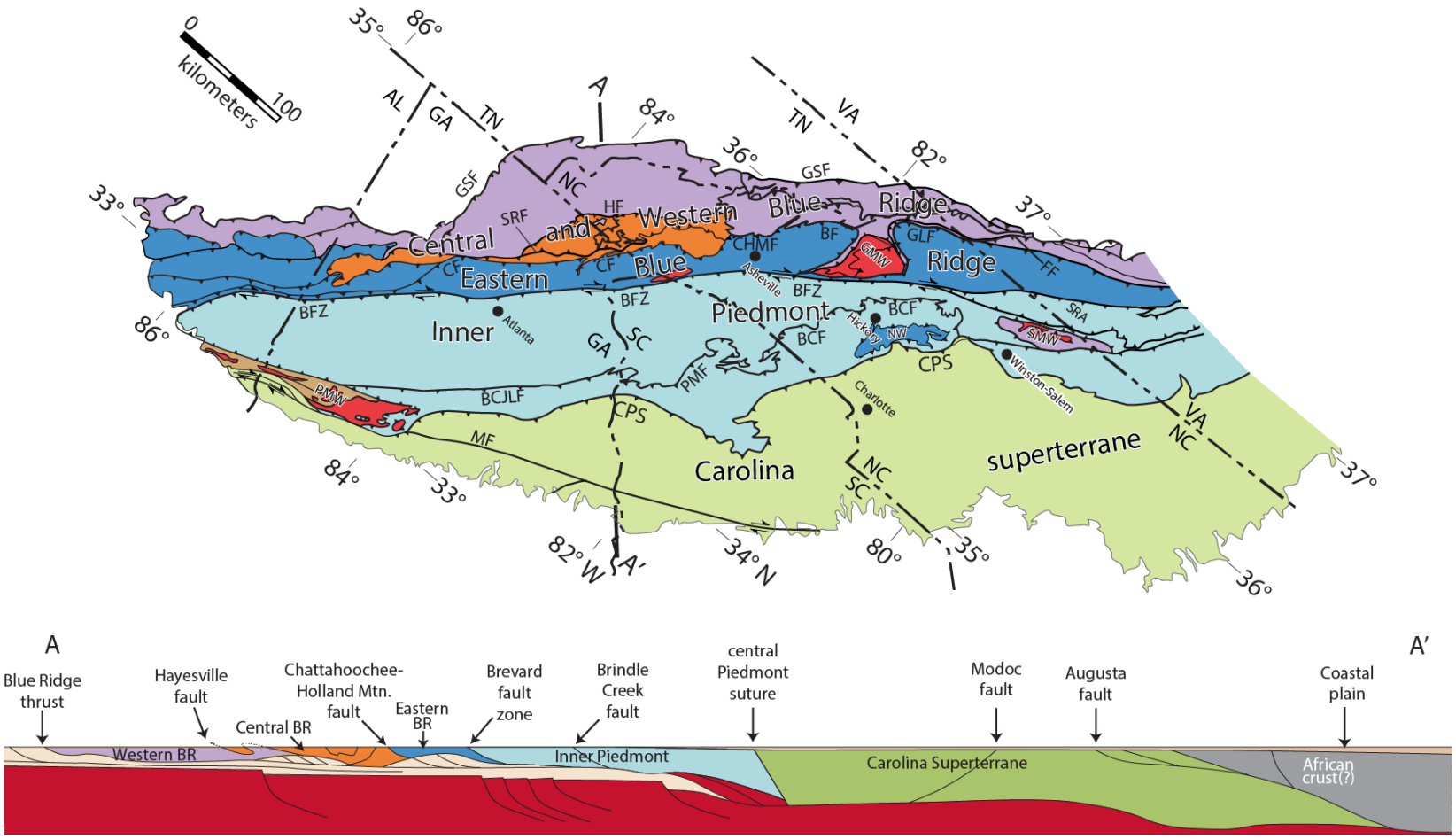
0
kilometers
100
35°
86°
AL
GA
TN
A
84°
NC
VA
TN
36°
82°
37°
33°
GSF
SRF
HF
Central
and
Western
Blue
Ridge
CHMF
BF
GLF
GMW
Ridge
FF
CF
Eastern
CF
Blue
Asheville
BFZ
BFZ
Piedmont
BCF
Hickory
NW
SRA
SMW
86°
BFZ
Inner
Atlanta
GA
SC
BCF
PMW
BCJLF
PMF
CPS
Charlotte
Winston-Salem
VA
NC
MF
CPS
Carolina
NC
SC
superterrane
37°
84°
33°
82° W
A'
34° N
80°
35°
36°

A
A'
Blue Ridge thrust
Hayesville fault
Central BR
Chattahoochee-Holland Mtn. fault
Eastern BR
Brevard fault zone
Brindle Creek fault
central Piedmont suture
Modoc fault
Augusta fault
Coastal plain
Western BR
Inner Piedmont
Carolina Superterrane
African crust(?)

Figure 1.5 Simplified regional map of the southern Appalachians and accompanying cross-section, modified from Merschat et al. (2017), denoting the boundaries of major terranes as well as the positions of major thrusts. BCF = Brindle Creek fault, BCJLF = Jackson Lake fault, BF = Burnsville fault, BFZ = Brevard fault zone, CF = Chattahoochee fault, CPS = central Piedmont suture, MF = Modoc fault zone, MPF = Paris Mountain fault, FF = Fries fault, GLF = Gossan Lead fault, GSF = Great Smoky fault, GMW = Grandfather Mountain Window, NW = Newton window, PMW = Pine Mountain window, SMW = Sauratown Mountains window, SRA = Smith River allochthon, SRF = Soque River fault. State abbreviations: VA = Virginia, TN = Tennessee, NC = North Carolina, SC = South Carolina, GA = Georgia, AL = Alabama.

CHAPTER 2. METHODS

2.1 Overview

The primary goal of this contribution is to delineate the temporal and spatial extent of metamorphism during Paleozoic orogenesis throughout the proposed southern Appalachian channel. To do this, we collected samples from each thrust sheet between the CHMGL faults and the CPS, selecting metapelitic garnet-bearing rocks for their potential to record *P-T* conditions (Fig. 2.1). Additionally, we collected samples in an attempt to form a rough transect across the interpreted channel system from the eastern border of the Brindle Creek thrust sheet into the CHMGL thrust sheet. *In situ*, high spatial resolution laser ablation split stream (LASS) U-Pb geochronology is used for this contribution because it is a powerful tool for interpreting ages in the context of deformation and metamorphism. The simultaneous collection of U-Pb isotopes and trace element geochemistry from a single spot allows ages to be directly tied to metamorphic reactions and/or the presence or absence of minerals of importance. One example that is particularly important for the purpose of this study is the use of HREE depletion to make inferences about garnet presence and growth during specific intervals of time. Each sample in this study was first examined petrographically to characterize mineralogy, texture, and fabric relationships. Any garnet present was then analyzed using electron microscopy to identify major element chemical zoning. Both of these observations are then compared to inferred garnet presence or absence using LASS data to make interpretations of the conditions and timing of metamorphism from each sample, using the context given by existing studies from similar locations and thrust sheets in the southern Appalachians.

2.2 Laser Ablation Split Stream (LASS) Geochronology

Twenty-two schist, gneiss, and amphibolite samples from throughout the Inner Piedmont and BR provinces were collected. Of these, seven were selected based on structural position and mineralogical composition to encompass the northern IP and eastern BR (Fig. 2.1, latitude and longitude in Table 1). For each sample, monazite and

xenotime grains were identified using backscatter electron detection and energy-dispersive x-ray spectroscopy using a JEOL JSM-IT100 scanning electron microscope at the University of Kentucky under an operating voltage of 15 kV. Each grain was imaged first at low contrast to determine fabric and textural relationships, then at high contrast to better show zoning and inclusions. Across the seven selected samples, 82 monazite grains and 4 xenotime grains were selected based on zoning patterns, fabric relationships, and position within each sample (matrix, garnet core, garnet rim, etc.) for LASS analysis at the University of California at Santa Barbara. Each monazite and xenotime grain was ablated using an Analyte 193 ArF laser-ablation system attached to both a Nu Instruments Plasma HR multi-collector ICP-MS to measure U-Th-Pb isotopes and a Nu Instruments AttoM single-collector ICP-MS to measure trace element abundances (Kylander-Clark et al., 2013). Spot locations for LASS analysis were selected to include as many zoning domains as possible for each monazite or xenotime grain. For each spot analysis, an 8 – 10 μm diameter area was ablated for ~11 seconds and, following the methods outlined by Kylander-Clark et al. (2013), U-Th-Pb isotopes and REE compositions were collected. Isotopes of U, Th, and Pb were used to create Tera-Wasserburg concordia diagrams of $^{238}U/^{206}Pb$ and $^{207}Pb/^{206}Pb$ ratios in the program IsoplotR, as well as kernel density estimations (KDEs) and weighted mean age plots (Vermeesch, 2018), from which best $^{238}U/^{206}Pb$ ages were calculated. For each sample, the KDE was used to visually identify age modes. In the case of multiple age modes, ages were divided into groups by visually identifying the trough of the KDE and using the corresponding age as the boundary between each age group. In all samples, each age mode was used to calculate weighted mean and concordia ages, reported at ± 1 standard deviation error. For concordia ages in samples with multiple age modes, KDEs of concordia ages were used in identifying the boundaries between age modes. For weighted means, KDEs of $^{238}U/^{206}Pb$ ages were used to identify age mode boundaries. Parameters used within IsoplotR age calculations include a ^{238}U decay constant of 0.155125×10^{-9} yr^{-1}, a ^{235}U decay constant of 0.98485×10^{-9} yr^{-1}, and a $^{238}U/^{235}U$ ratio of 137.88 (Stacey and Kramers, 1975). Errors for each analysis are reported at ± 2 standard deviations and analyses with discordance values ≥ ± 10% were not considered to improve data quality. Table S1 compiles U-Pb data and ages from all analyses, concordant and discordant, and

Table S2 compiles rare earth element (REE) data for concordant analyses. REE data were analyzed by first plotting the concentration of each REE, normalized to chondrite values from Sun and McDonough (1989) in increasing atomic weight on a spider diagram using the plotting software of Yu et al. (2019), color-coded by age, as well as by monazite zoning domain, if applicable. Additionally, plots of Ho_N/Gd_N vs concordia age were generated to show patterns in HREE enrichment relative to LREEs through time in each sample, with Ho_N and Gd_N being the concentration of Ho and Gd normalized to chondrite values from Sun and McDonough (1989). Ho was used in this case to account for the low concentrations of Tm, Yb, and Lu in many analyses, similar to the methods of Stevens et al. (2015).

2.3 Garnet Chemical Analyses

Compositional maps of Fe, Mg, Ca, and Mg and chemical traverses were collected from garnet using wavelength dispersive spectroscopy on a CAMECA SX50 electron microprobe housed at the University of Kentucky. Garnet crystals were selected based on crystal size, texture, fabric relationship, and relationship with xenotime and monazite. For compositional maps, the garnet being mapped was used to peak spectrometers on Fe, Mg, Mn, and Ca, except for instances in which the garnet produced poor Ca peaks, in which case plagioclase was used. Beam conditions used for mapping were an accelerating voltage of 15 kV and a current of 75 nA. Beam conditions used for traverse analyses were a 15 kV accelerating voltage and beam current of 25 nA. Because the resulting traverse data contained measurements of inclusions or otherwise anomalous compositional analyses, points along the traverse with weight percent oxide totals ± 3 away from 100% were removed.

Table 1 Summary of sample locations, analyses, and ages.

Sample	Latitude (°N)	Longitude (°E)	Metamorphic zone (as indicated by Merschat et al., 2017)	Number of analyses (concordant/total)	Concordant $^{238}U/^{206}Pb$ age range (Ma)	Concordia age(s), 1σ error (Ma)	Weighted mean age(s), 1σ error (Ma)
Chattahoochee-Holland Mountain-Gossan Lead thrust sheet							
SK440			sillimanite I	40/40	451-467	458.8 ± 0.8	458.2 ± 1.1
BR-20-10	36.18083	-81.39028	kyanite	80/83	329-380	338.6 ± 1.5, 359.0 ± 0.7, 377.3 ± 0.6	335.1 ± 2.0, 357.5 ± 0.9, 372.9 ± 0.8
Brevard fault zone							
BR-20-14	35.53028	-82.38417	chlorite	10/12	438-464	461.8 ± 1.9	452.8 ± 2.6
Brevard thrust sheet							
IP-18-05	36.08889	-81.17417	sillimanite I	68/73	329-375	357.9 ± 0.5	356.4 ± 0.7
Sauratown Moutnains window							
IP-20-19	36.37833	-80.36222	sillimanite I	10/12	348-376	361.5 ± 1.3	360.2 ± 1.7
Brindle Creek thrust sheet							
IP-18-09	36.0236111	-81.29777778	sillimanite II	59/67	332-413	356.7 ± 0.7, 404.5 ± 1.9	355.9 ± 0.9, 401.5 ± 2.5
IP-19-01	35.33667	-81.36036	kyanite	51*/72	322-371	332.9 ± 1.9, 369.4 ± 0.8	324.1 ± 1.5, 362.1 ± 0.7

Table 1 Summary of the latitude and longitude, total number of analyses, and resulting ages of each sample as well as the thrust sheets in which each sample is located. *Asterisk denotes the number of concordant analyses excluding those which included a significant mixture of core and rim domains.

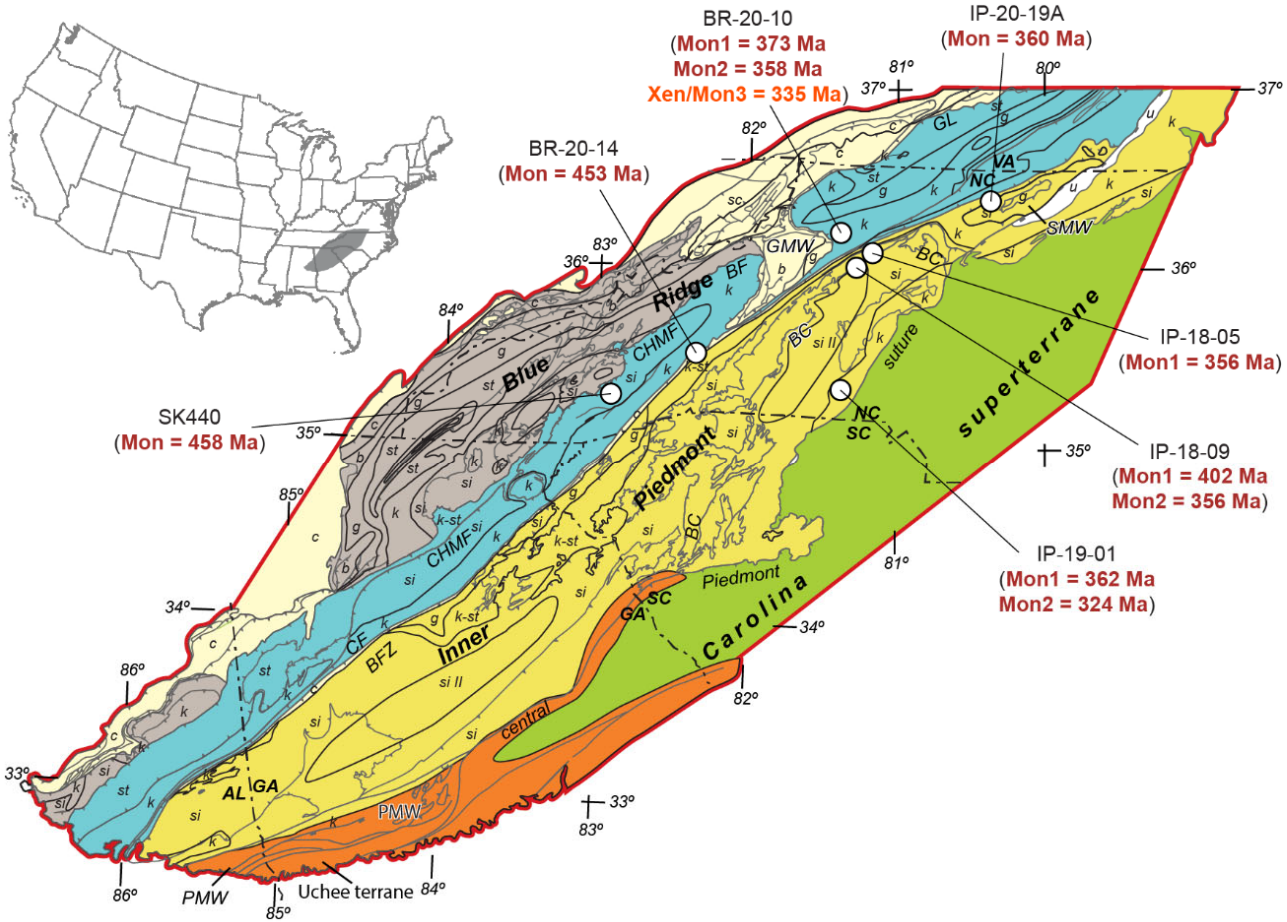

Figure 2.1 Simplified geologic map of the southern Appalachians with metamorphic isograds, sample locations, and age results. Modified from Merschat et al. (2017). BC = Brindle Creek fault, BF = Burnsville fault, BFZ = Brevard fault zone, CF = Chattahoochee fault, CHMF = Chattahoochee-Holland Mountain fault, GL = Gossan Lead fault, PMW = Pine Mountain window, SMW = Sauratown Mountains window. State abbreviations: VA = Virginia, NC = North Carolina, SC = South Carolina, GA = Georgia, AL = Alabama.

CHAPTER 3. RESULTS

3.1 Chattahoochee-Holland Mountain-Gossan Lead thrust sheet

Sample SK440 was collected from ~20 km south of Waynesville NC (Fig. 2.1) and contains the assemblage biotite + kyanite + garnet + muscovite + quartz + plagioclase + staurolite + sillimanite ± ilmenite ± zircon ± monazite (Fig. 3.1a-c). Foliation is defined primarily by parallelism of biotite and muscovite (Fig. 3.1d). Quartz and feldspar primarily occur as isolated grains surrounded by micas, though in some instances thin bands of quartz and/or plagioclase are present (Fig. 3.1a). Most of these quartz and feldspar grains appear to be free of significant post-peak metamorphic recrystallization (Fig. 3.1e). Garnet up to 2 mm in diameter is abundant in SK440 and is subhedral in shape (Fig. 3.1f). Most garnet porphyroblasts contain abundant inclusions which are composed largely of quartz in addition to less common biotite, plagioclase, sillimanite (coarse-grained and fibrous), and monazite (Fig. 3.1f, g).

Monazite is abundant and occurs inclusions in garnet and intergrown with matrix phases. Though monazite is present both within garnet and in the matrix, it is much more common as a garnet inclusion than as a matrix component, as 15 monazite grains were identified within garnet and only five grains were identified outside of garnet. Monazite included in garnet is commonly under 25 μm in greatest dimension, though in some cases can be up to 60 μm in length. Of the five monazite grains located outside of garnet, none are oriented parallel to foliation (Fig. 3.2a-c). Most matrix monazite grains as well as many larger monazite grains included in garnet are highly fractured, though some extent of this is likely an artifact of sample preparation (Fig. 3.2c-f). A total of 14 monazite grains were selected for LASS analysis, 3 of which were matrix grains. From these, 40 concordant analyses were collected, resulting in ages that range from 451 to 467 Ma (Fig. 3.3, Table 1, S1). Both matrix monazite and garnet inclusion monazite return similar age ranges that form a single age mode when plotted as a KDE that has a concordia age of 458.8 ± 0.8 Ma and a weighted mean age of 458.2 ± 1.1 Ma (Fig. 3.4, Table 1). Chondrite normalized Ho/Gd vs age plots show no age-related trends in the enrichment or depletion of HREEs in monazite (Fig. 3.5). Most analyses show varying depletion of HREEs and a negative Eu anomaly, however four analyses in particular show much more depletion in

HREEs than others (Fig. 3.5). Of these analyses strongly depleted in HREEs, three are from matrix monazite (two of which are clearly on monazite rims) and one from a monazite grain included in garnet. One of these matrix monazite grains is entirely surrounded by fractured orthopyroxene and is not close to garnet, and the other is located next to a garnet grain.

A sample of Ashe metamorphic suite (BR-20-10) was collected from the eastern BR (Fig. 2.1) that contains the assemblage quartz + muscovite + biotite + plagioclase + garnet ± monazite ± zircon ± magnetite ± graphite ± chlorite ± xenotime (Fig. 3.6a). Foliation is defined by biotite, quartz ribbons, and muscovite and lineation is defined by biotite (Fig. 3.6a, b). Muscovite is mostly medium-grained, though there are a few aggregates of finer-grained, irregular muscovite as well (Fig. 3.6c, d). Quartz and plagioclase are all medium-grained, with no finer recrystallized grains. Garnet is uncommon in this sample and ranges from 2 – 3 mm in size (Fig. 3.6e, f). Garnet is anhedral and in one grain is surrounded by quartz and biotite grains which outline a more euhedral garnet shape prior to alteration (Fig. 3.6e, f). Chlorite, interpreted to be retrograde, occurs around one garnet porphyroblast (Fig. 3.6g).

Monazite is relatively abundant and occurs included in garnet and in the matrix. Monazite within garnet is 15 – 70 μm in length and shows very slight compositional zoning whereas matrix monazite ranges from 10 – 180 μm in length and shows more prominent zoning (Fig. 3.7). Matrix monazite is mostly elongated with the long axis parallel or sub-parallel to foliation (Fig. 3.8). This is reflected in zoning patterns, aside from one monazite grain which shows a core domain that is near-perpendicular to foliation (e.g., Fig. 3.7r). Additionally, one monazite shows a clear rim domain that is present only on the long axis of the grain, parallel to foliation (Fig. 3.7f). Most monazite grains also show alteration to apatite, which has seemingly strengthened the alignment of each monazite grain with foliation by preferentially removing material from the axis of the grain perpendicular to foliation (Fig. 3.8d-f). A total of 74 concordant ages were collected from monazite and 6 from xenotime, with monazite ages ranging from 329 to 380 Ma, and xenotime ages ranging from 335 to 354 Ma (Fig. 3.9a, Table 1, S1). The KDE shows two major age modes as well as a few younger ages (Fig. 3.9b). Weighted

means were calculated for each of these age modes, and were visually separated at 343 Ma and 365 Ma based on the trough of the KDE (Fig. 3.9b, Table 1). The oldest population yields a weighted mean age of 372.9 ± 0.8 Ma, the intermediate mode yields a weighted mean of 357.5 ± 0.9 Ma, and the youngest age mode yields a weighted mean of 335.1 ± 2.0 Ma (Fig. 3.10, Table 1). The REE patterns exhibits a slight Eu anomaly, though much less pronounced than in other samples, as well as a trend of slightly depleted HREE (Fig. 3.11a, b). The degree of HREE depletion is relatively consistent among the grains, and is less than other samples in this study (Fig. 3.11a, b).

3.2 Brevard fault zone

One unoriented sample (BR-20-14) was collected from within 100 m of the BFZ (Fig. 2.1), and consists of muscovite + chlorite + quartz + garnet + plagioclase ± ilmenite ± monazite (Fig. 3.12a). Foliation and lineation in this sample are well defined by muscovite and chlorite (Fig. 3.12a, b). Muscovite is present both as fine-grained aggregates and as larger individual grains (Fig. 3.12c, d). Garnet is anhedral and typically 1-3 mm in diameter, though in many instances garnet consists of fragments of an original porphyroblast that underwent layer-parallel extension with chlorite and quartz filling the extended space between garnet fragments (Fig. 3.13). Quartz inclusions occur in many garnet grains as well as rare monazite and xenotime grains. Asymmetry is apparent in garnet pressure shadows, typically composed of quartz and chlorite, as well as by the orientation of fracturing and shearing of garnet grains (Fig. 3.13).

Monazite in the matrix of BR-20-14 is highly altered and anhedral, ranging in size from 20 – 50 μm in length aside from one grain included within a plagioclase porphyroclast (Fig. 3.14). Most grains show alteration, and many of these monazite grains are either fully aligned within the foliation, or have an original alignment with foliation captured in alteration byproducts around the monazite grain (Fig. 3.14). Only one monazite grain contains internal zoning that could be clearly observed by SEM, and contains a core and a rim domain (Fig. 3.15). Of the monazite and xenotime grains present as garnet inclusions, one monazite was large enough and internally clean enough for LASS analysis. This grain is ~15 μm in length and is free of the alteration present in

matrix monazite (Fig. 3.15). Between both matrix and garnet monazite, ten concordant ages could be obtained (Table S1). These ages range from 438 to 464 Ma and have a single peak when plotted on a KDE (Fig. 3.16). All analyses yield a concordia age of 461.8 ± 1.9 Ma and a weighted mean age of 452.8 ± 2.6 Ma (Fig. 3.16, Table 1). REE patterns in BR-20-14 show a negative Eu anomaly as well as a depletion of HREE (Fig. 3.17a). Analyses with older ages fall almost entirely within the spread of HREE abundances in younger ages, indicating that there is no correlation between age and HREE depletion (Fig. 3.17a, b).

3.3 Brevard thrust sheet

Sample IP-18-05, which is mapped as Hibriten mylonite (Gatewood 2007), was collected from the immediate footwall of the Brindle Creek fault zone (Fig. 2.1). The assemblage is quartz + plagioclase + microcline + garnet + biotite + muscovite + sillimanite ± monazite ± zircon ± ilmenite ± graphite (Fig. 3.18a, b). Foliation in this sample is largely defined by elongated quartz ribbons as well as oriented biotite and rarely muscovite or sillimanite grains (Fig. 3.18a, b). Quartz and feldspar are largely recrystallized throughout this sample, with coarser-grained microcline porphyroclasts that have been fractured and slightly sheared (Fig. 3.18c). Many of these porphyroclasts show grain boundary bulging, subgrain rotation, and undulose extinction (Fig. 3.18d-e). Garnet is sub- to anhedral and 1 to 5 mm in diameter (Fig. 3.18a, b, f, g, 25). In some instances, garnet crystals are elongated parallel to foliation or show pressure shadows composed of biotite (Fig. 3.18f-g). Most garnet crystals show alteration to biotite, though one garnet in particular shows apparent alteration to a combination of quartz, plagioclase, and biotite (Fig. 3.18g). Garnet in this sample is primarily almandine (X_{alm} = 0.79 – 0.85), with lesser components of pyrope (X_{py} = 0.06 – 0.14), spessartine (X_{spss} = 0.02 – 0.08), and grossular (X_{gr} = 0.02 – 0.04) (Fig. 3.19). Similarly to the Brindle Creek thrust sheet, garnet in this Brevard Thrust sheet sample shows homogenous cores free of any growth zoning that may have originally been present, along with thin rims (~100 to 400 μm) of increased Mn and decreased Mg, as well as increased Fe (Fig. 3.19).

Monazite is present both as garnet inclusions, where it ranges from 5 – 80 μm in length and within the matrix where it ranges from 45 – 145 μm in length (Fig. 3.20). Most matrix monazite grains are elongated and of these, the majority are parallel to foliation. There are some grains however that are elongated in an orientation cross-cutting foliation, as well as some grains that are more rounded than elongated, and exhibit no preferred fabric relationships. Most monazite grains show compositional zoning consisting of core and rim domains with further complexities within cores akin to Brindle Creek thrust sheet monazite. Additionally, some monazite grains have both outer core/mantle domains as well as inner core domains (Fig. 3.20). Monazite located within garnet, however, is free of compositional zoning.

Seventy-three LASS analyses were collected across 18 monazite grains and 1 xenotime grain in IP-18-05 (Table S1). Of these, 68 analyses produced ages that are 90-110% concordant. These analyses define a single age mode with a concordia age of 357.9 + 0.5 Ma and a weighted mean age of 356.4 ± 0.7 Ma (Fig. 3.21, Table 1). Concordant garnet inclusion monazite ages range from 351 to 375 Ma, whereas matrix monazite ages range from 338 to 371 Ma. In matrix grains with multiple zoning domains, comparatively older ages are localized toward the core domains and younger ages toward the rims. The single xenotime grain analyzed returned three concordant ages at 329 ± 15 Ma, 329 ± 10 Ma, and 338 ± 11 Ma, which, along with one monazite rim age, constitute the youngest ages obtained from this sample. All monazite analyses show a depletion in HREEs relative to LREEs, as well as a negative Eu anomaly (Fig. 3.22a). No significant correlation exists between HREE depletion and age, though monazite in garnet show very slightly less depletion of HREEs than matrix monazite (Fig. 3.22b).

3.4 Sauratown Mountains window

One sample, IP-20-19, was collected from the Sauratown Mountains window, ~11 km NE of Pilot Mountain, NC (Fig. 2.1). The assemblage is quartz + plagioclase + muscovite + garnet + microcline ± magnetite ± monazite ± zircon ± xenotime (Fig. 3.23a). Fine-grained aggregates of highly recrystallized quartz and plagioclase constitute the majority of this sample (Fig. 3.23b), with a few slightly coarser-grained quartz and

feldspar as well as some much coarser sheared feldspar porphyroclasts. Foliation is defined by elongated quartz grains and muscovite (Fig. 3.23a-d) whereas the same elongated quartz grains define lineation. Garnet is sub- to anhedral and is ~1 mm in diameter and shows serrated grain boundaries, though only one garnet grain was captured in thin section (Fig. 3.23e, f). This may not be representative of the entire sample however, because garnet is slightly more abundant in hand sample than is suggested in thin section (Fig. 3.24).

Elongated monazite is present in the matrix of this sample, and many grains are oriented with the long axis of the grain parallel or sub-parallel to foliation (Fig. 3.25). Though monazite was not observed as inclusions within garnet, the particular thin sections cut did not capture enough garnet grains to definitively state that no monazite inclusions in garnet are present in this sample. The monazite grains that were observed in the matrix were around 10 – 40 μm in length, and a few of these grains show alteration to apatite (Fig. 3.25). Additionally, most grains show complex compositional zoning patterns consisting of thin rims (< 5 μm) and 2 – 3 domains within cores (Fig. 3.26). A total of ten concordant ages were obtained from across four monazite grains which, when plotted on a KDE, show a single age mode with a concordia age of 361.5 ± 1.3 Ma and a weighted mean age of 360.2 ± 1.7 Ma (Fig. 3.27, Table 1, S1). Rare earth element patterns in these ten analyses show a negative Eu anomaly and a slight depletion in heavy REEs (Fig. 3.28), though less depletion than other samples in this study.

3.5 Brindle Creek thrust sheet

Sample IP-18-09 was collected from the immediate hanging wall of the Brindle Creek fault zone (Fig. 2.1). The assemblage is quartz + plagioclase + biotite + garnet + sillimanite + muscovite ± graphite ± pyrite ± monazite ± zircon ± xenotime, with the foliation defined by aligned biotite, muscovite, and sillimanite laths and the lineation defined by elongate sillimanite and muscovite laths (Fig. 3.29). Garnet is generally anhedral and up to 3 mm in diameter (Fig. 3.29b-e, 36). Most garnet porphyroblasts are partly altered to quartz, biotite, and plagioclase (Fig. 3.29b-e). Inclusions are abundant and, in some instances, are localized in the core of the garnet (Fig. 3.29e). Garnet cores

are largely homogenous in major element composition, however 300 to 500 μm rims are enriched in Mn, depleted in Mg, and have similar Fe and Ca relative to cores (Fig. 3.30a, b, c). Some small garnet grains show no compositional zoning and major element compositions that are roughly equivalent to the rims of larger garnet grains (Fig. 3.30b).

Monazite occurs in the matrix and as garnet inclusions in IP-18-09. Matrix monazite is typically elongated and ranges from ~30 to 100 μm (Fig. 3.31). In most cases, the long axis of the grain is oriented parallel to foliation aside from a few grains that are either rounded or are oriented with the long axis of the grain slightly oblique to foliation (Fig. 3.32). Matrix monazite exhibits complex compositional zoning that generally includes core and rim domains, and distinct mantle domains in some grains (Fig. 3.31). Monazite included in garnet is typically finer-grained than matrix monazite, ranging from 25 to 70 μm, and shows similarly complex zoning patterns (Fig. 3.31). The total range of ages from this sample falls between 332 and 413 Ma (Fig. 3.33a). Due to the thin rims of many grains and the LASS spot size (8 μm), only one concordant rim age was obtained from matrix monazite, at 332 ± 11 Ma. In matrix monazite grains that contain a definable mantle domain, mantle ages range from 340 to 370 Ma. Matrix monazite cores yield $^{206}Pb/^{238}U$ ages ranging from 342 to 411 Ma. Monazite inclusions in garnet yield slightly older ages, with cores ranging from 390 to 413 Ma, mantle domains ranging from 367 to 374 Ma, and two rim ages of 368 and 373 Ma. Two xenotime inclusions in garnet yield ages ranging from 332 Ma to 376 Ma (Fig. 3.31). A KDE histogram shows that the majority of all obtained ages fall into a single population that ranges from 332 to 376 Ma, however a small group of ages (n = 8) have a higher age range from 390 to 413 Ma (Fig. 3.33). The younger, primary age population was used to calculate a concordia age of 356.7 ± 0.7 Ma and a weighted mean of $^{206}Pb/^{238}U$ 355.9 ± 0.9 Ma (Fig. 3.33a, 3.34a, Table 1) and the older population was used to calculate a concordia age of 404.5 ± 1.9 Ma and a weighted mean of 401.5 ± 2.5 Ma (Fig. 3.33b, 3.34b, Table 1). The oldest age population consists entirely of core ages from garnet inclusions as well as core ages from a single large monazite grain (Fig. 3.31). The distribution of REEs in monazite shows that all monazites are depleted in HREEs (Fig. 3.35a, b). The Ho/Gd vs. age plot for monazite analyses in this sample shows that monazite included in garnet exhibits a depletion of HREEs in their cores from 413 to 400 Ma and a relative enrichment in

HREEs from 400 to 362 Ma (Fig. 3.35c). Matrix monazite analyses show a relative enrichment in HREE from 410 to 365 Ma, a relative depletion in HREEs from 365 to 348 Ma, and a return to slightly more enriched HREE from 348 to 330 Ma (Fig. 3.35c).

Sample IP-19-01, collected ~5 km from the CPS (Fig. 2.1), is a mylonite with the assemblage quartz + plagioclase + garnet + microcline + biotite + monazite + muscovite ± ilmenite (Fig. 3.36a, b). Foliation is largely defined by elongated quartz ribbons and aligned biotite grains (Fig. 3.36a, c). The majority of quartz and feldspar throughout this sample are comprised of small, recrystallized grains aside from coarser-grained quartz ribbons and small microcline clasts (Fig. 3.36c, d, e). Garnet ranges in size from 1 to 5 mm and is commonly sub- to anhedral (Fig. 3.36b, f). A few porphyroblasts exhibit shearing and elongation parallel to foliation (Fig. 3.36f). Additionally, in many instances, garnet is surrounded by biotite and quartz (Fig. 3.36b, f). Major element chemical analyses of garnet in this sample shows that garnet is primarily almandine with minor pyrope as well as minimal spessartine and grossular (Fig. 3.37). Growth zoning is absent from all garnet grains in this sample; instead, the majority of each grain is homogenous aside from a thin (~100 μm) rim of enriched Mn and Ca and depleted Mg (Fig. 3.37).

Monazite is abundant in the matrix of IP-19-01, and grains range from ~30 μm to 500 μm in maximum dimension (Fig. 3.36g, 3.37). The grains are typically somewhat elongated parallel to foliation with a few exceptions that are either rounded or slightly cross-cut foliation. Most monazite grains show a distinct rim domain with cores that range from being mostly homogenous to complexly zoned (Fig. 3.38). A total of 8 monazite grains in this sample were analyzed via LASS. The resulting ages can be divided into two groups based largely on compositional domains, with monazite core ages ranging from 349 to 371 Ma and monazite rim ages ranging from 319 to 329 Ma (Fig. 3.38). Most ages are within ± 10% of concordance, although some rim ages were discordant and are therefore excluded for interpretations and age calculations (Fig. 3.38). The KDE shows two peaks at ~324 Ma and ~364 Ma (Fig. 3.39). To ensure that age populations properly represent the metamorphic history captured in this sample, analyses that were located on the boundary between two monazite zoning domains were removed from consideration.

Using an age of 345 Ma to divide the two populations, the younger population of ages has a weighted mean $^{206}Pb/^{238}U$ age of 324.1 ± 1.5 Ma and a concordia age of 332.9 ± 1.9 Ma (Fig. 3.39a, 3.40a, Table 1). The older population of ages yields a weighted mean $^{206}Pb/^{238}U$ age of 362.1 ± 0.9 Ma and a concordia age of 369.4 ± 0.8 Ma (Fig. 3.39b, 3.40b, Table 1). Monazite shows depletion in HREEs along with a negative Eu anomaly (Results Fig. 3.41a, b), although rims are slightly more enriched in HREEs than cores. Plotting the ratio of chondrite-normalized Ho to Gd vs age shows a relative enrichment of HREEs in monazite over time between the recorded age range of 380 to 325 Ma (Fig. 3.41c). Additionally, monazite cores have a stronger negative Eu anomaly than monazite rims (Fig 3.41a).

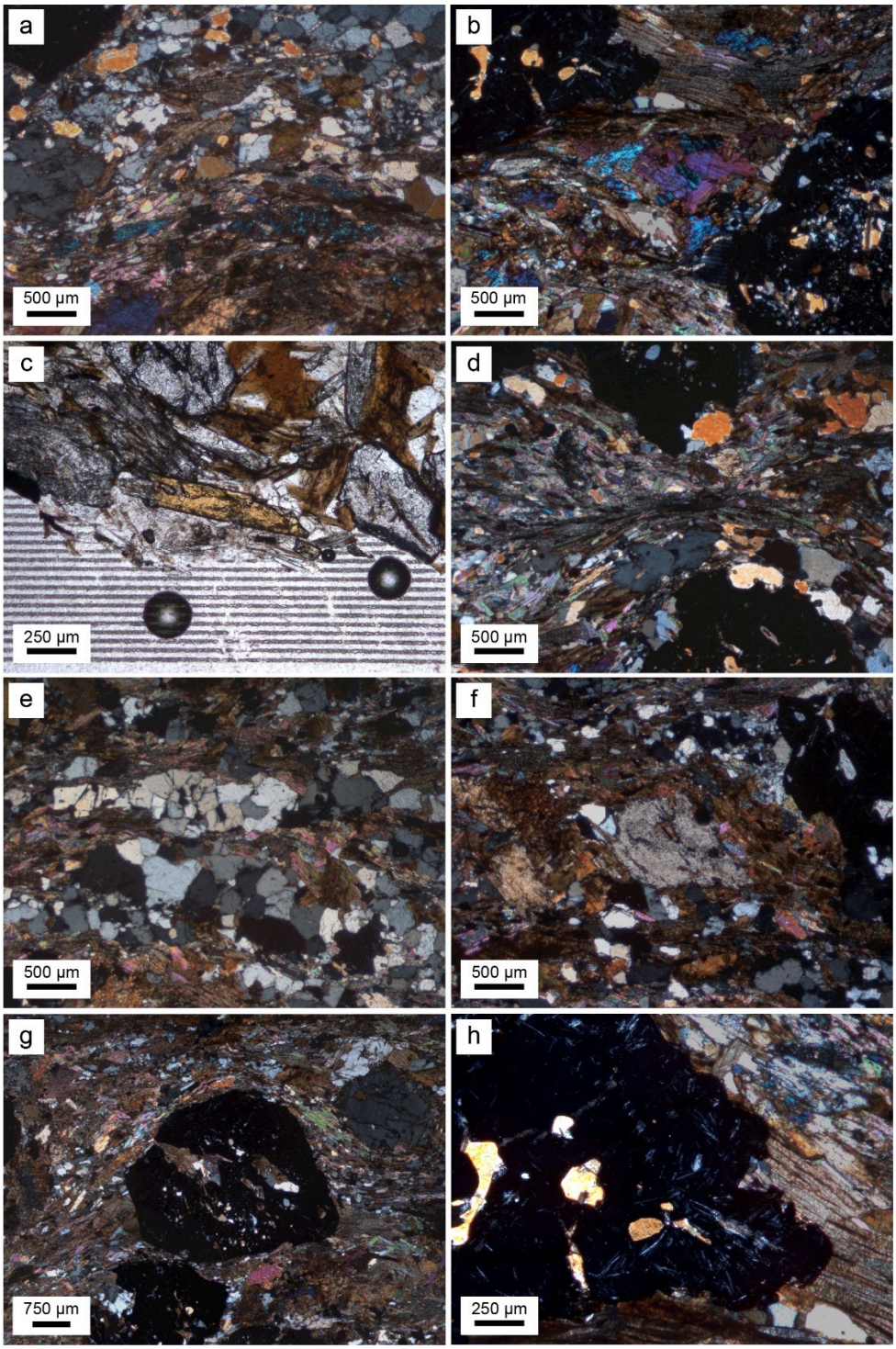

Figure 3.1 Photomicrographs from sample SK440. (a-d) Representative mineralogy and foliation. Horizontal lines clearly visible in plane-polarized light are the remnants of electron microprobe analysis. (e) Representative quartz and feldspar showing a relative lack of recrystallization compared to other samples. (f) Representative garnet with abundant inclusions and subhedral shape. (g) Garnet showing fibrous sillimanite inclusions.

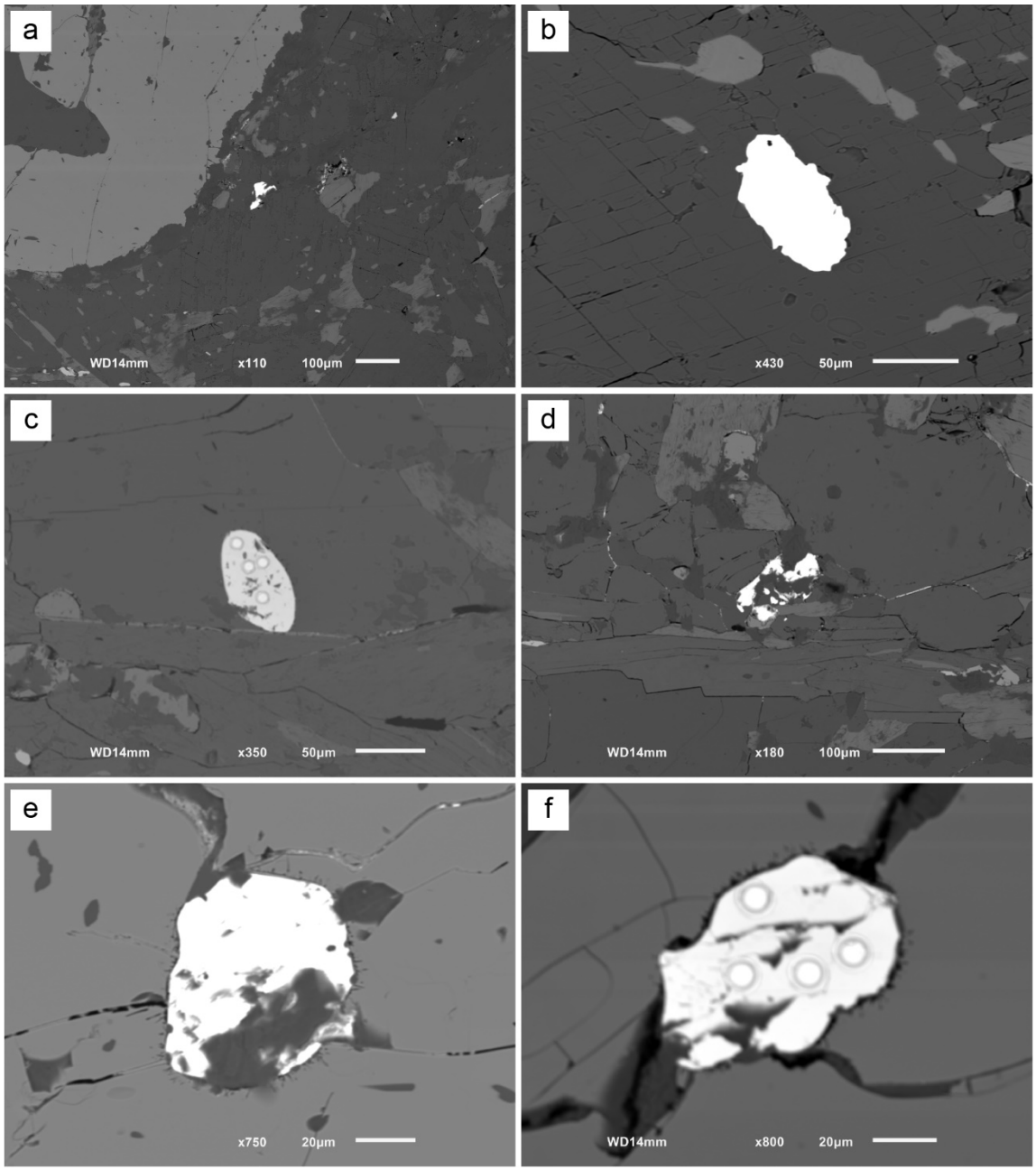

Figure 3.2 SEM backscatter electron images of monazite from SK440 showing poor alignment of the grains with foliation as well as (c-f) highly fractured, impure nature of monazite in the sample. White circles in some grains are LASS analysis spots.

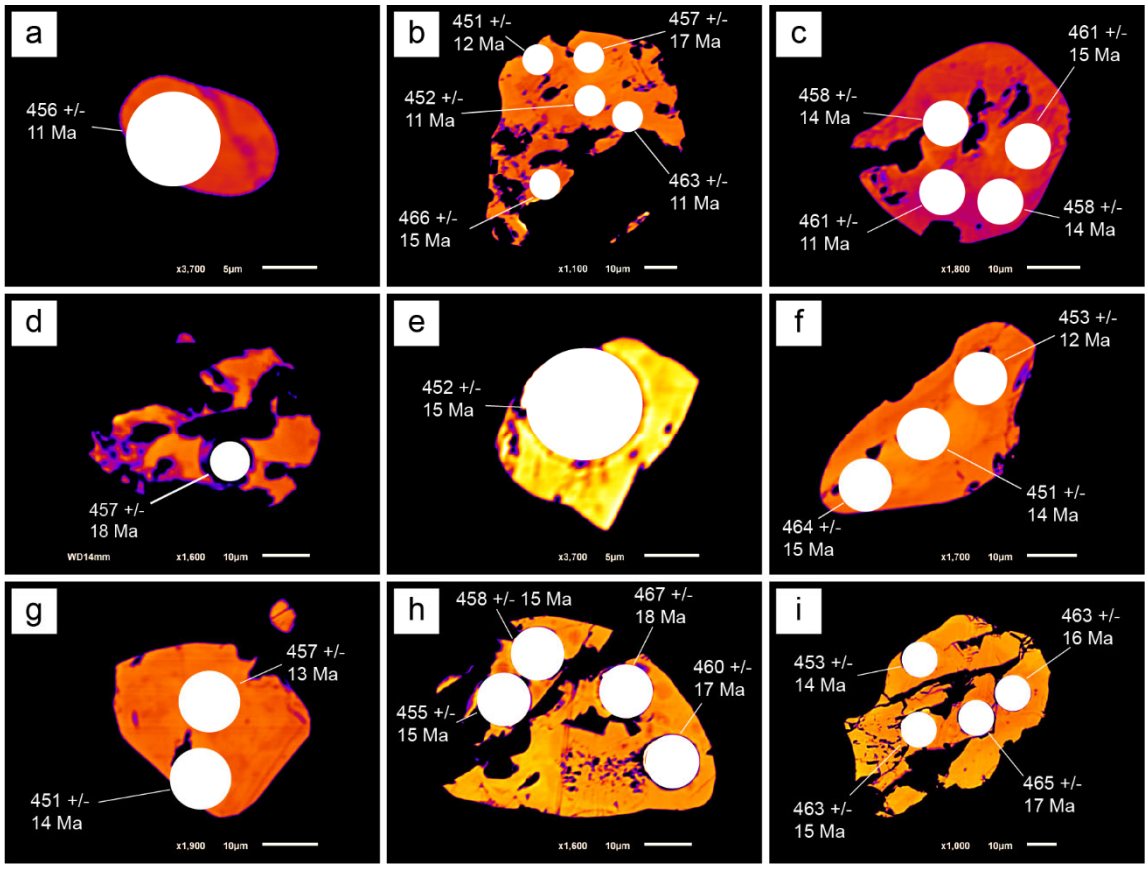

Figure 3.3 Colorized backscatter electron images taken at minimal brightness and high contrast settings of all monazite and xenotime grains analyzed from SK440, as well as LASS analysis spots and resulting ages. All analyses in this sample are concordant.

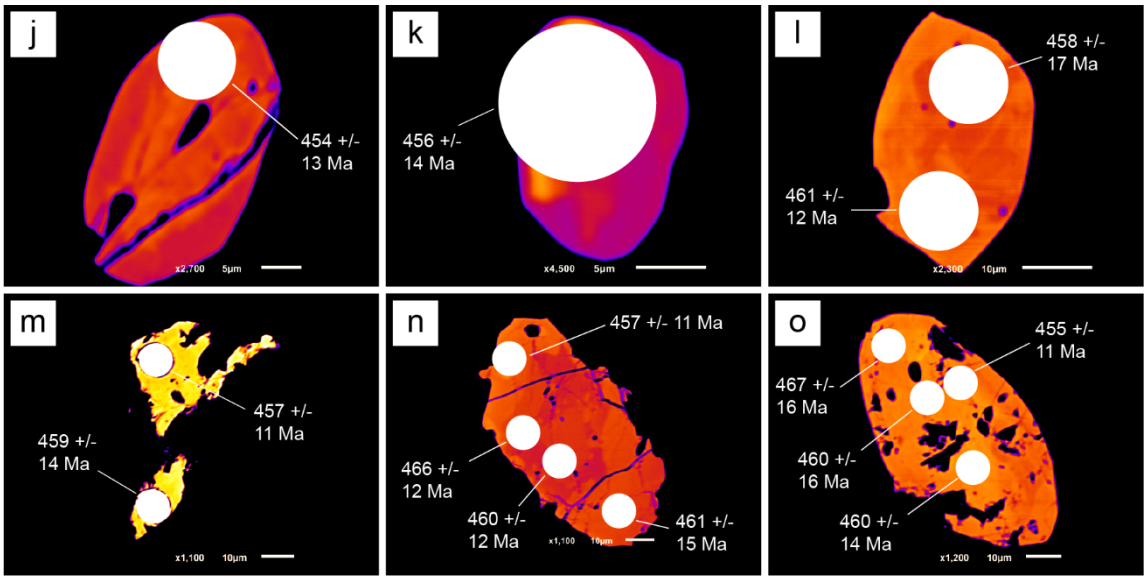

Figure 3.3 (cont.) Colorized backscatter electron images taken at minimal brightness and high contrast settings of all monazite grains analyzed from SK440, as well as LASS analysis spots and resulting ages. All analyses in this sample are concordant.

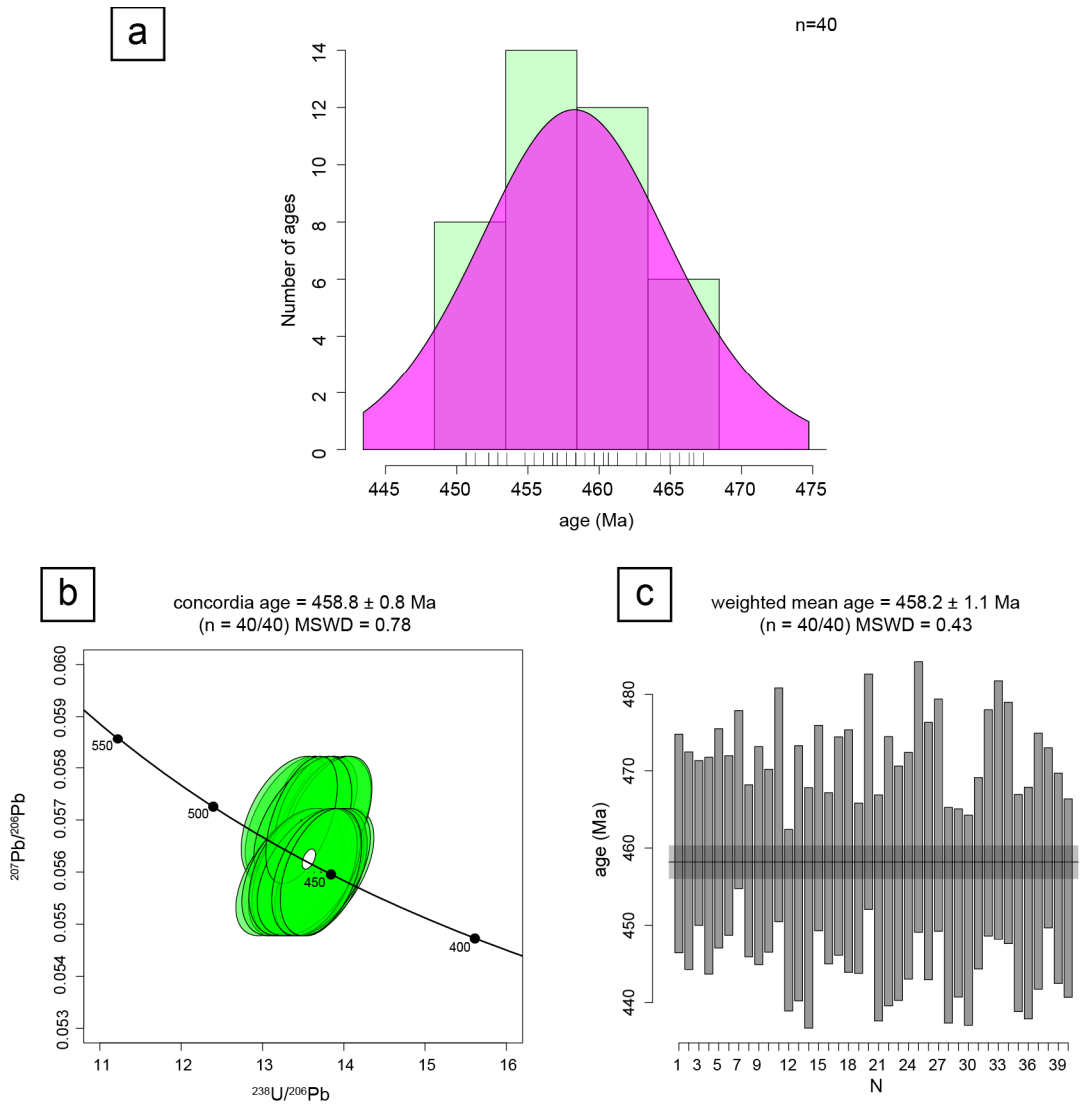

Figure 3.4 (a) KDE of all ages from SK440 showing a single age peak. (b) Concordia diagram of all ages from SK440, as well as concordia age calculations. White circle shows the concordia age ellipse with error, and points along the central line are age in Ma. (c) Weighted mean age plot and calculation of the same age peak shown in (a-b). Concordia age and weighted mean age vary by less than 0.5 Ma.

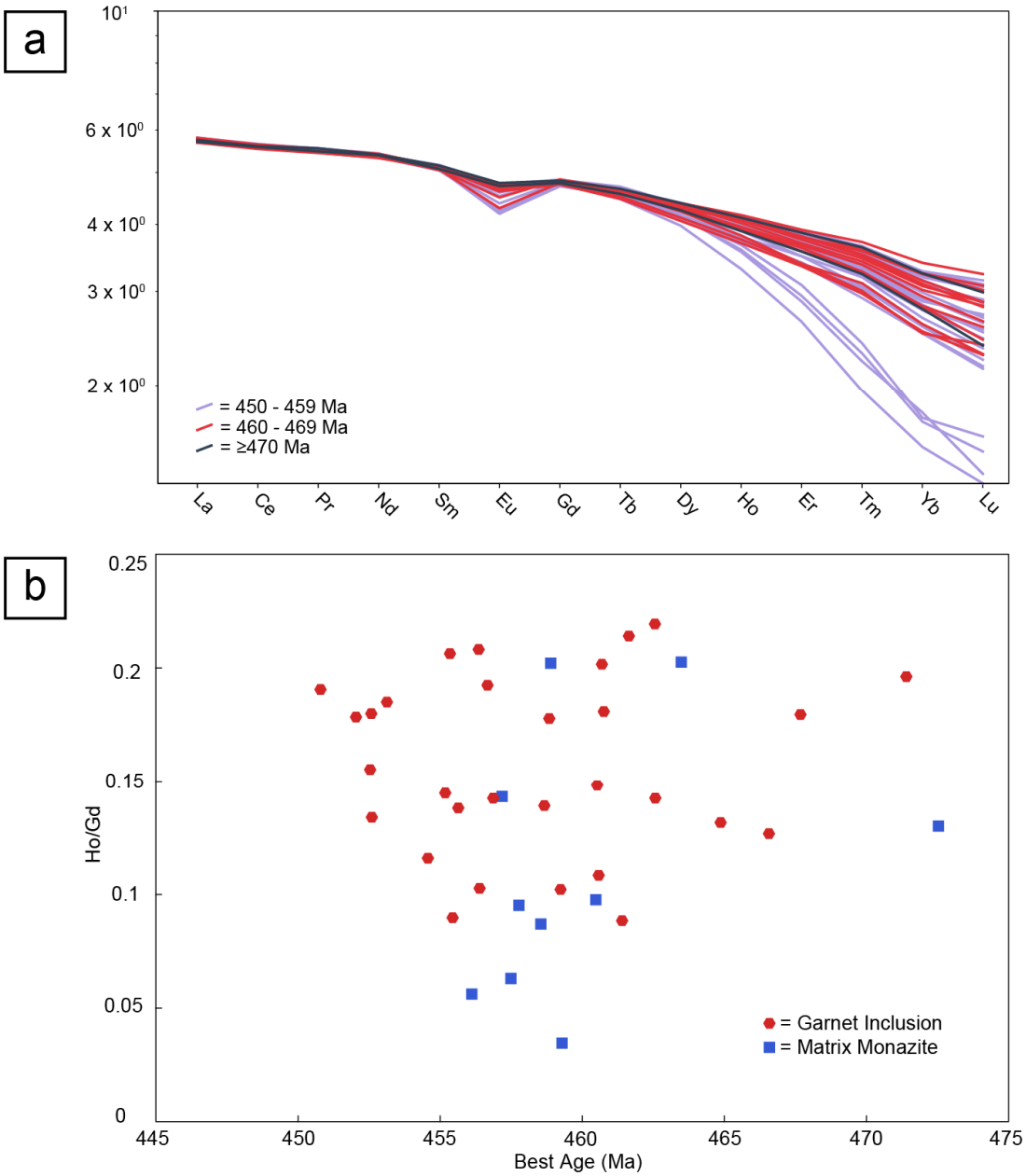

Figure 3.5 Rare earth element plots of monazite from SK440. (a) Spider diagram of monazite showing a clear negative Eu anomaly as well as a slight spread of HREE enrichment, particularly in the younger ages. (b) The ratio of chondrite-normalized Ho to Gd plotted against concordia age.

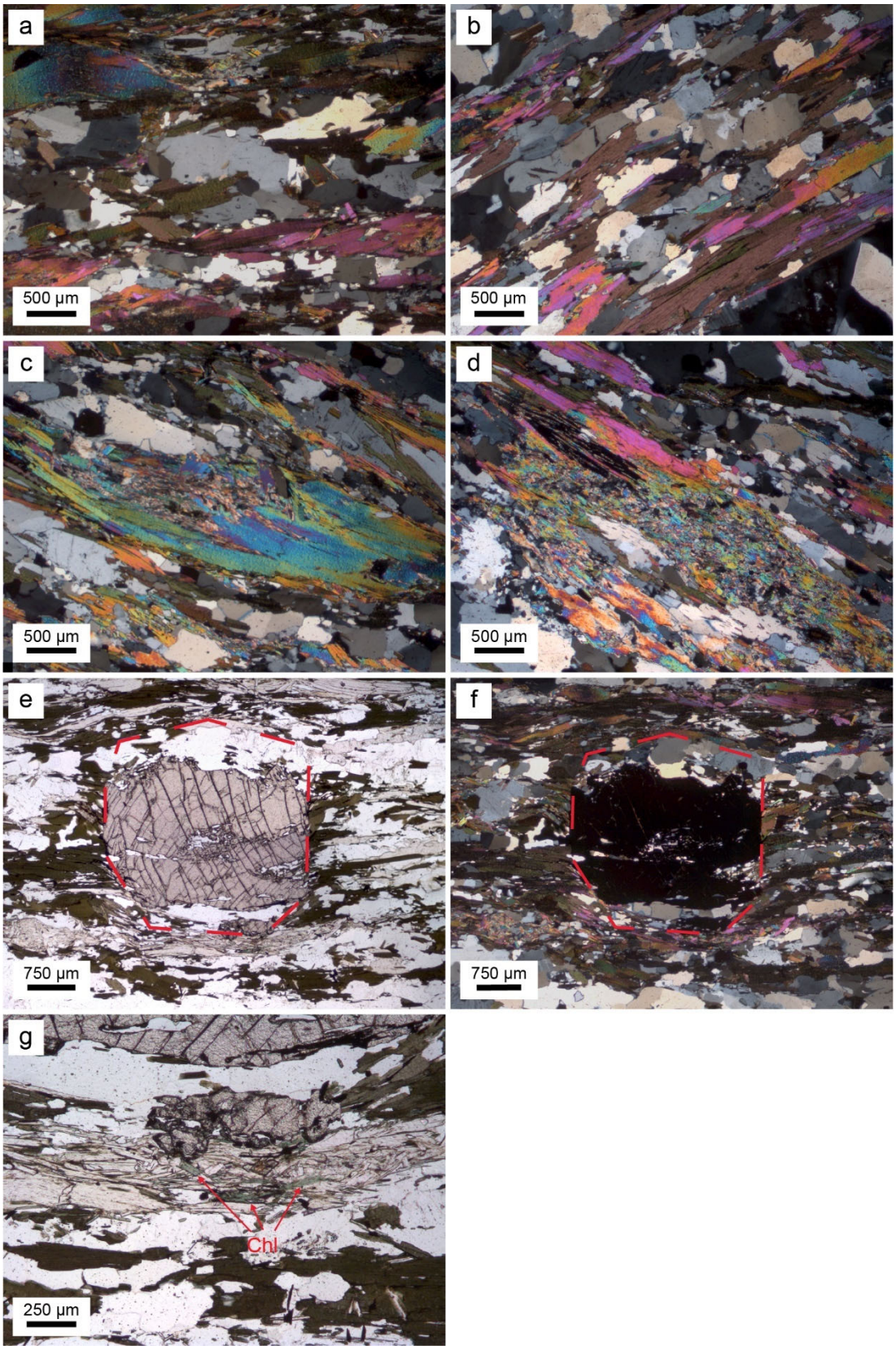
a
500 µm
b
500 µm
c
500 µm
d
500 µm
e
750 µm
f
750 µm
g
Chl
250 µm

Figure 3.6 Photomicrographs from sample BR-20-10. (a-b) Representative mineralogy and foliation captured in both micas and elongated quartz ribbons. (c-d) Examples of muscovite textures in this sample, showing both larger muscovite laths and more fine fibers. (e-f) Plane-polarized light and cross-polarized light images, respectively, of garnet from this sample. Red outline shows interpreted original grain size before alteration to quartz, plagioclase, and biotite. (g) Plane-polarized light image taken from the bottom center of (e) at higher magnification, showing very small chlorite grains around the exterior of the garnet.

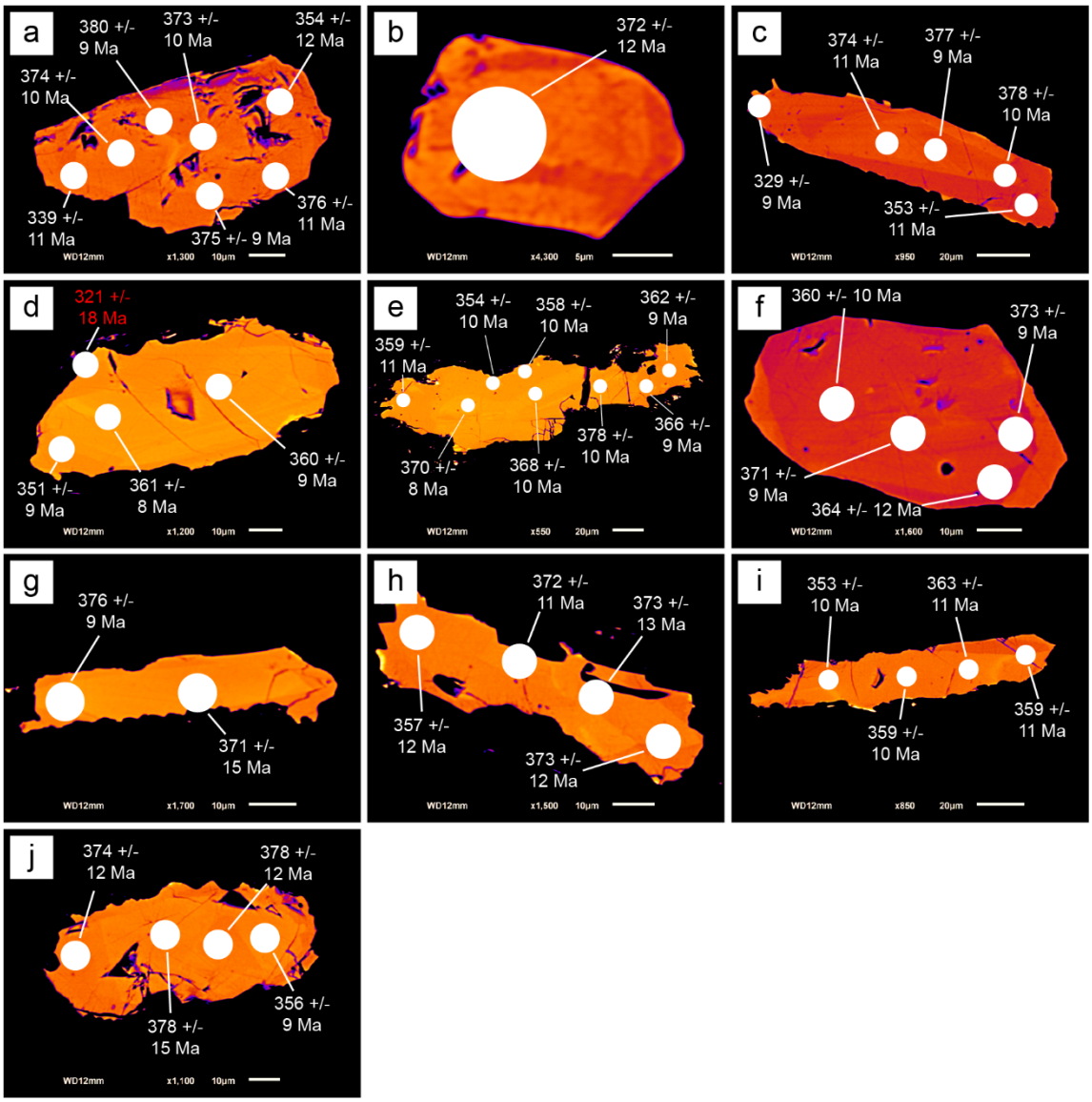

Figure 3.7 Colorized backscatter electron images taken at minimal brightness and high contrast settings of all monazite and xenotime grains analyzed from BR-20-10, as well as LASS analysis spots and resulting ages. All grains shown are monazite aside from (s) which is xenotime. White ages are concordant, whereas red ages are discordant and excluded from all plots (e.g. KDE, weighted means, concordia diagrams, REE plots).

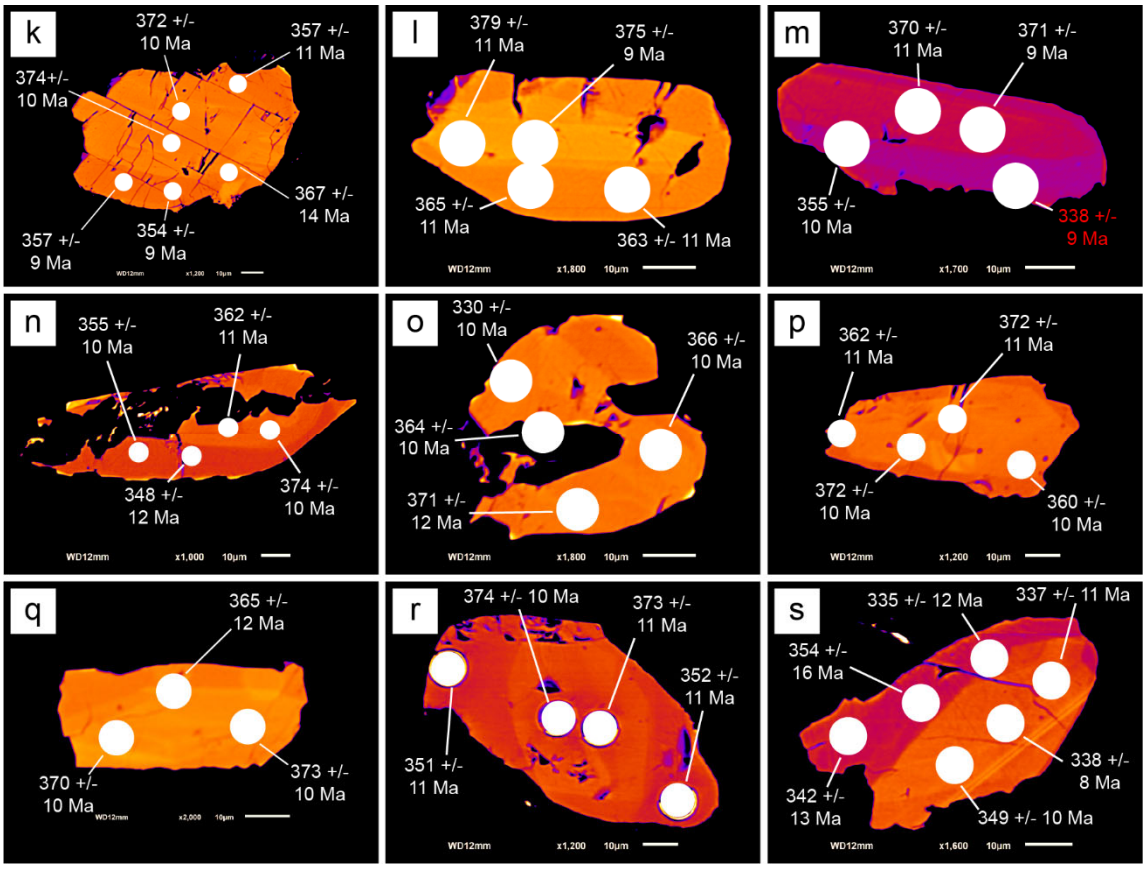

Figure 3.7 (cont.) Colorized backscatter electron images taken at minimal brightness and high contrast settings of all monazite and xenotime grains analyzed from BR-20-10, as well as LASS analysis spots and resulting ages. All grains shown are monazite aside from (s) which is xenotime. White ages are concordant, whereas red ages are discordant and excluded from all plots (e.g. KDE, weighted means, concordia diagrams, REE plots).

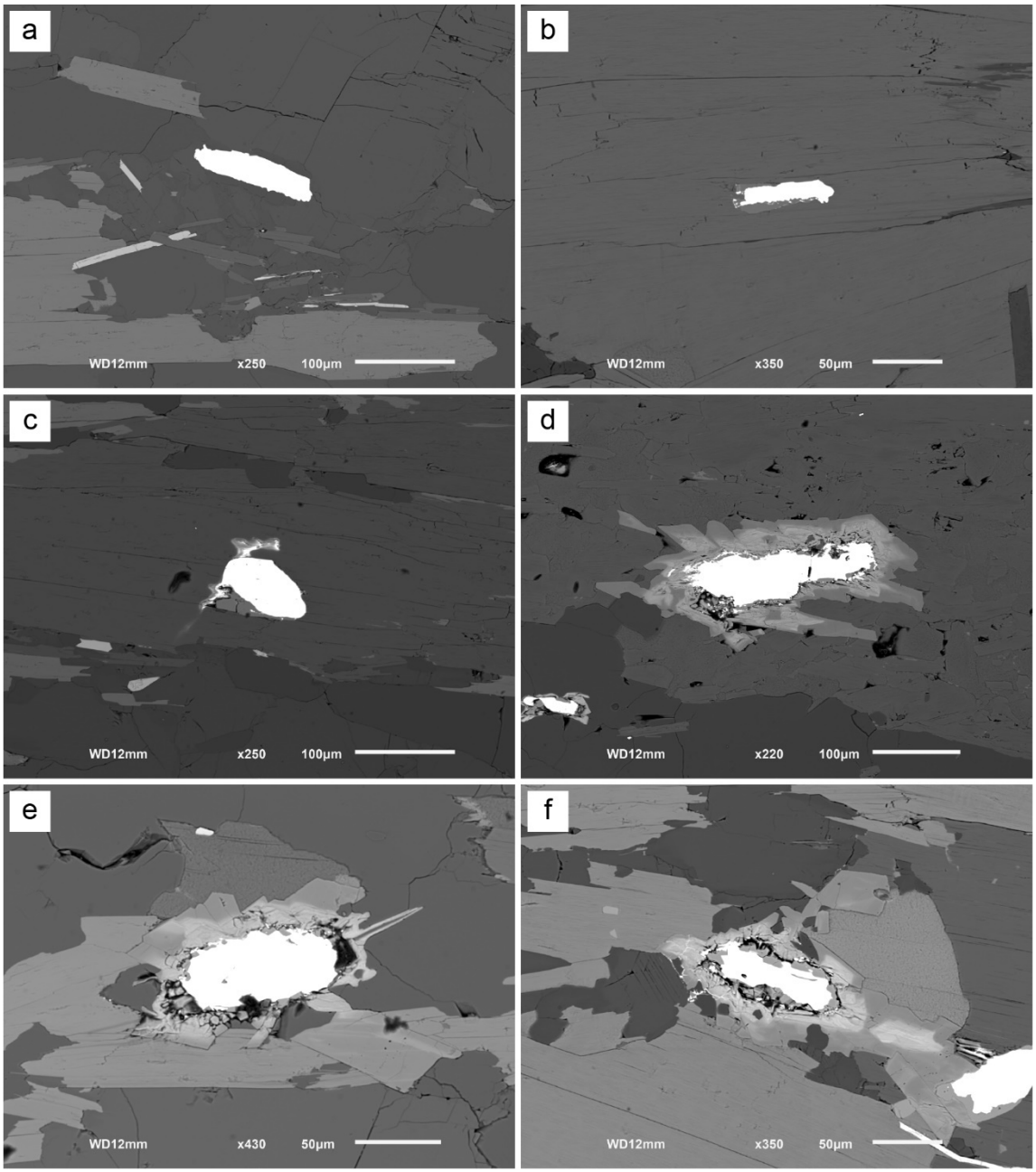

Figure 3.8 Lower magnification backscatter electron images from BR-20-10, taken at brightness and contrast settings optimal for visibility of all minerals in the sample. All grains in this figure show orientation with the long axis of the monazite grain roughly parallel to foliation. Additionally, (b-f) show alteration to apatite.

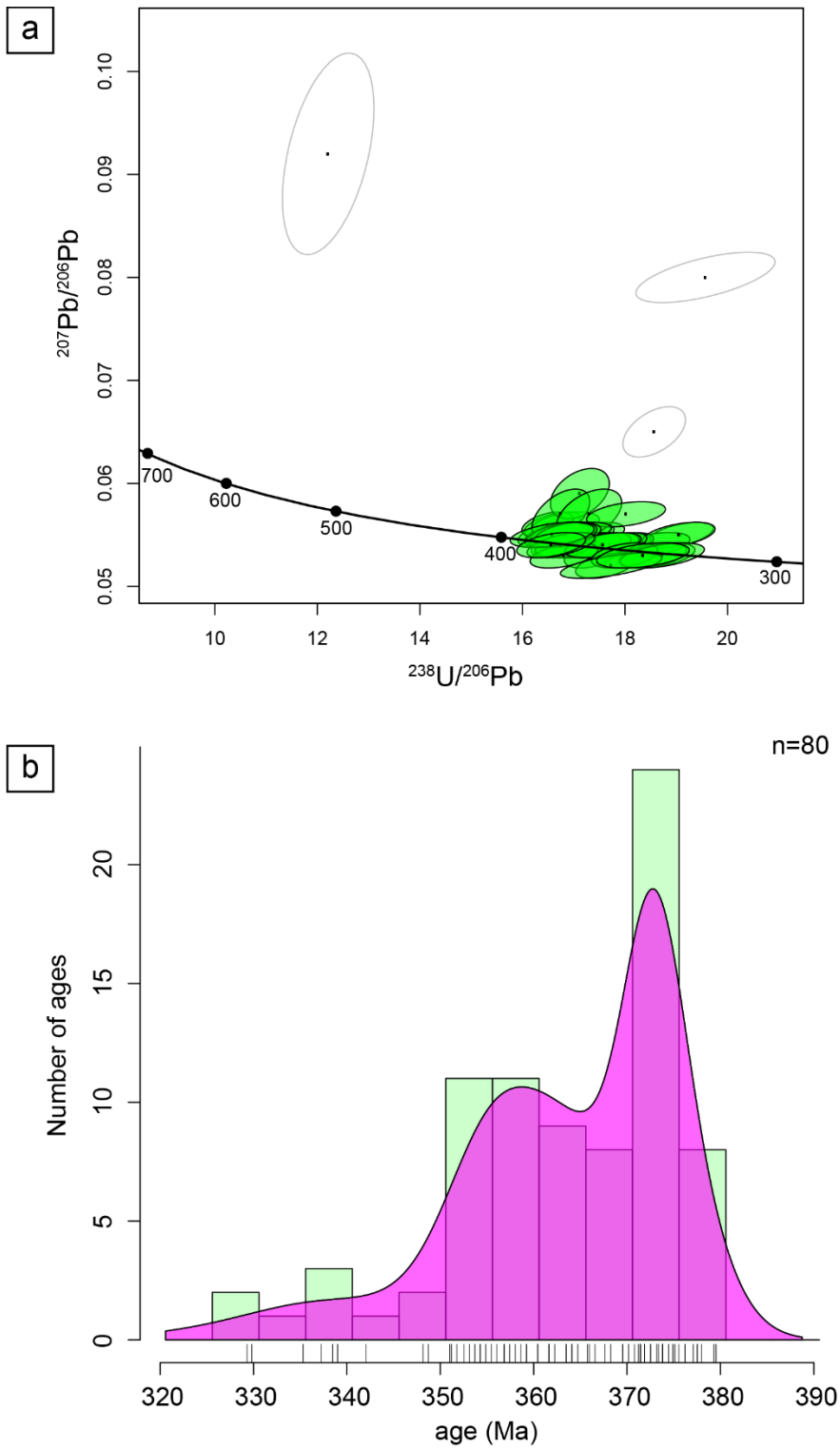

Figure 3.9 (a) Concordia diagram of all ages from BR-20-10. Points along the central line are age in Ma. (b) KDE of all ages from BR-20-10 showing two major age modes as well as a few younger ages. Xenotime ages are included in the youngest age cluster, whereas only monazite ages are present in the older two age peaks.

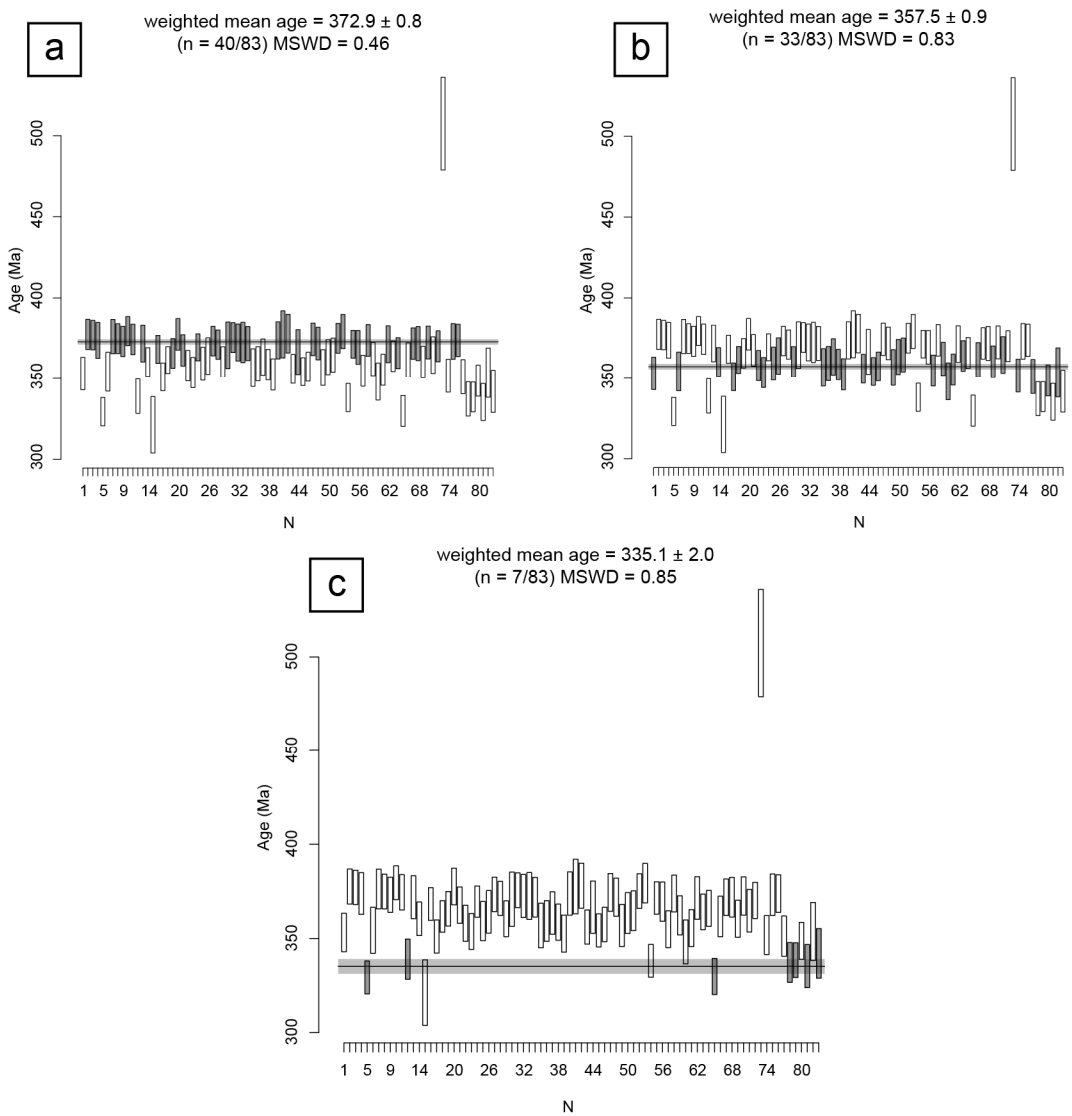

Figure 3.10 Weighted mean age plots and calculations from the three age peaks in BR-20-10 (Fig. 3.9b), separated into groups (divided at 343 Ma and 365 Ma) by visually identifying the troughs between each peak. Horizontal gray bars indicate the confidence interval for the weighted mean. (a) Oldest age mode excluding discordant ages which shows a Neoacadian age. (b) Age peak falling between (a) and (c), showing a slightly younger Neoacadian age. Together, (a) and (b) make up the majority of the sample. (c) Youngest age cluster, consisting of both monazite and xenotime ages.

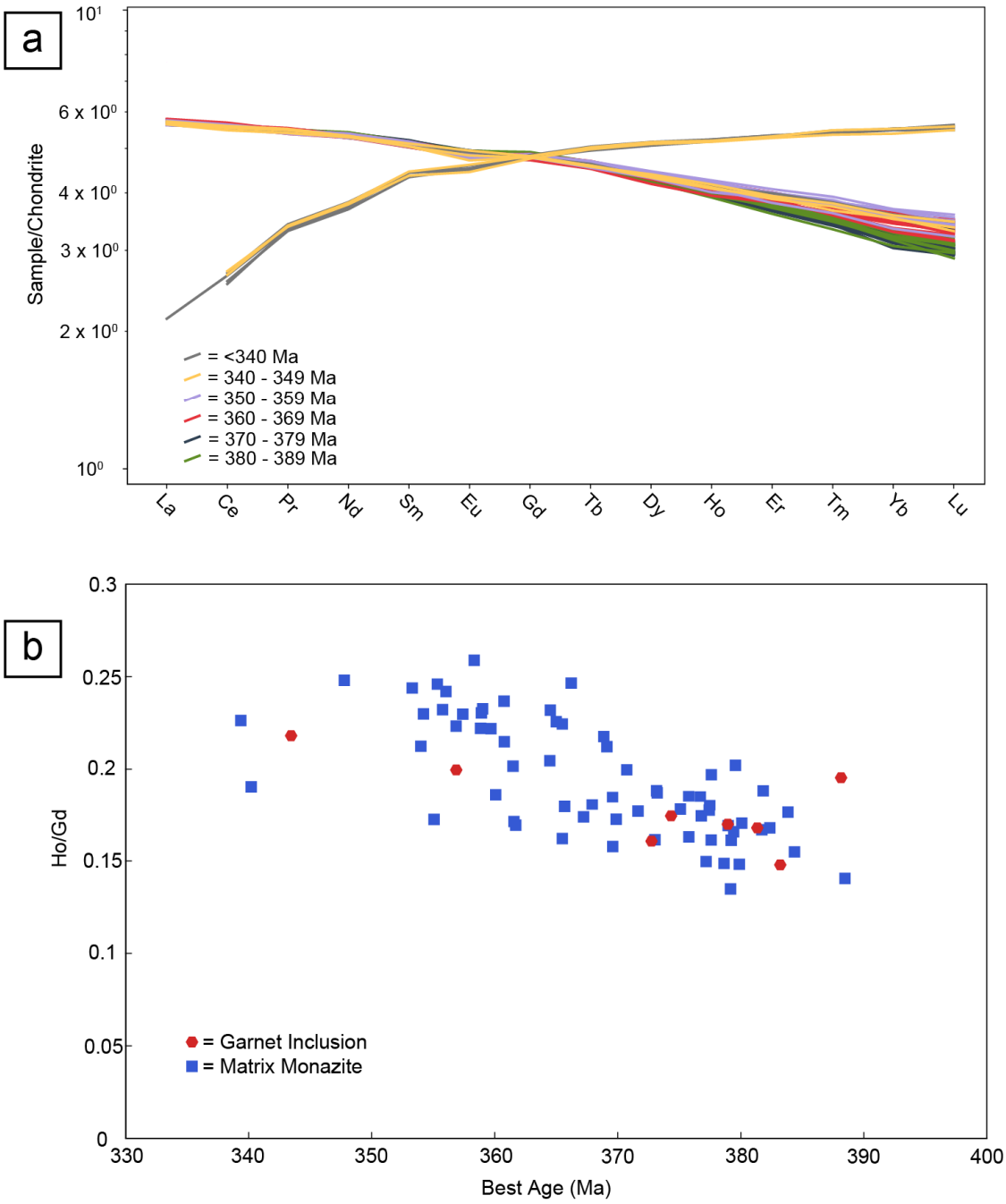

Figure 3.11 Rare earth element plots of monazite and xenotime from BR-20-10. (a) Spider diagram of monazite (higher LREE, lower HREE) and xenotime (lower LREE, higher HREE) showing almost no discernable Eu anomaly and a slight spread in HREEs in monazite. Older monazite ages are slightly more depleted in HREE than younger ages. (b) The ratio of chondrite-normalized Ho to Gd plotted against monazite age. All analyses are slightly enriched in HREEs, and show a very slight trend towards further enrichment as ages get younger.

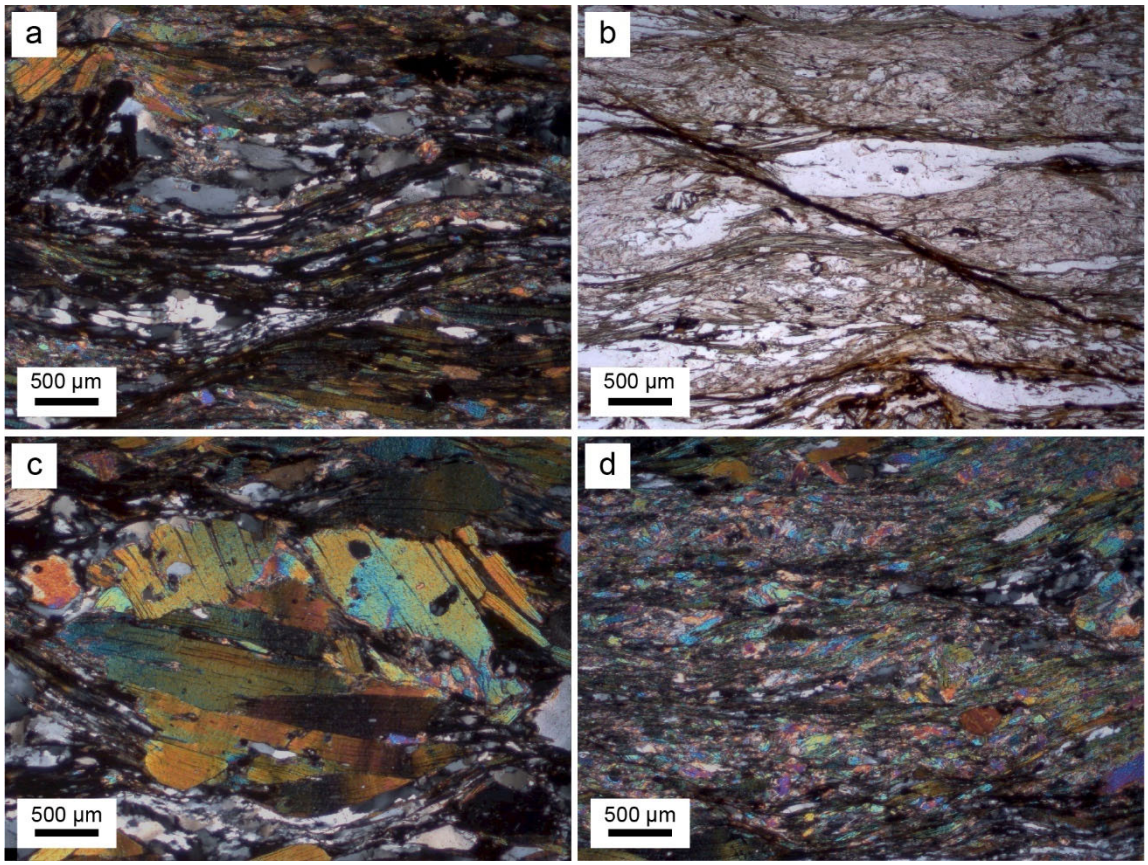

Figure 3.12 Photomicrographs of BR-20-14. (a) Representative mineralogy and foliation. (b) Plane-polarized light image showing shearing and fabrics captured by chlorite and muscovite in BR-20-14. (c-d) Cross-polarized light images of muscovite textures in this sample, showing both larger muscovite laths and finer-grained fibers.

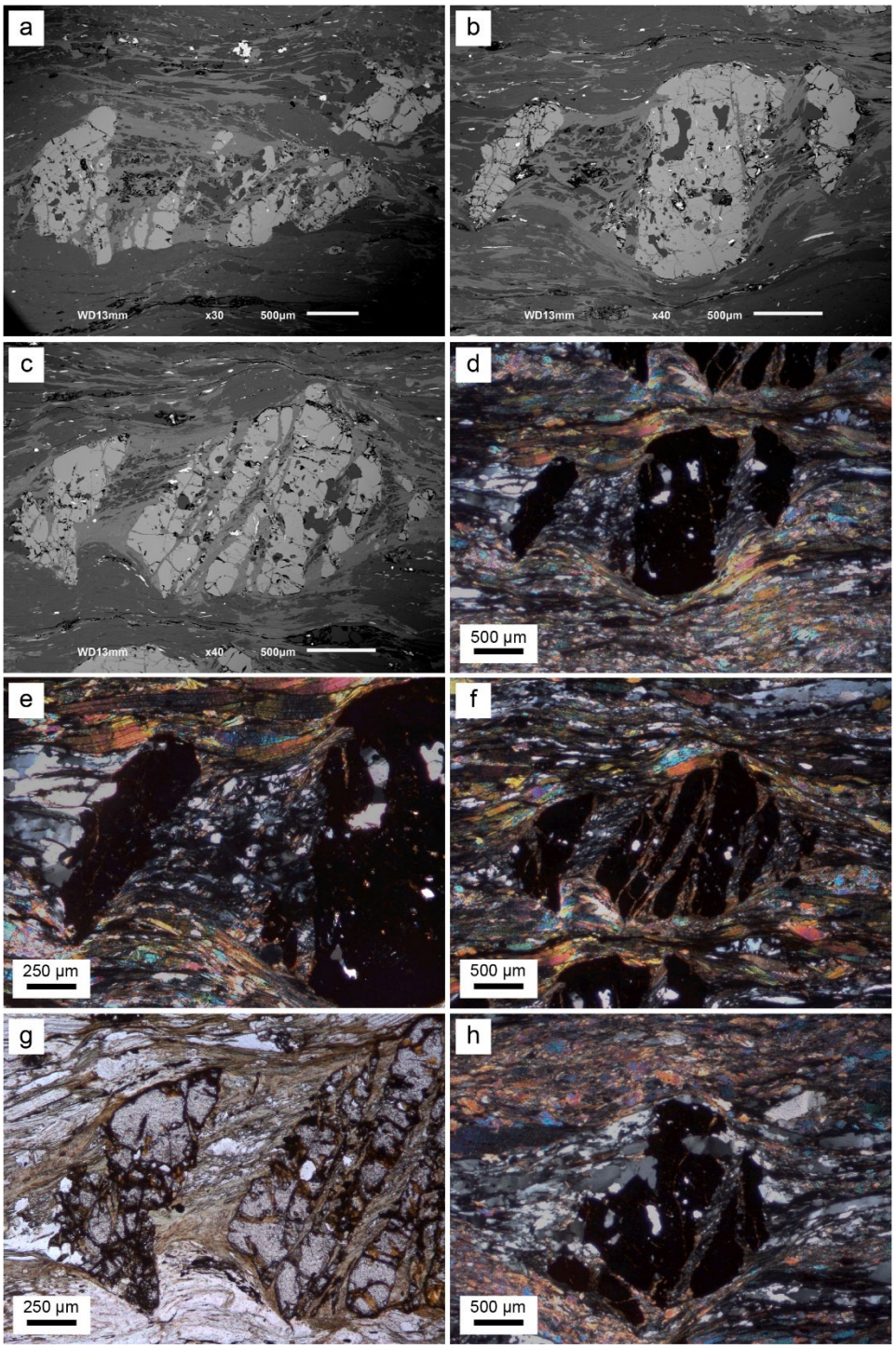

Figure 3.13 SEM backscatter electron images and photomicrographs of garnet in BR-20-14. (a-c) SEM backscatter electron images of garnet that shows extensive shearing and alteration to chlorite and quartz between originally intact fragments of garnet. (d-g) Sheared garnet grains in both cross-polarized and plane-polarized light, showing quartz and chlorite alteration byproducts in higher magnification. (h) Garnet that shows alteration to quartz, feldspar, and mica without the same shearing and alteration to chlorite as is present in other garnet grains.

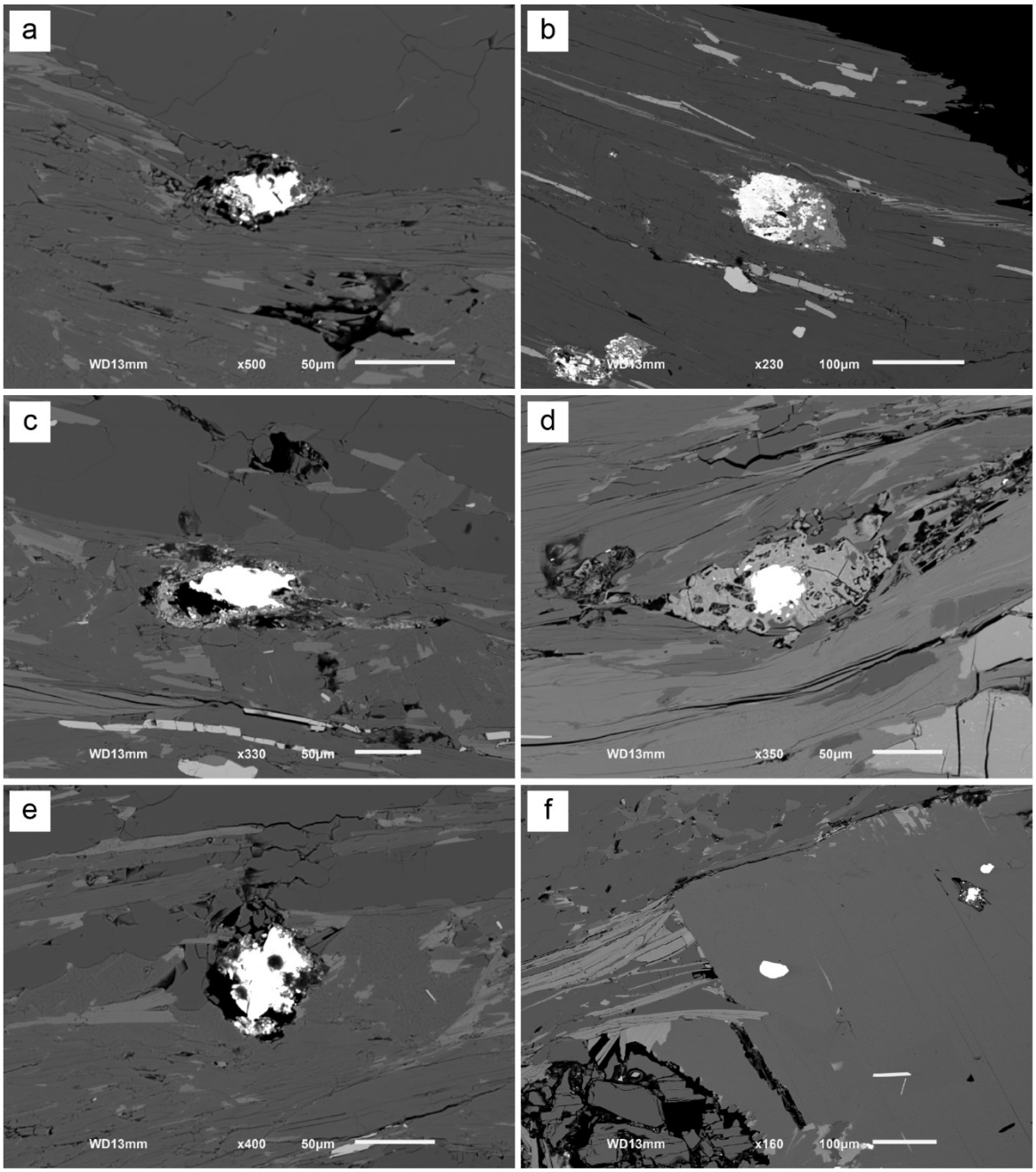

Figure 3.14 SEM backscatter electron images of monazite from BR-20-14 showing alteration of most grains to a combination of Al-rich phosphate minerals (a-e) as well as one monazite inclusion in feldspar that appears to have been shielded from alteration (f).

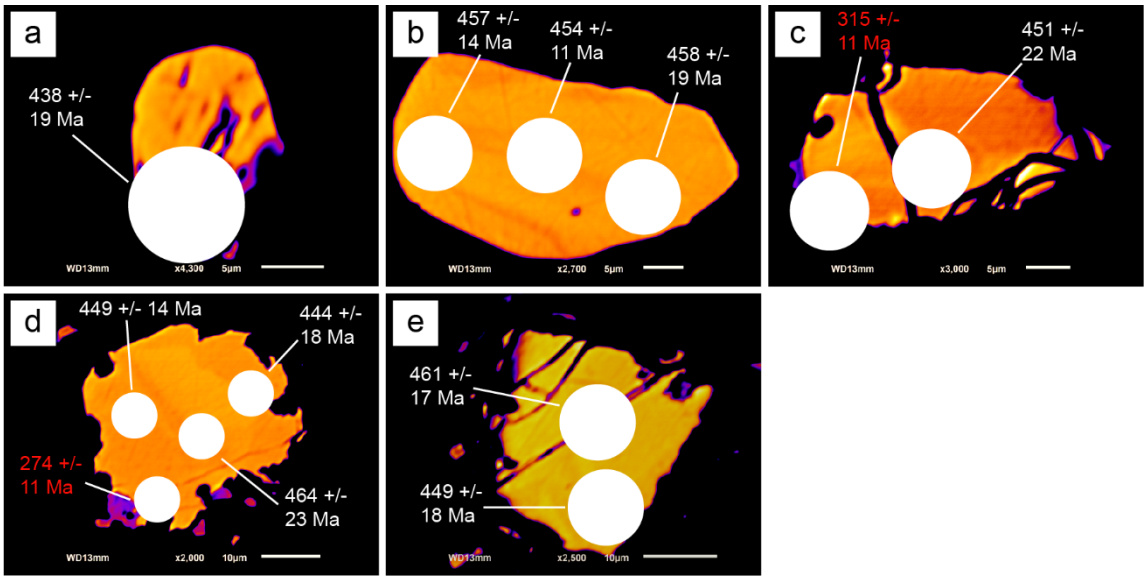

Figure 3.15 Colorized backscatter electron images of monazite in BR-20-14 taken at minimal brightness and high contrast settings of all monazite grains analyzed from this sample, as well as LASS analysis spots and resulting ages. White ages are concordant, whereas red ages are discordant and excluded from all plots (e.g. KDE, weighted means, concordia diagrams, REE plots).

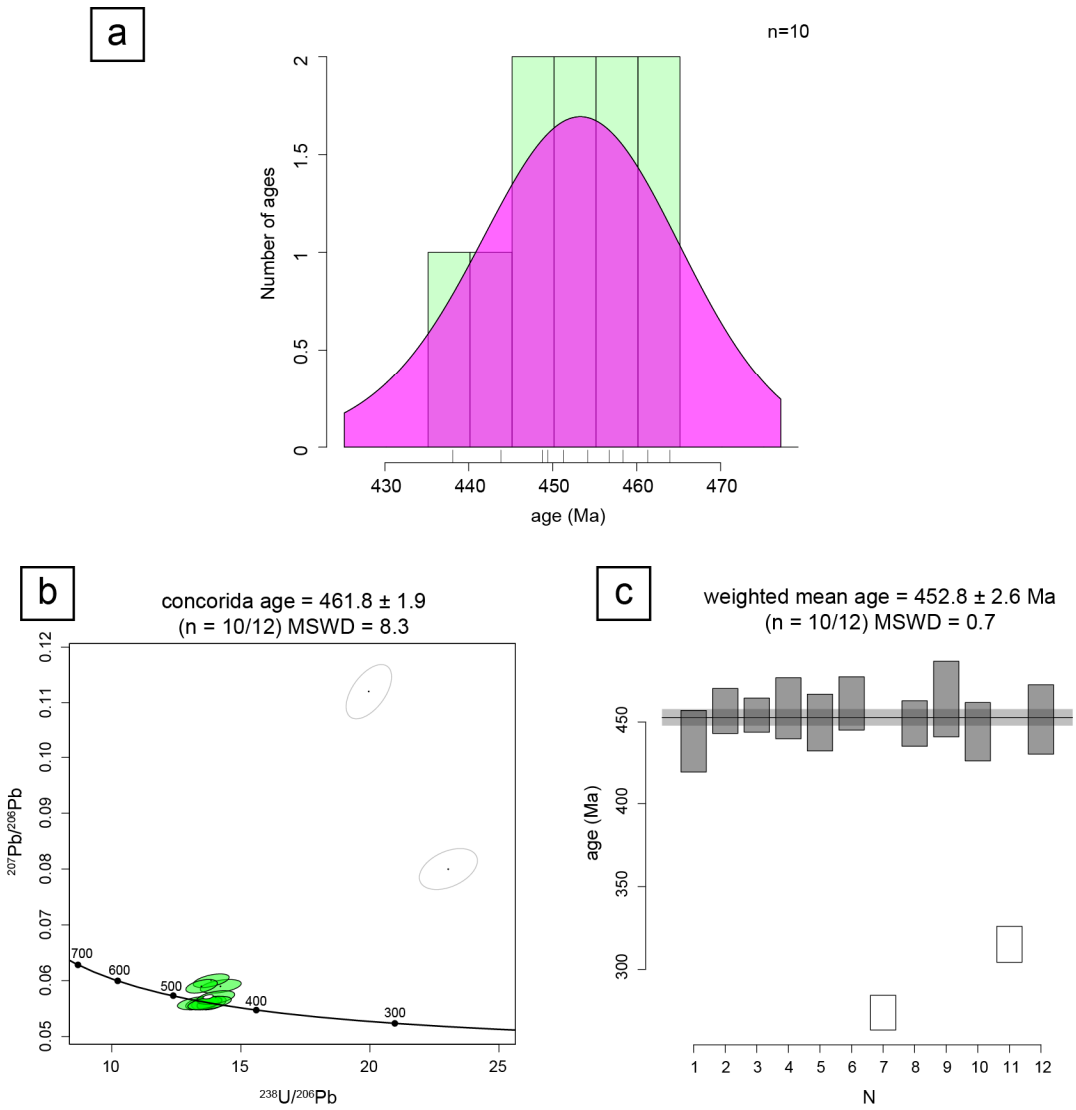

Figure 3.16 (a) KDE of all ages from BR-20-14 showing a single age peak. (b) Concordia diagram of all ages from BR-20-10, as well as concordia age calculations. White circle shows the concordia age ellipse with error, and points along the central line are age in Ma. (c) Weighted mean age plot and calculation of the same age peak shown in (a-b). Concordia age and weighted mean age vary by less than 0.5 Ma and errors are within 0.01 Ma between the concordia age and the weighted mean age.

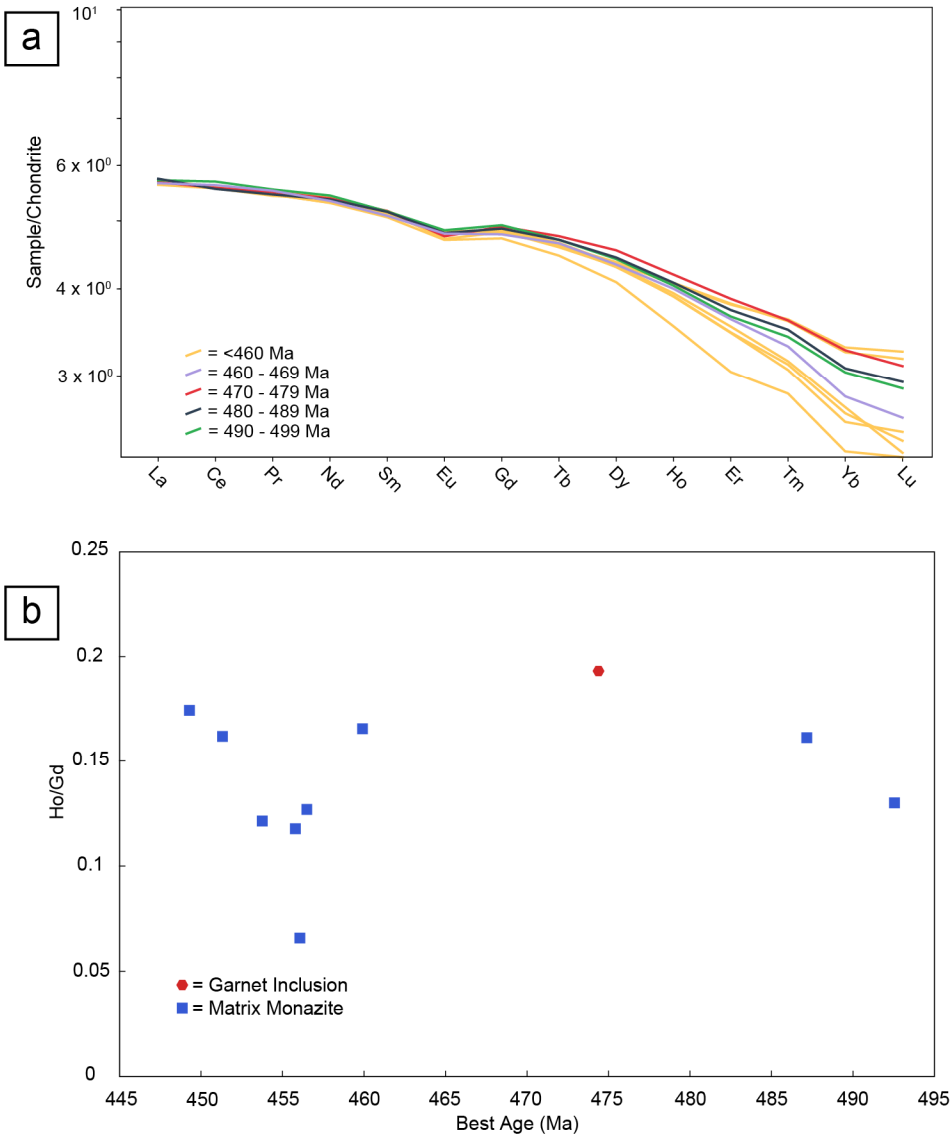

Figure 3.17 Rare earth element plots of monazite BR-20-14. (a) Spider diagram of monazite a slight spread in HREEs in monazite as well as a slight negative Eu anomaly. Older ages show a spread of HREE enrichment that is almost entirely within the spread of HREE enrichment in younger ages. Note the difference in range of the vertical axis compared to other samples. (b) The ratio of chondrite-normalized Ho to Gd plotted against monazite age. Most analyses show similar ranges of HREE depletion/enrichment, there is no change with age.

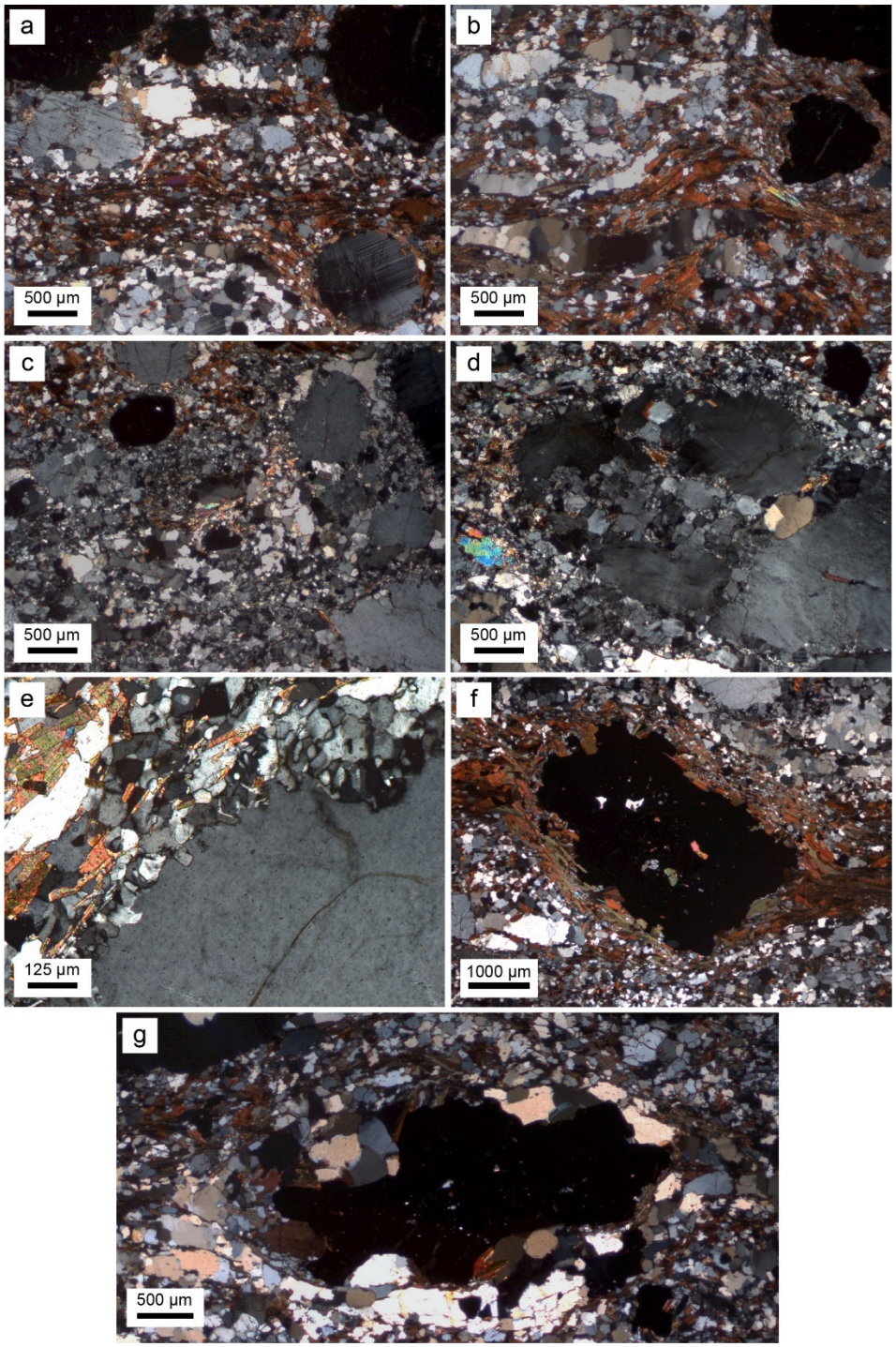

Figure 3.18 Photomicrographs of IP-18-05. (a-b) Representative mineralogy and foliation captured by biotite and elongated quartz ribbons. (c) Textures of highly recrystallized quartz and feldspar common throughout IP-18-05. (d-e) Large microcline porphyroclast showing subgrain rotation recrystallization as well as bulging recrystallization around grain borders. (f) Garnet grain showing shearing and localized biotite within pressure shadows. (g) Garnet grain showing elongation, potentially as a result of shearing, as well as alteration to quartz, plagioclase, and biotite.

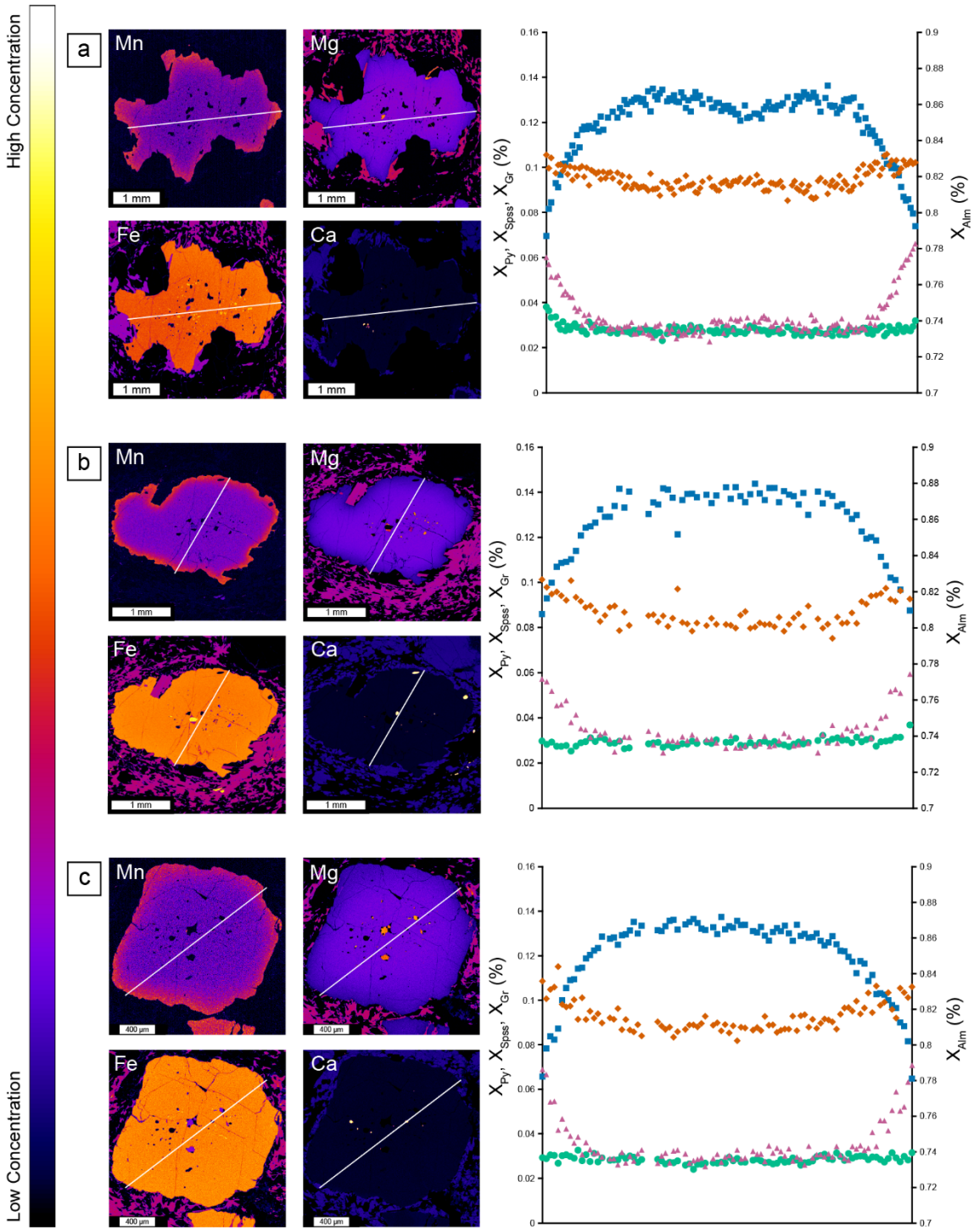

Figure 3.19 Colorized electron microprobe major element compositional maps of garnet as well as chemical traverse data. Orange diamonds are almandine compositions, blue squares are pyrope compositions, pink triangles are spessartine compositions, and teal circles are grossular compositions.

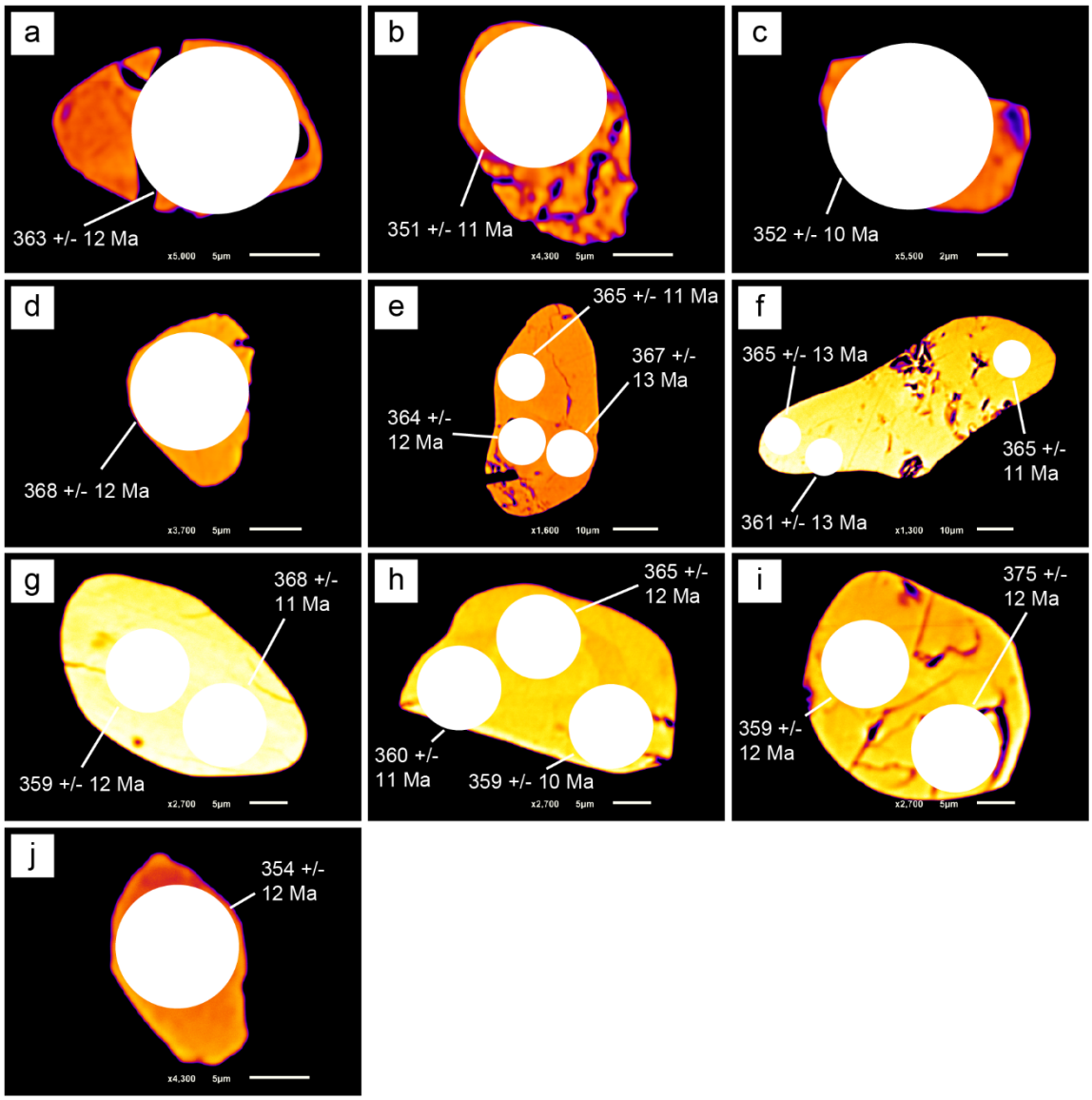

Figure 3.20 Colorized backscatter electron images taken at minimal brightness and high contrast settings of all monazite and xenotime grains analyzed from IP-18-05, as well as LASS analysis spots and resulting ages. All grains shown are monazite aside from (s) which is xenotime. White ages are concordant, whereas red ages are discordant and excluded from all plots (e.g. KDE, weighted means, concordia diagrams, REE plots).

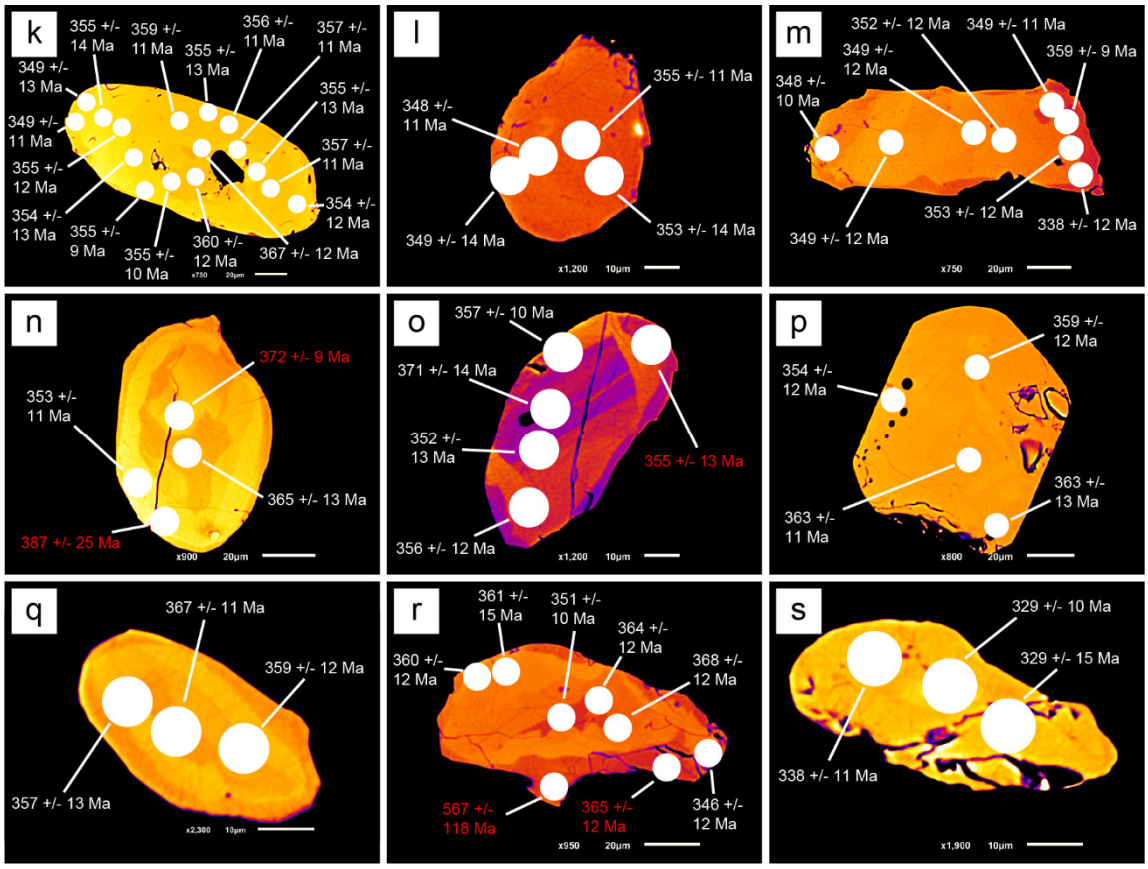

Figure 3.20 (cont.) Colorized backscatter electron images taken at minimal brightness and high contrast settings of all monazite and xenotime grains analyzed from IP-18-05, as well as LASS analysis spots and resulting ages. All grains shown are monazite aside from (s) which is xenotime. White ages are concordant, whereas red ages are discordant and excluded from all plots (e.g. KDE, weighted means, concordia diagrams, REE plots).

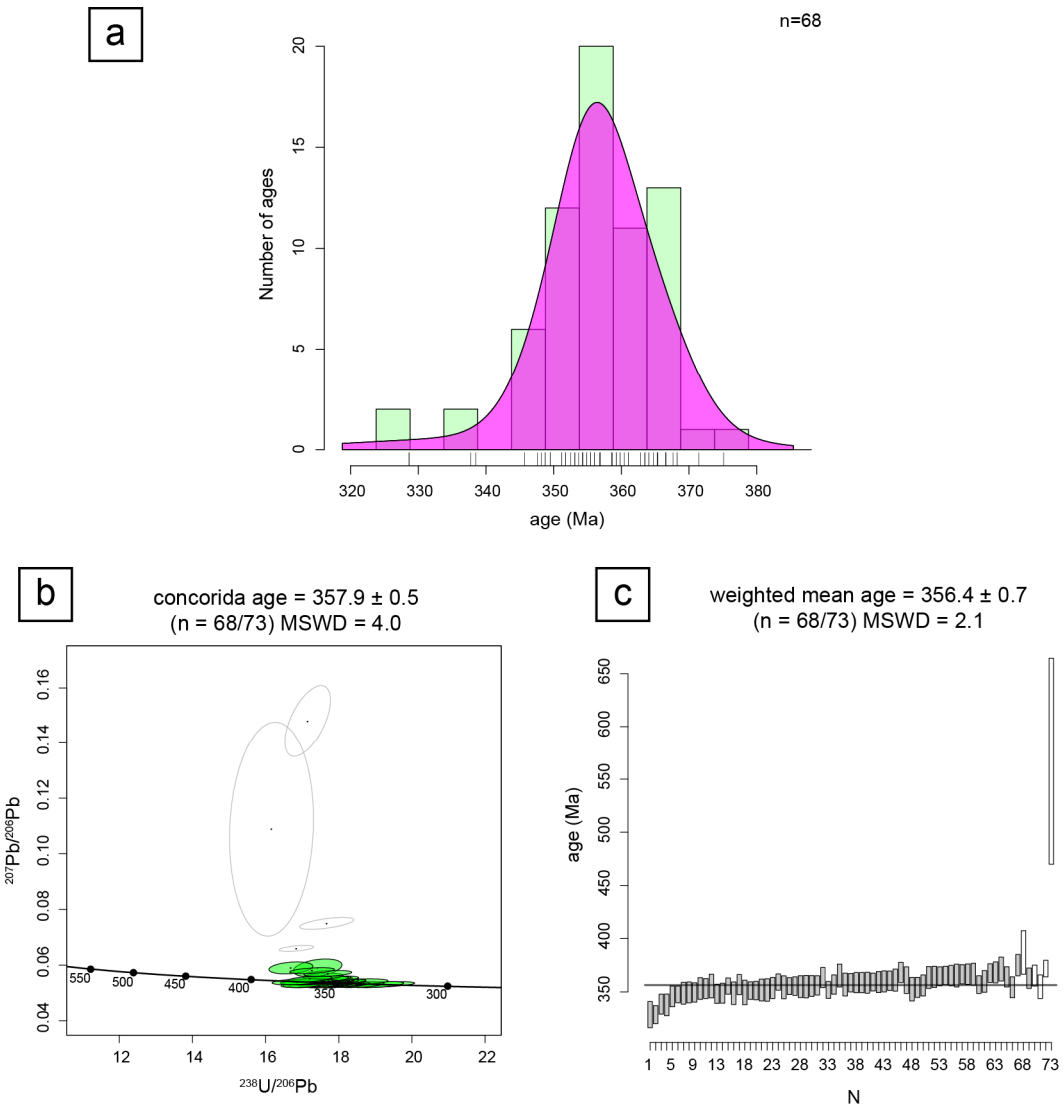

Figure 3.21 (a) KDE of all ages from IP-18-05 showing a single age peak. (b) Concordia diagram of all ages from IP-18-05 as well as concordia age calculations. White circle represents concordia age ellipse, and points along the central line are age in Ma. (c) Weighted mean age plot and calculation of the same age peak shown in (a-b). Concordia age and weighted mean age vary by only 0.1 Ma, and errors by 0.01 Ma.

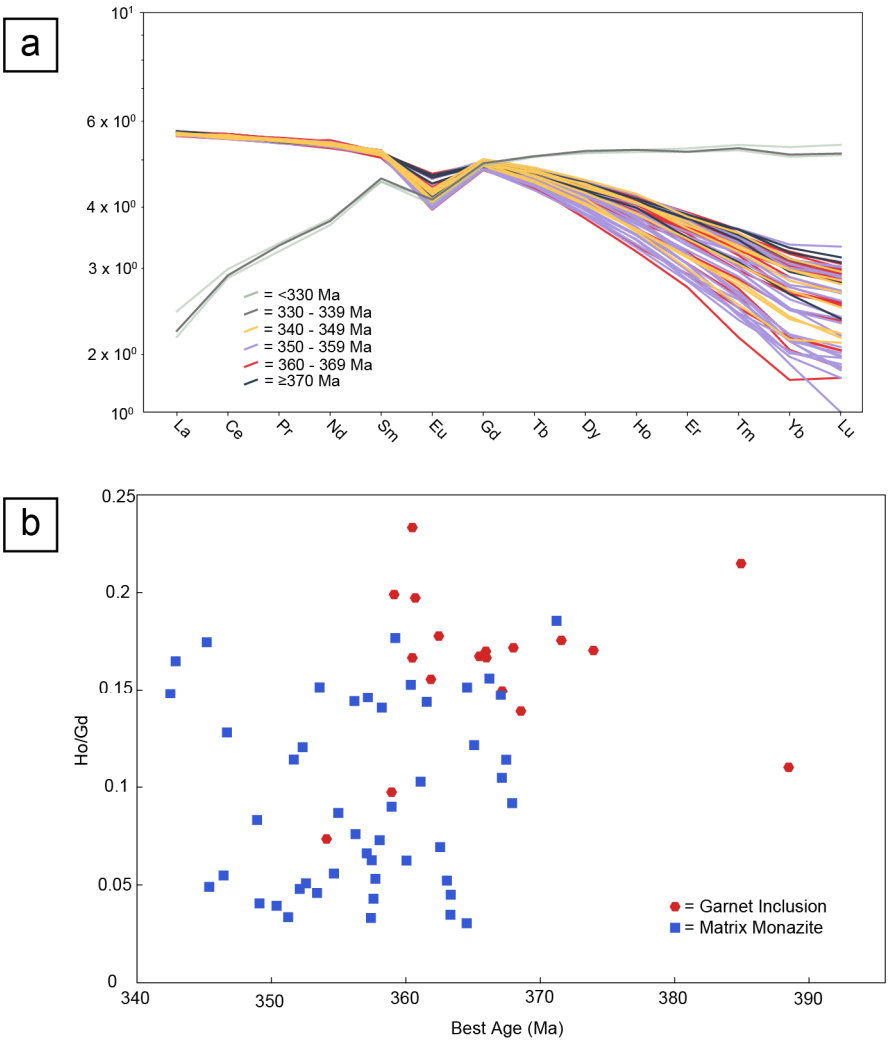

Figure 3.22. Rare earth element plots of monazite and xenotime from IP-18-05. (a) Spider diagram of monazite (higher LREE, lower HREE) and xenotime (lower LREE, higher HREE) showing a clear Eu anomaly that varies in magnitude by age and a spread in HREEs in monazite. Variations in HREE enrichment/depletion do not appear to have any relationship with age. (b) The ratio of chondrite-normalized Ho to Gd plotted against monazite age. Analyses vary in HREE enrichment and show no clear patterns with age, though garnet inclusion monazites have a slightly higher abundance of HREEs than matrix monazite.

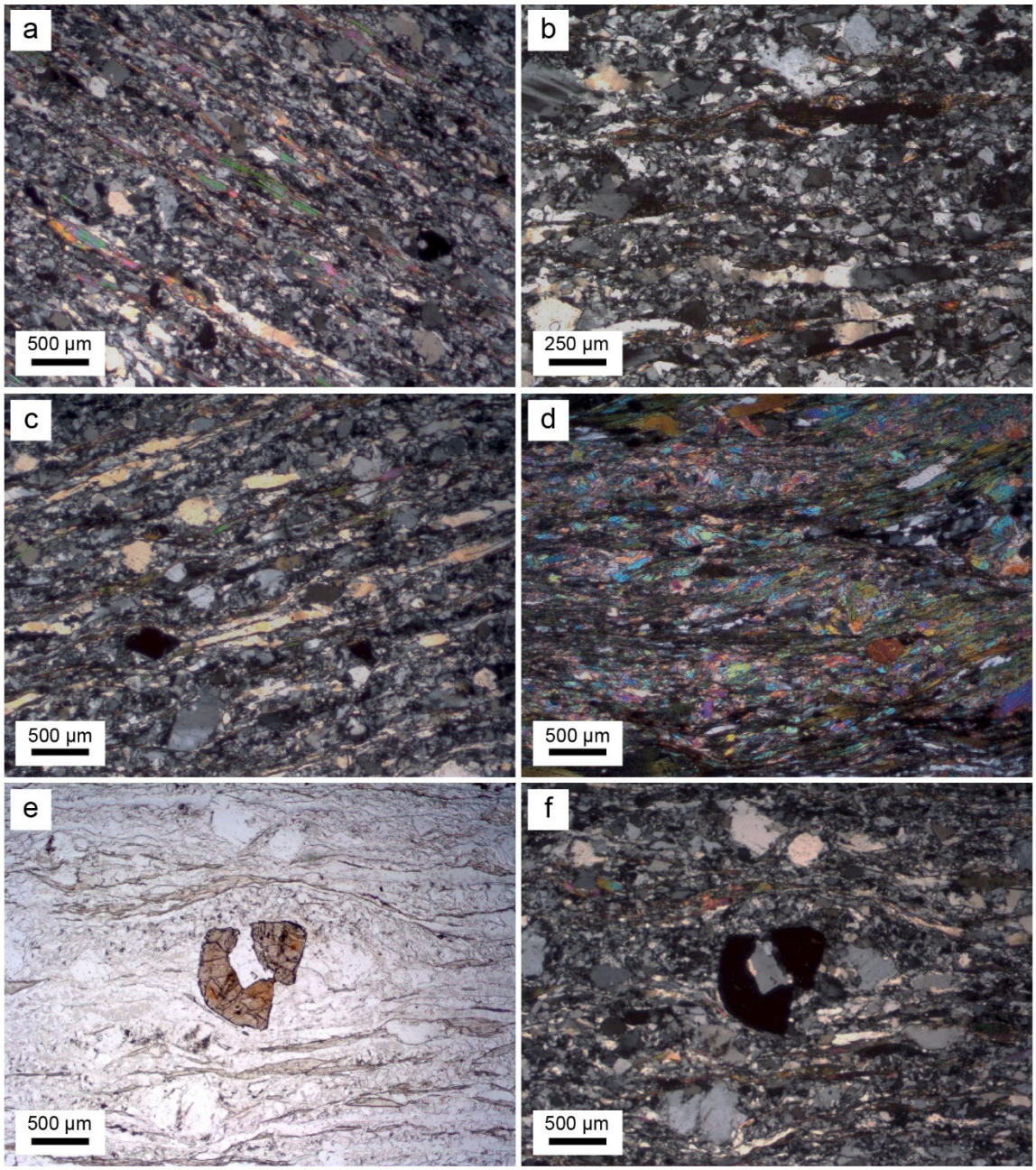

Figure 3.23 Photomicrographs of IP-20-19. (a-d) Representative mineralogy and foliation captured in elongated quartz grains and muscovite. (e-f) Plane-polarized light and cross-polarized light images of garnet in IP-20-19, showing highly anhedral shape.

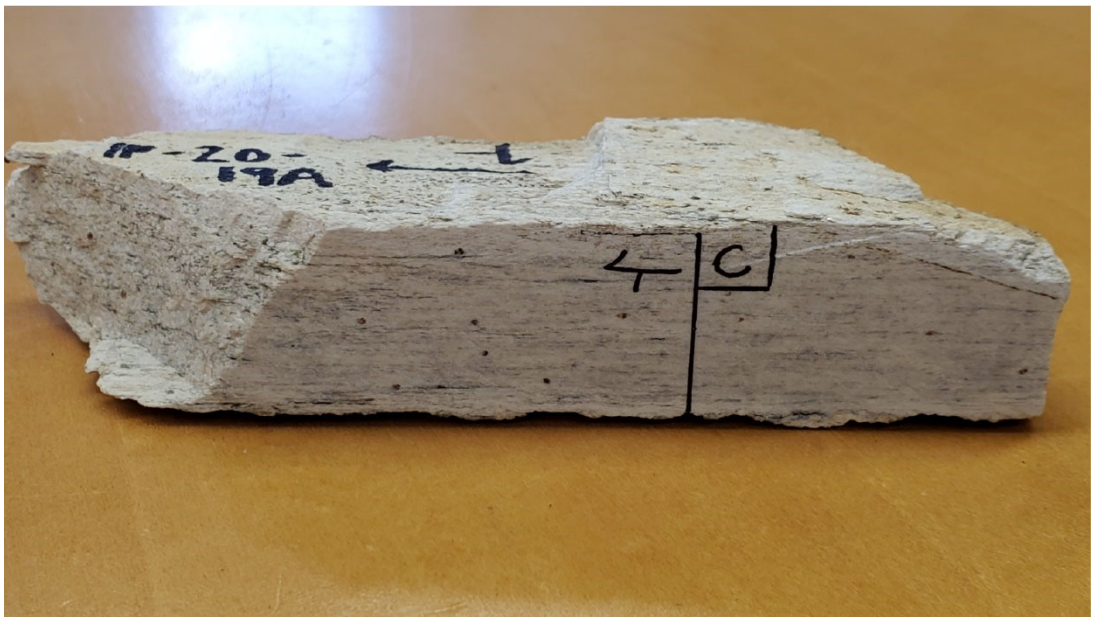

Figure 3.24 Hand sample photograph of IP-20-19. The thin section for this sample was cut along the flat face of this hand sample, on the right side within the area labeled "c". Height of sample, measured along the vertical black line is 2.6 cm.

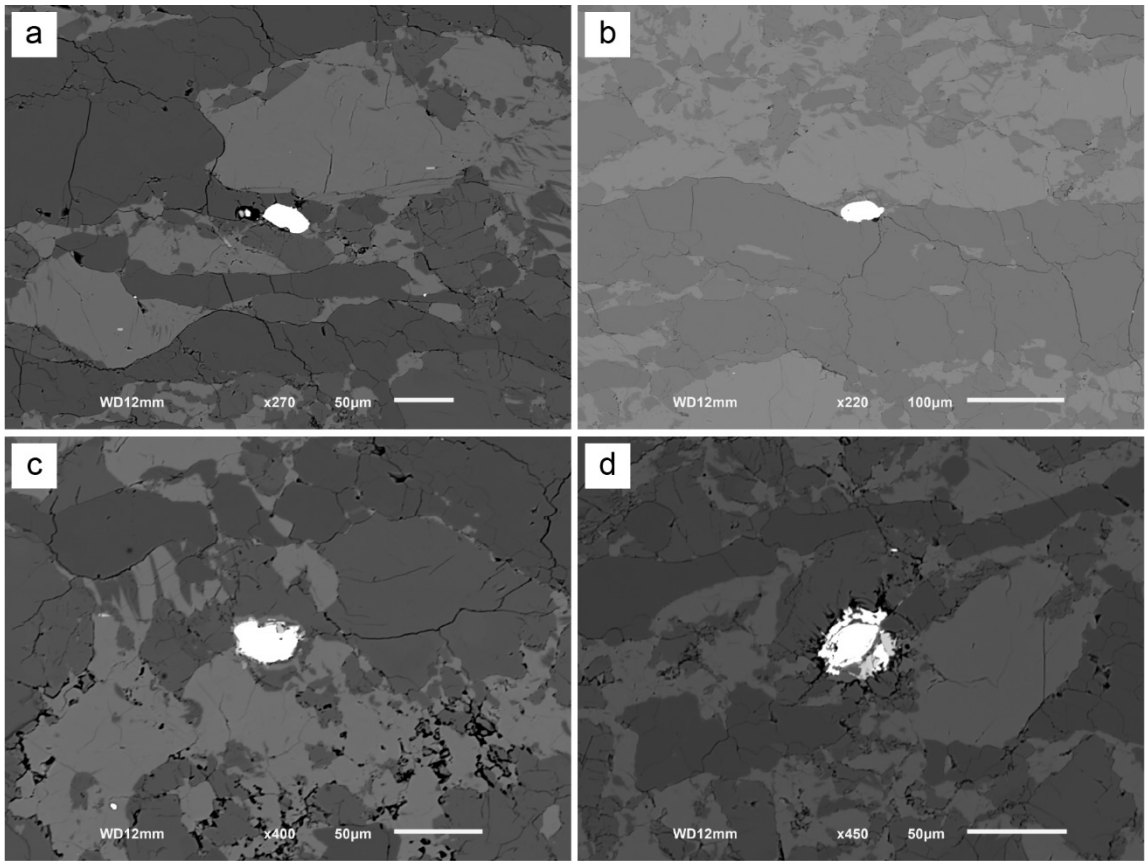

Figure 3.25 SEM backscatter electron images of monazite from IP-20-19 showing alignment of elongated axis of monazite grains roughly parallel or sub-parallel to foliation. Some grains, such as (c) and (d) show alteration to apatite.

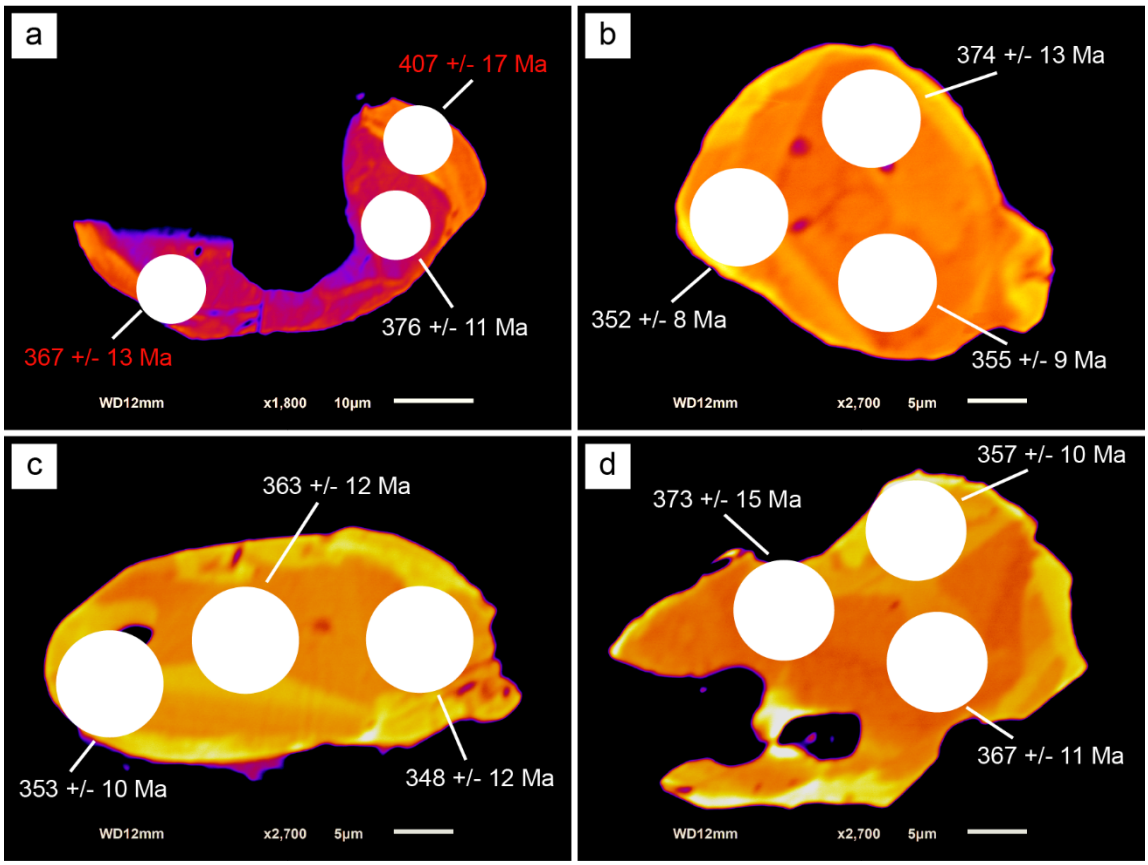

Figure 3.26 Colorized backscatter electron images taken at minimal brightness and high contrast settings of all monazite grains analyzed from IP-20-19, as well as LASS analysis spots and resulting ages. White ages are concordant, whereas red ages are discordant and excluded from all plots (e.g. KDE, weighted means, concordia diagrams, REE plots). All grains show clear zoning patterns, though in many instances the LASS spot size of 8 µm diameter is too large to analyze within a specific zoning domain.

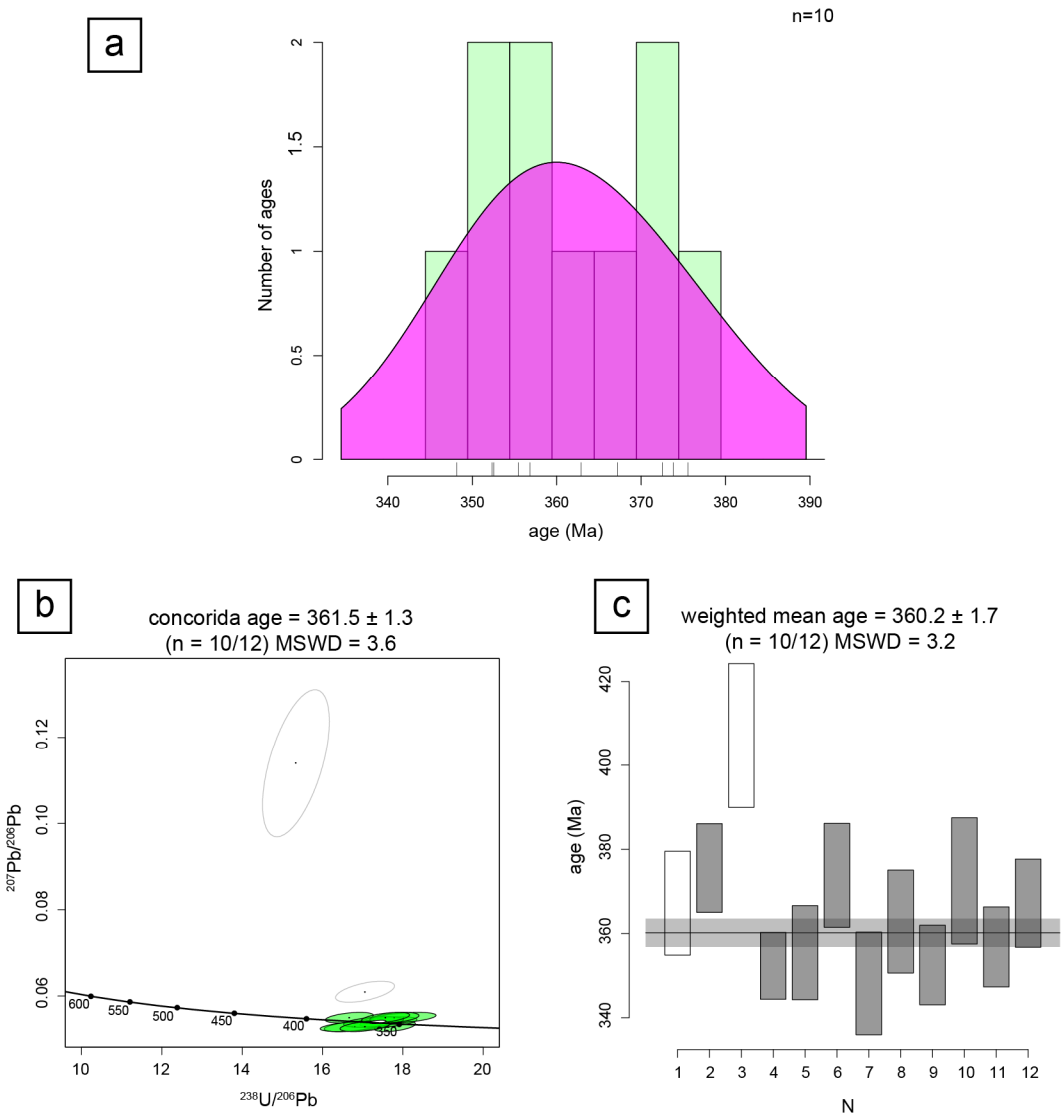

Figure 3.27 (a) KDE of all ages from IP-20-19 showing a single age peak. (b) Concordia diagram of all ages from IP-20-19 as well as concordia age calculations. White circle represents concordia age ellipse, and points along the central line are age in Ma. (c) Weighted mean age plot and calculation of the same age peak shown in (a-b). Concordia age and weighted mean age vary by less than 0.1 Ma, and errors by less than 0.01 Ma.

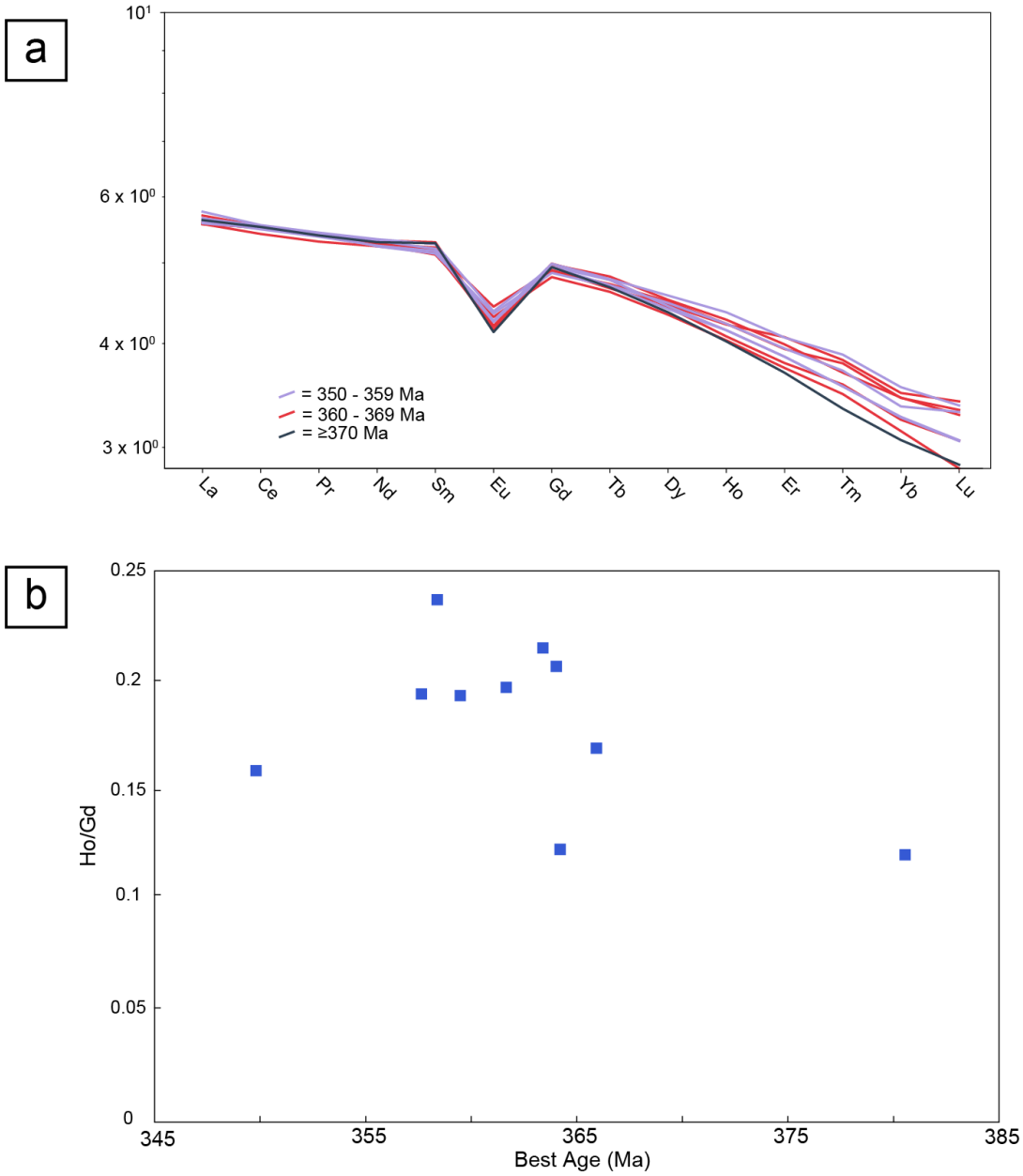

Figure 3.28. Rare earth element plots of monazite from IP-20-19. (a) Spider diagram of monazite showing a clear negative Eu anomaly and a slight spread in HREEs in monazite. Note that the minimum concentration on the vertical axis is higher than that of most other samples presented in this study. (b) The ratio of chondrite-normalized Ho to Gd plotted against monazite age. HREE enrichment appears to be steady throughout the time interval captured in monazite.

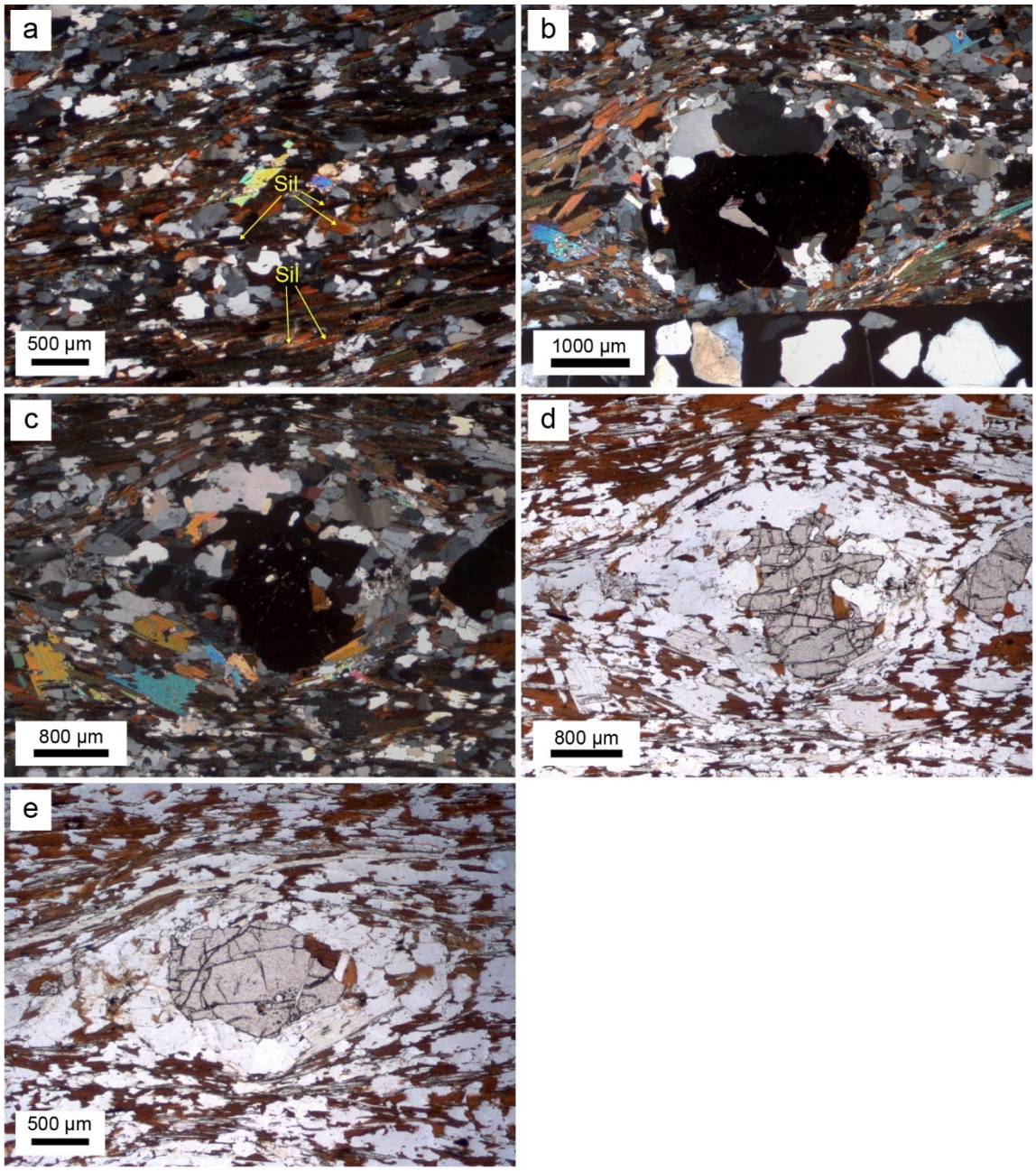

Figure 3.29 Photomicrographs of IP-18-09. (a) Representative mineralogy and foliation captured by sillimanite and muscovite. (b-e) Representative garnet from IP-18-09 showing alteration to combinations of quartz, plagioclase, and biotite.

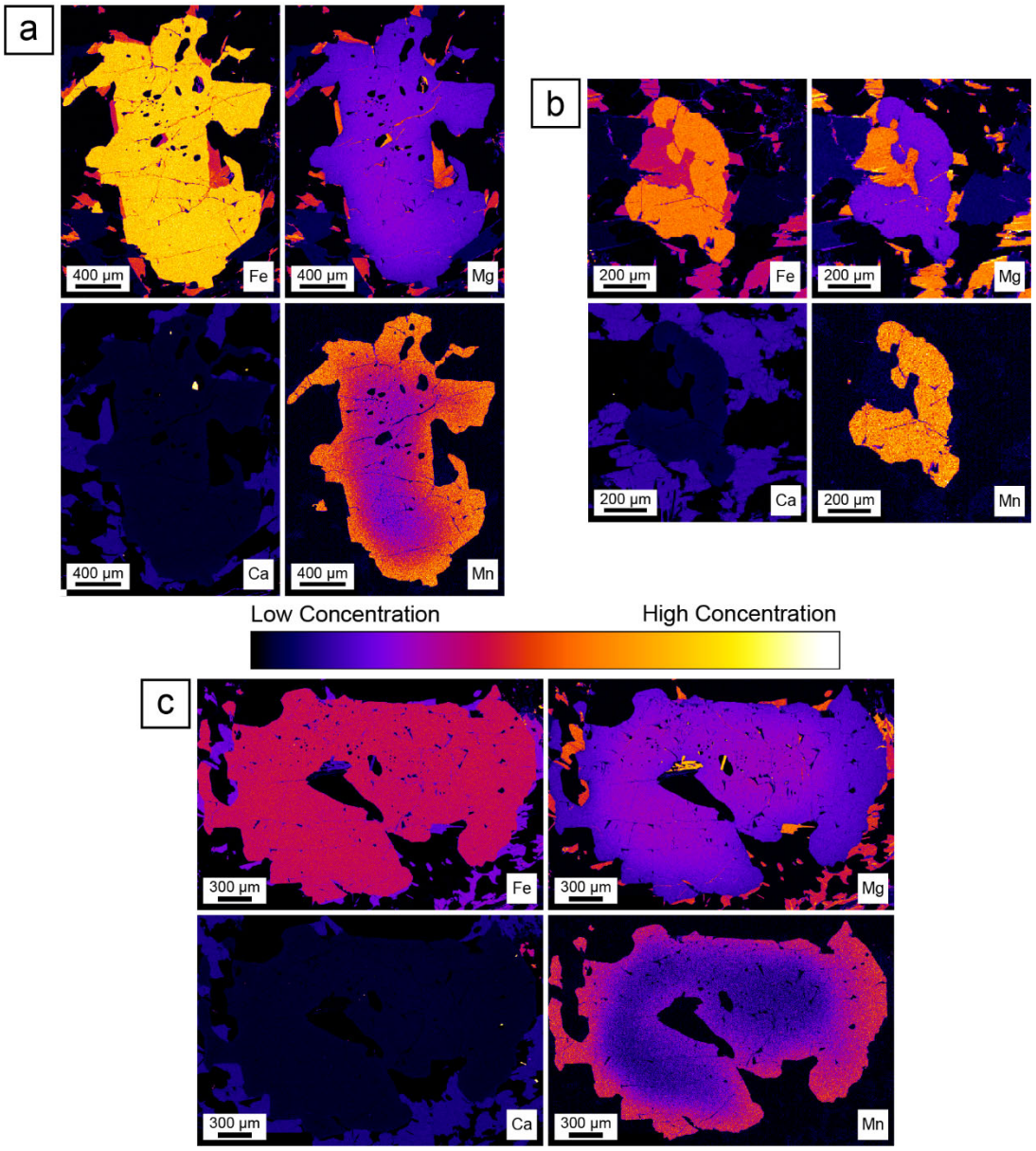

Figure 3.30 Colorized electron microprobe major element compositional maps of garnet showing homogenous cores and rims of increased Mn and decreased Mg in (a) and (c). (b) Small garnet grain with major element compositions that match the rim compositions noted in larger grains, e.g. (a), (c).

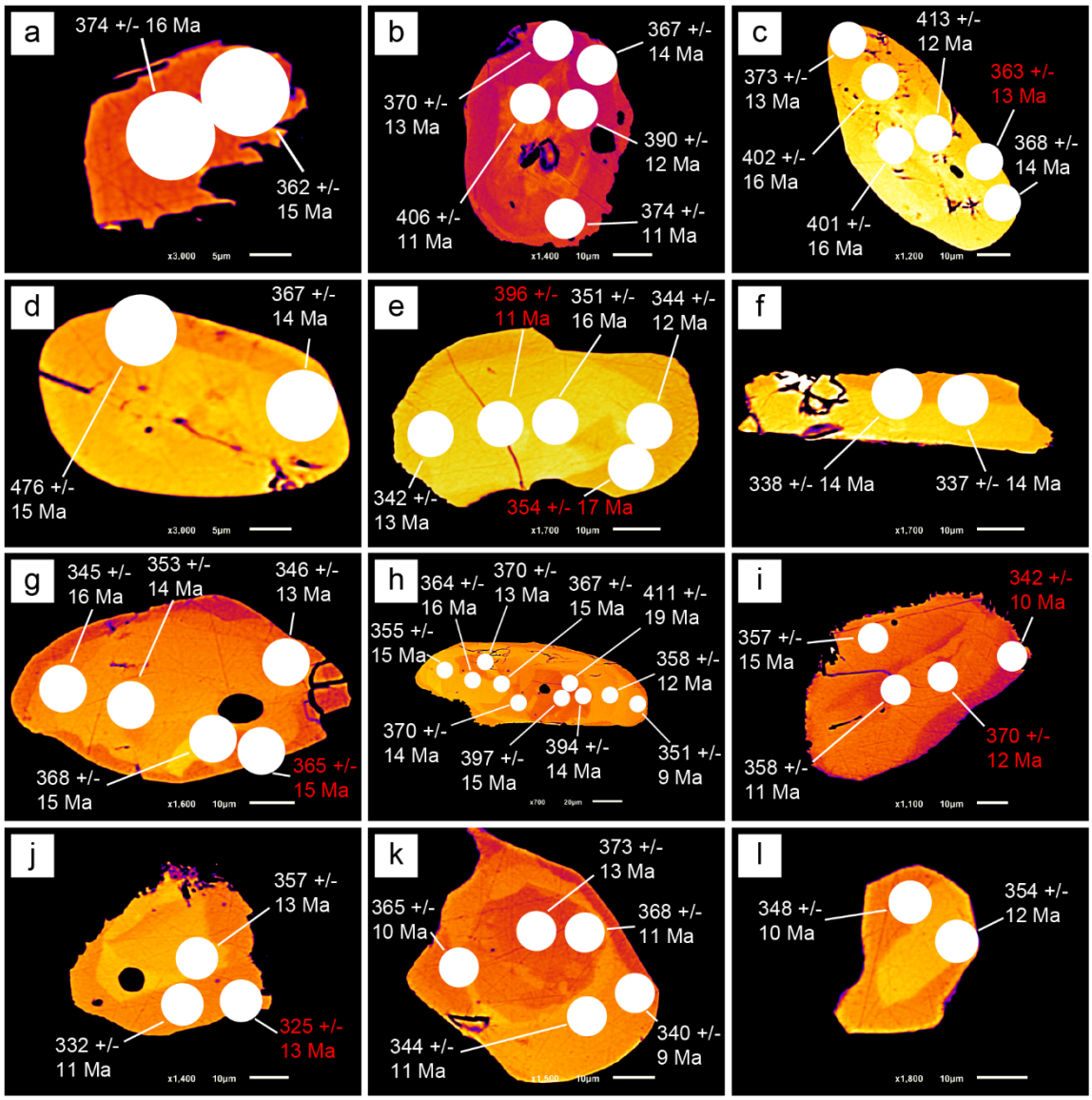

Figure 3.31 Colorized backscatter electron images taken at minimal brightness and high contrast settings of all monazite and xenotime grains analyzed from IP-18-09, as well as LASS analysis spots and resulting ages. White ages are concordant, whereas red ages are discordant and excluded from all plots (e.g. KDE, weighted means, concordia diagrams, REE plots). All grains shown are monazite, aside from (o) and (p) which are xenotime. Most grains show clear zoning patterns, though in many instances the LASS spot size of 8 µm diameter is too large to analyze within a specific zoning domain.

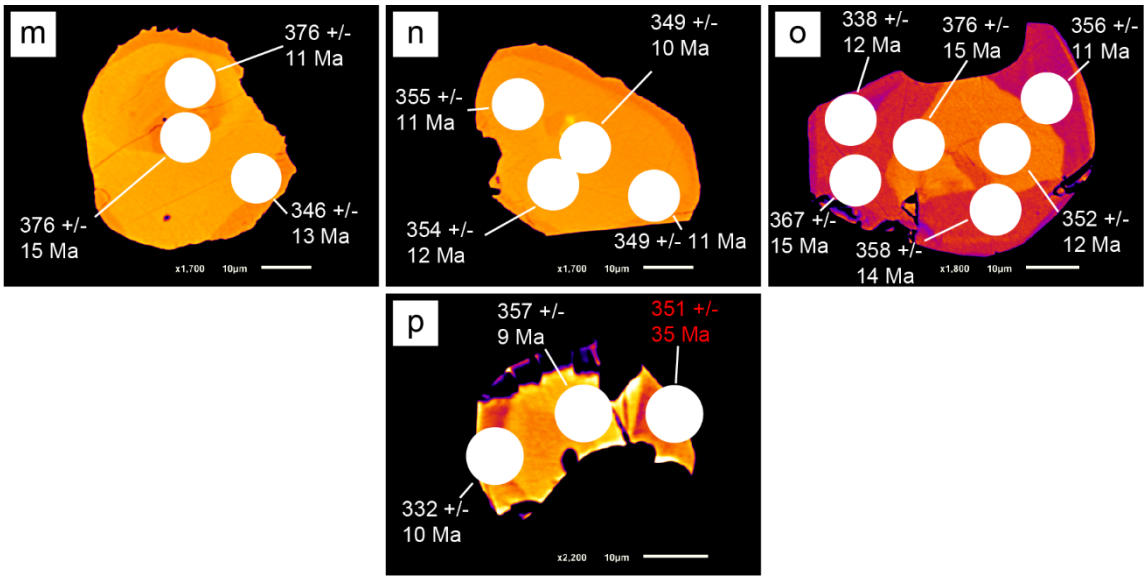

Figure 3.31 (cont.) Colorized backscatter electron images taken at minimal brightness and high contrast settings of all monazite and xenotime grains analyzed from IP-18-09, as well as LASS analysis spots and resulting ages. White ages are concordant, whereas red ages are discordant and excluded from all plots (e.g. KDE, weighted means, concordia diagrams, REE plots). All grains shown are monazite, aside from (o) and (p) which are xenotime. Most grains show clear zoning patterns, though in many instances the LASS spot size of 8 μm diameter is too large to analyze within a specific zoning domain.

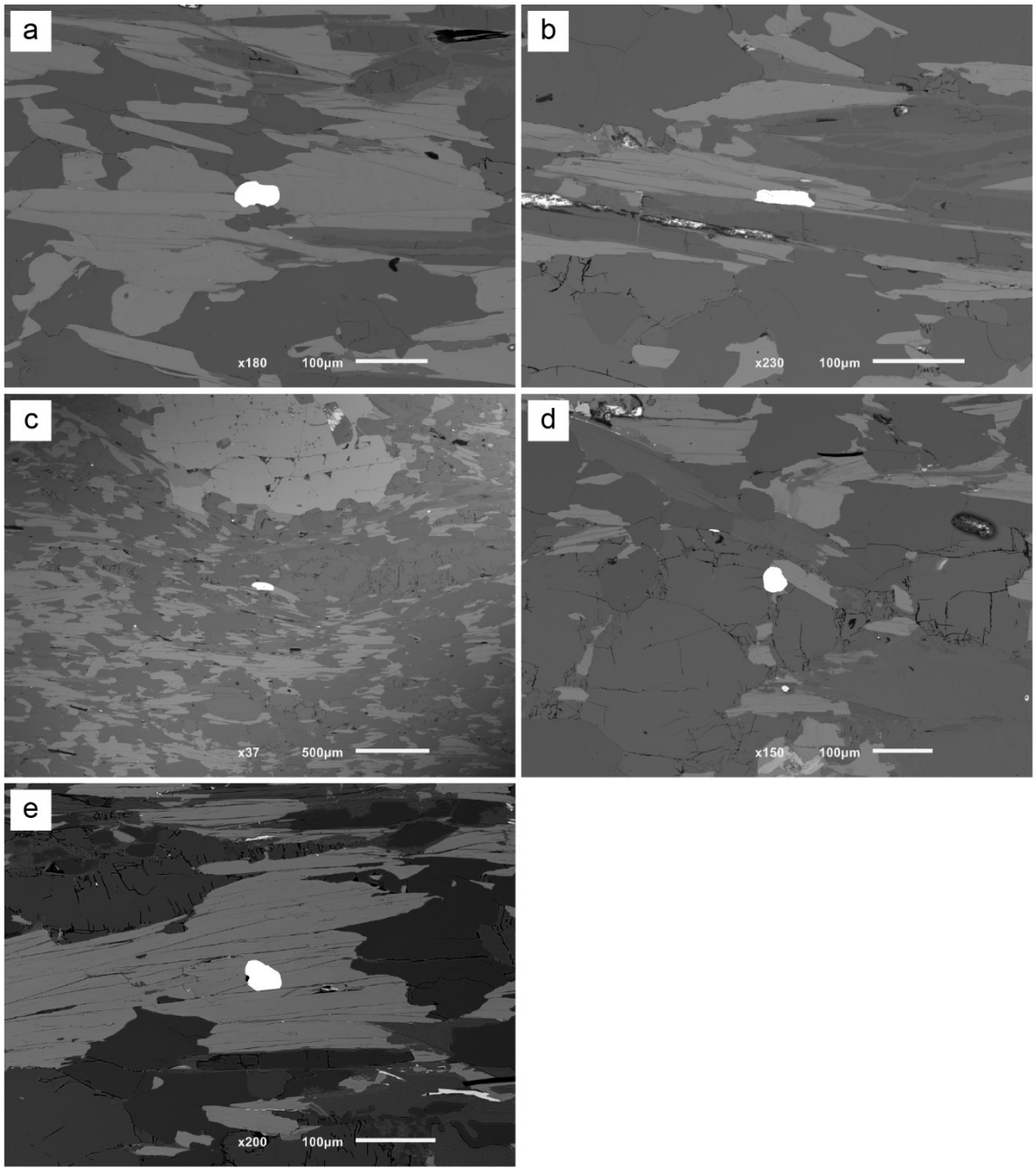

Figure 3.32 SEM backscatter electron images of monazite from IP-18-09. (a-c) Elongated monazite grains with the long axis of the grains aligned parallel or sub-parallel to foliation. (d) Slightly more rounded monazite grain with no clear relationship to foliation. (e) Monazite grain with a long axis somewhat oblique to foliation.

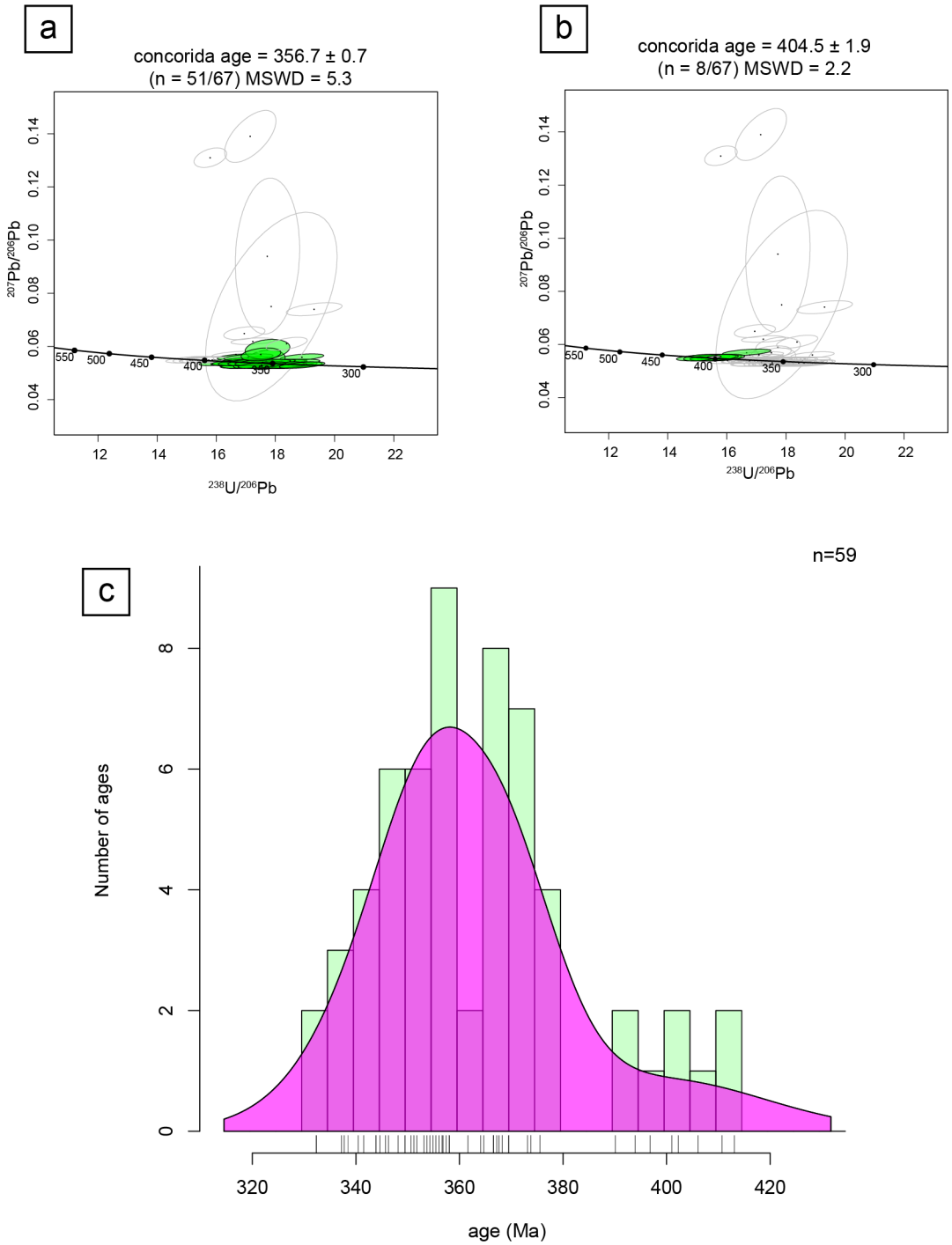

Figure 3.33 (a) Concordia diagram of all ages from IP-18-09 as well as the resulting concordia age calculations. White circle represents concordia age ellipse, and points along the central line are age in Ma. (b) KDE of all ages from IP-18-09 showing one clear age peak as well as a few slightly older grains.

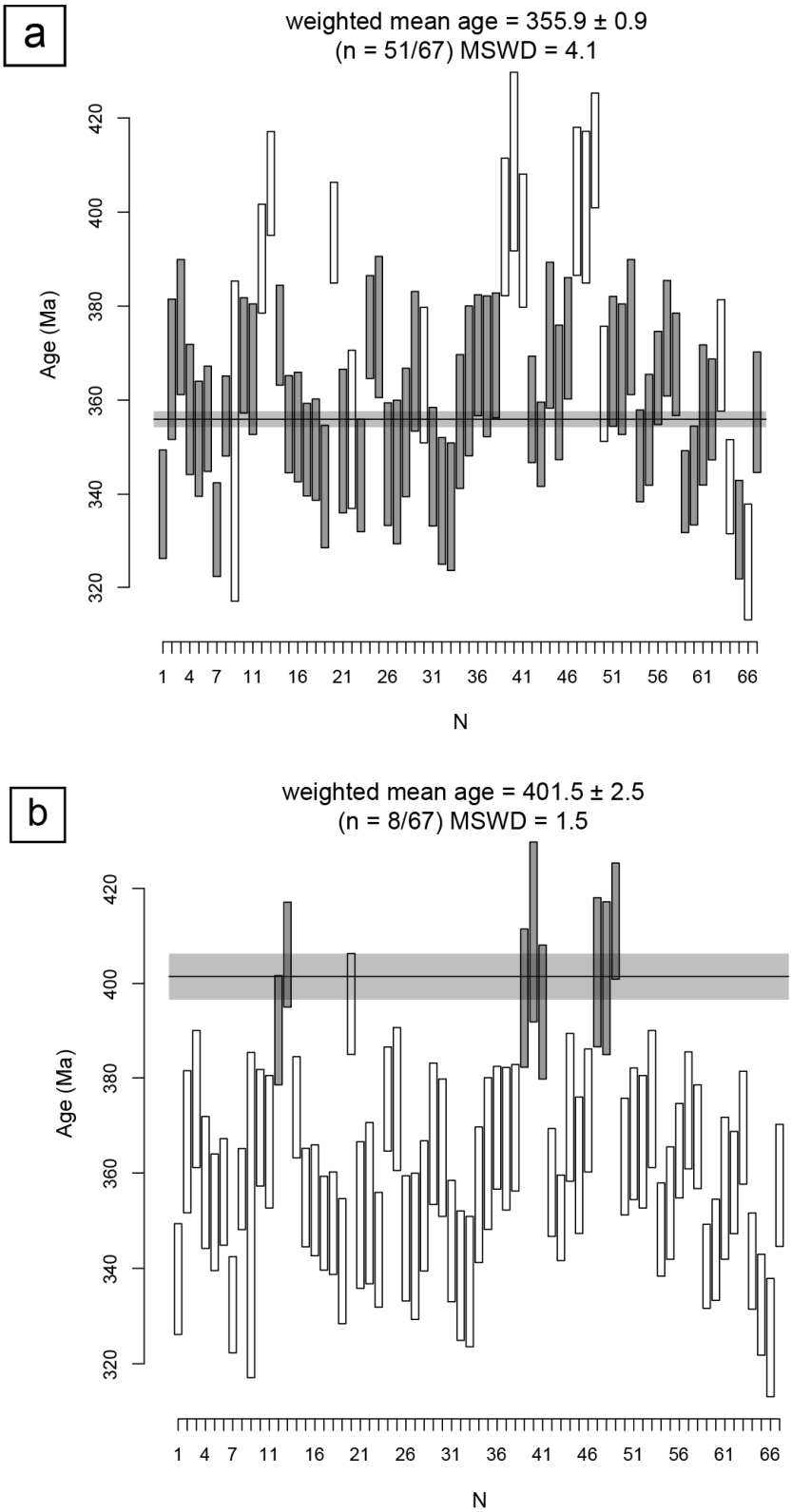

Figure 3.34 Weighted mean age plots and calculations from IP-18-09. (a) Primary age peak with 8 older ages removed. (b) Weighted mean of the 8 older ages removed from (a).

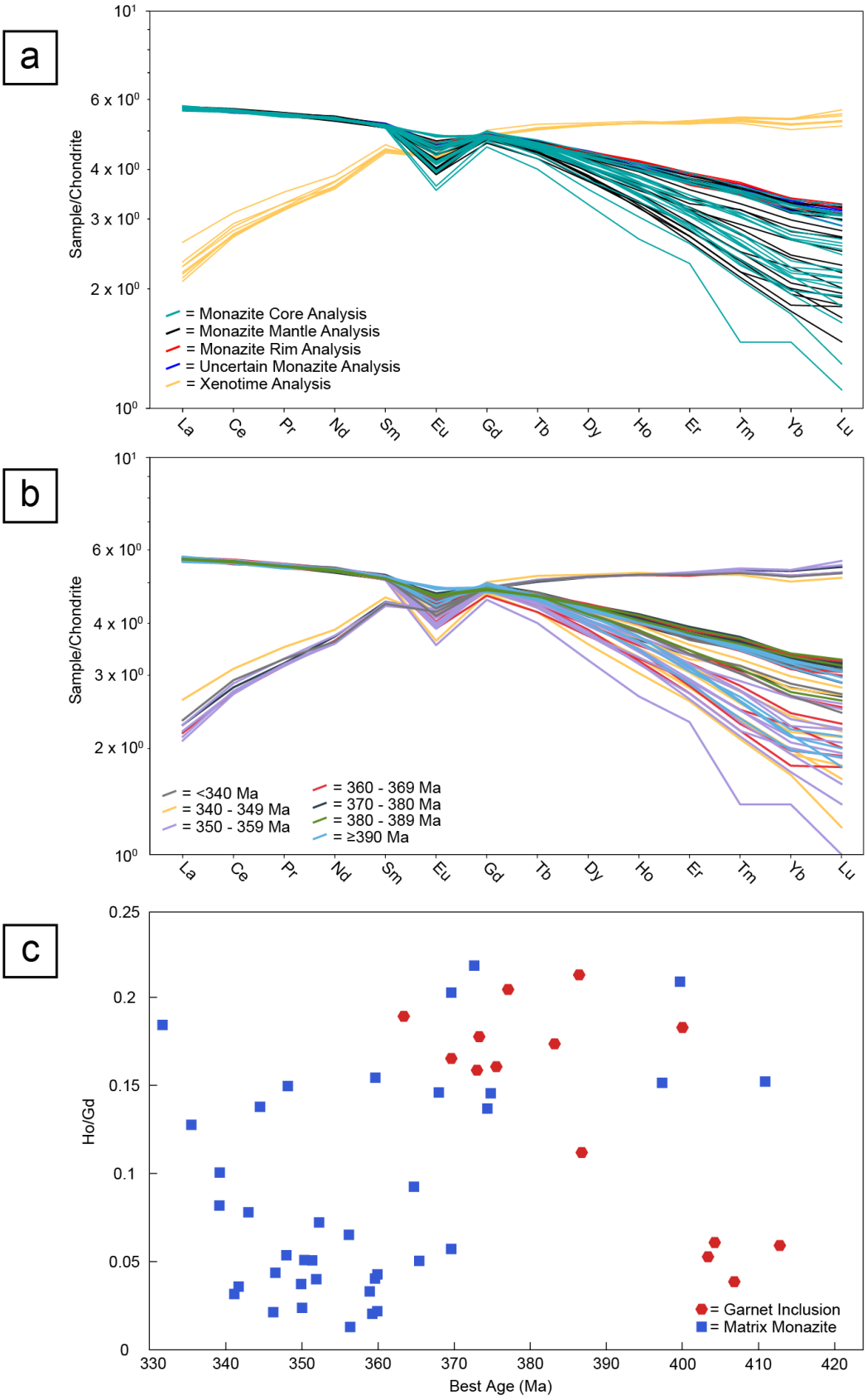
a
Sample/Chondrite
= Monazite Core Analysis
= Monazite Mantle Analysis
= Monazite Rim Analysis
= Uncertain Monazite Analysis
= Xenotime Analysis
La Ce Pr Nd Sm Eu Gd Tb Dy Ho Er Tm Yb Lu
b
Sample/Chondrite
= <340 Ma
= 340 - 349 Ma
= 350 - 359 Ma
= 360 - 369 Ma
= 370 - 380 Ma
= 380 - 389 Ma
= ≥390 Ma
La Ce Pr Nd Sm Eu Gd Tb Dy Ho Er Tm Yb Lu
c
Ho/Gd
Best Age (Ma)
= Garnet Inclusion
= Matrix Monazite

Figure 3.35 Rare earth element plots of monazite and xenotime from IP-18-09. (a) Spider diagram of monazite and xenotime, color-coded by monazite zoning domain, showing a clear negative Eu anomaly that varies by analysis in magnitude as well as a clear spread in HREEs in monazite. Patterns are difficult to discern, though monazite rim analyses only show relative enrichment in HREEs whereas monazite core analyses show a mix of HREE enrichment and depletion. (b) Spider diagram of monazite and xenotime color-coded by age. In this case, it can be seen that youngest ages have the strongest negative Eu anomaly. It remains difficult to distinguish a pattern in HREE enrichment over time. (c) The ratio of chondrite-normalized Ho to Gd plotted against monazite age. This shows the same enrichment and depletion of HREEs as in (b), but in a form that is much more clear to the observer. Garnet inclusion monazites show a trend from HREE depletion to HREE enrichment between 413 and 362 Ma, whereas matrix monazite shows a trend from HREE enrichment from ~410 to 365 Ma, a relative depletion of HREEs from 365 to 345 Ma, and a return to HREE enrichment from 345 to 330 Ma.

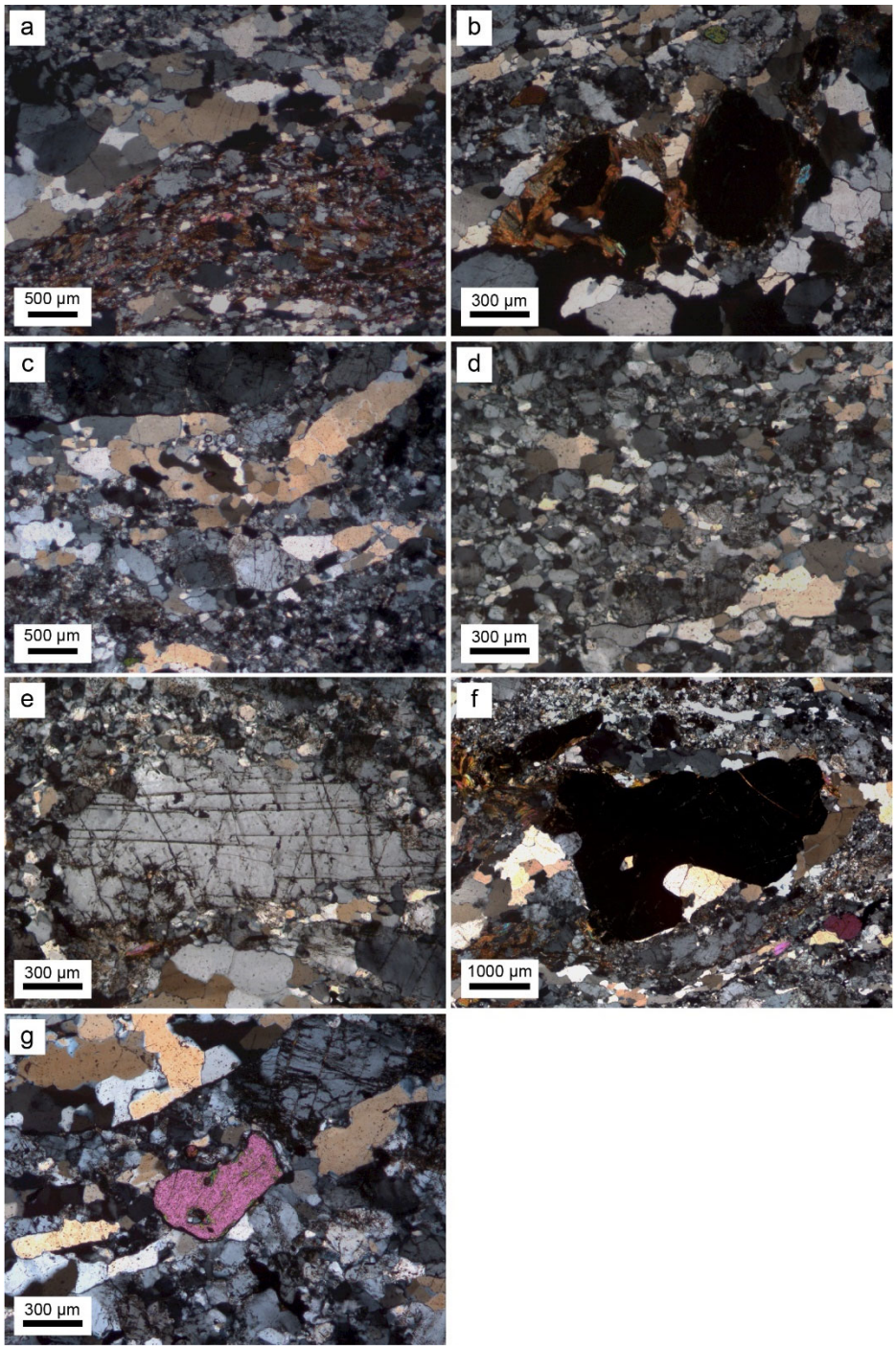

Figure 3.36 Photomicrographs of IP-19-01. (a-b) Representative mineralogy and foliation with elongated quartz and biotite grains. (b) Garnet surrounded by biotite which is interpreted to represent garnet breakdown. (c) Elongated quartz ribbons that define foliation. (d) example of recrystallized quartz and feldspar present throughout much of IP-19-01. (e) Microcline porphyroclast breaking down to finer-grained quartz and feldspar. (f) Garnet from IP-19-01, showing representative anhedral shape common in this sample. (g) Example monazite grain in cross-polarized light, showcasing the large grain size of monazite in IP-19-01.

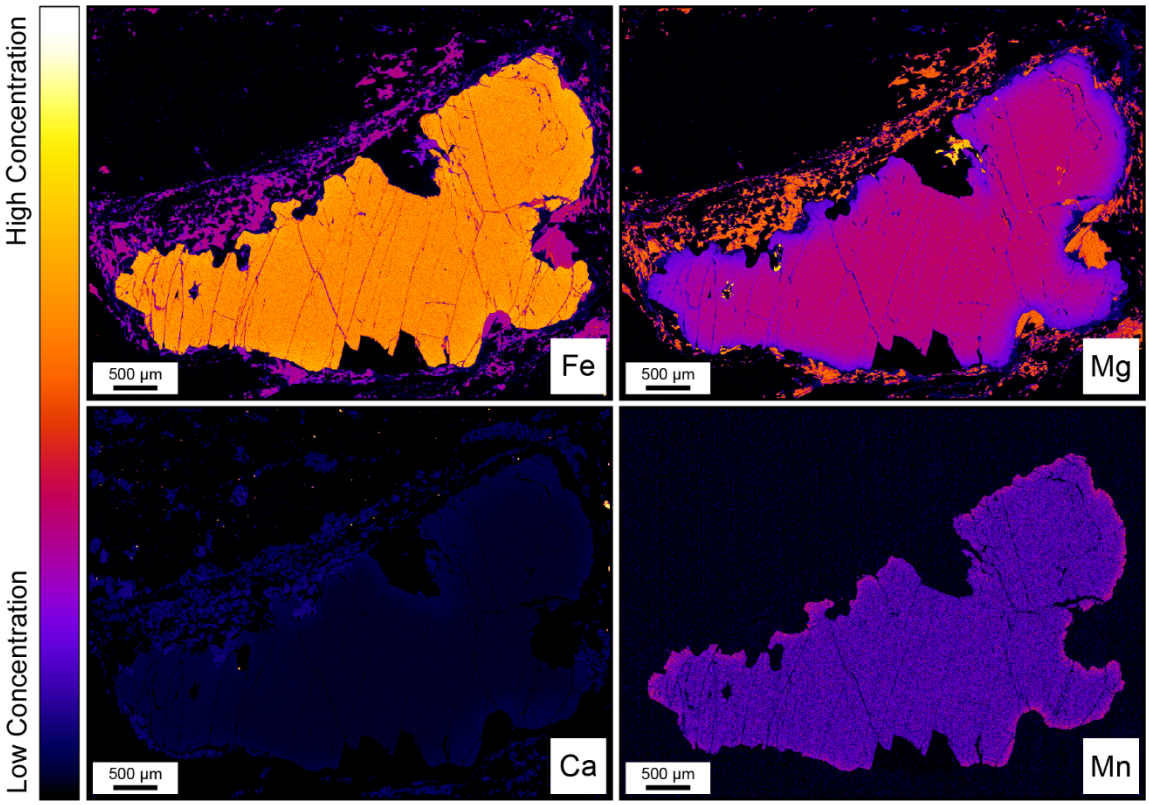

Figure 3.37 Colorized electron microprobe major element compositional map of garnet showing anhedral shape, homogenous cores, and rims of increased Mn and Ca as well as decreased Mg.

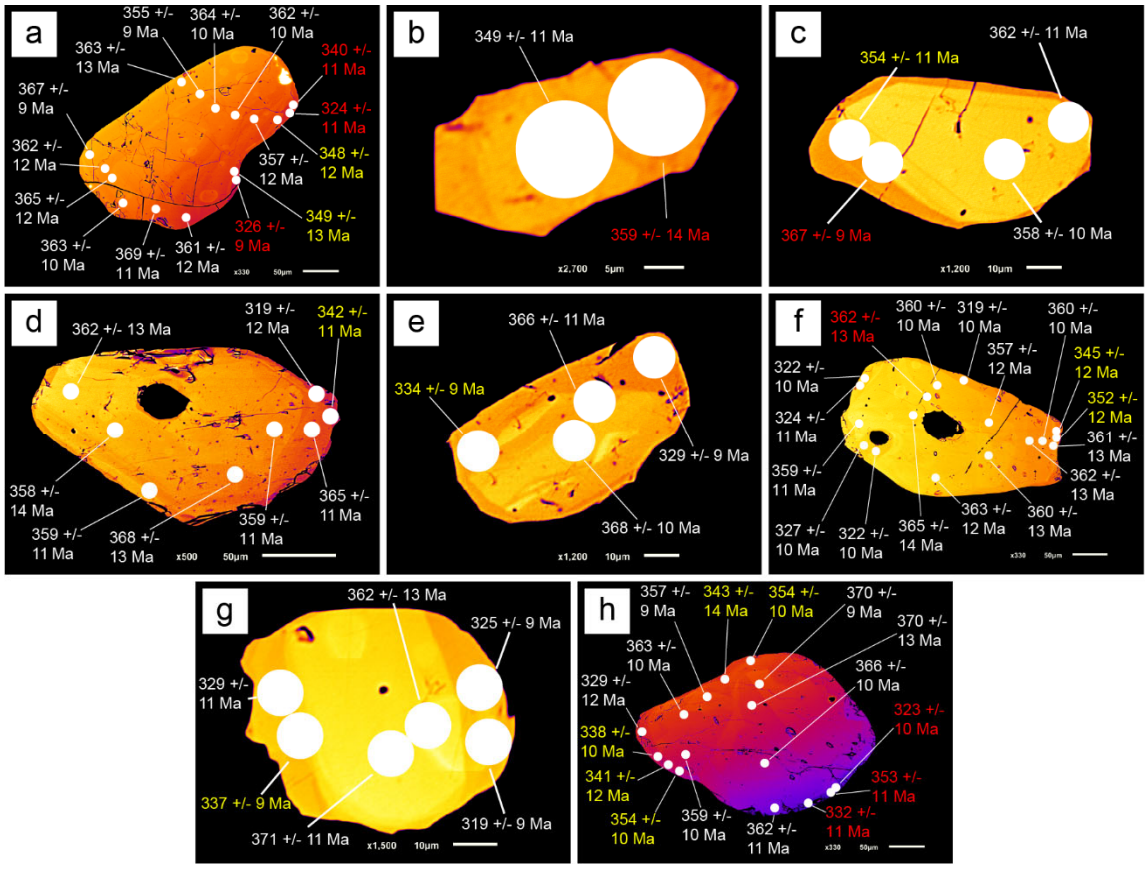

Figure 3.38 Colorized backscatter electron images taken at minimal brightness and high contrast settings of all monazite and xenotime grains analyzed from IP-19-01, as well as LASS analysis spots and resulting ages. White ages are concordant, yellow ages are concordant but excluded from age calculations due to potential mixing of domains, and red ages are discordant and excluded from all plots (e.g. KDE, weighted means, concordia diagrams, REE plots). Concordant ages that were removed from age calculations were chosen to be removed only on the basis of the analysis spot crossing between two distinct zoning domains.

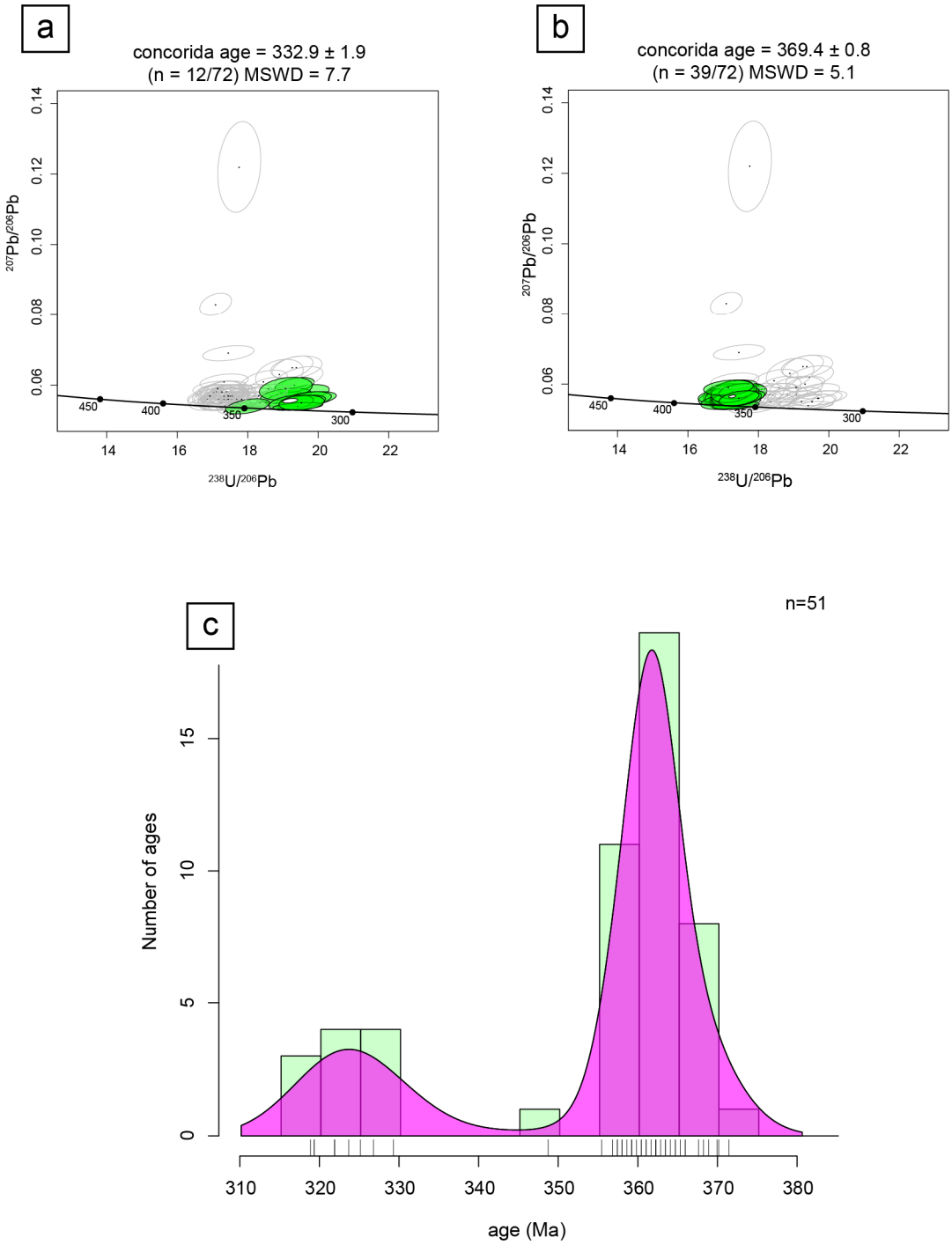

Figure 3.39 (a) Concordia diagram of all ages from IP-19-01. No concordia age was calculated due to two clearly distinct age populations. Points along the central line are age in Ma. (b) KDE of all concordant ages from IP-19-01 aside from those ages removed from consideration for including a mix of multiple zoning domains. Two distinct age peaks are clearly visible at ~328 and 368 Ma.

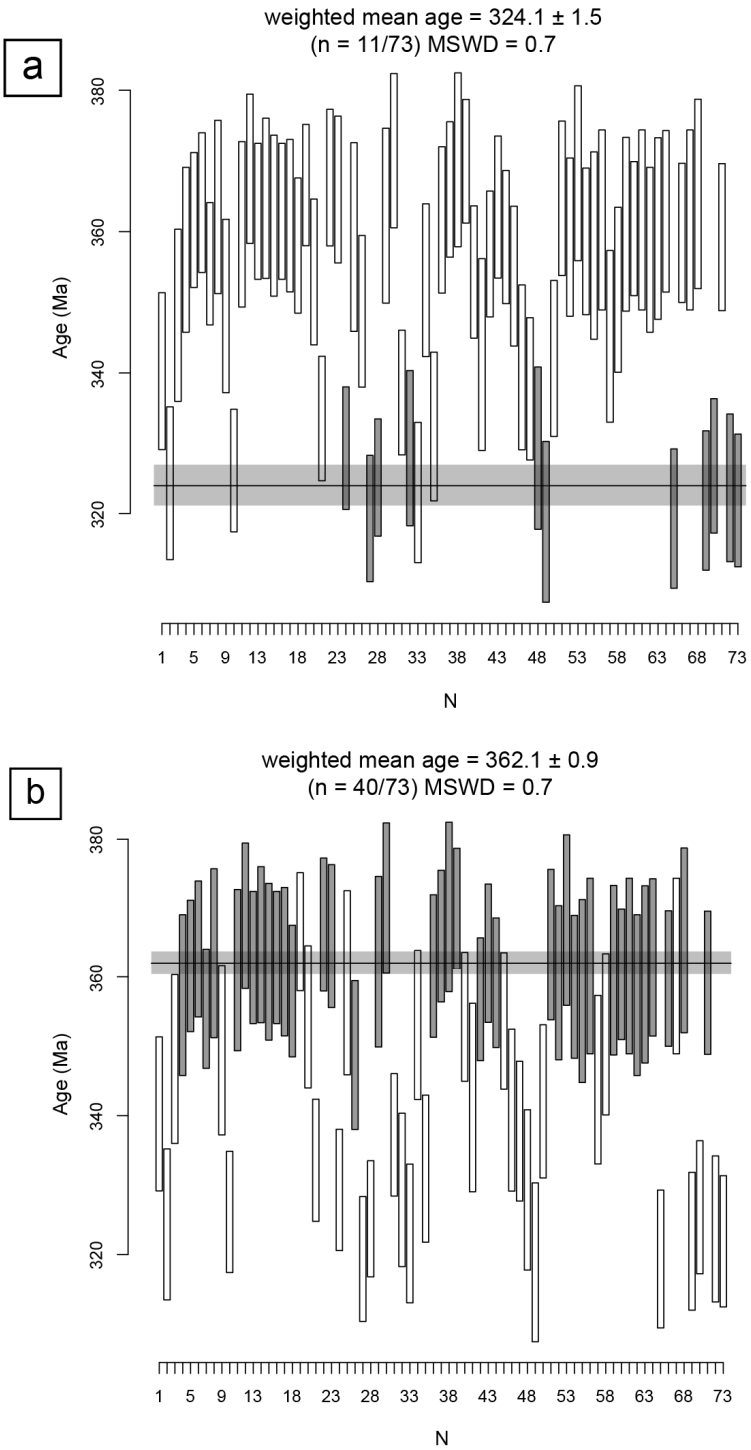

Figure 3.40 Weighted mean age plots and calculations from IP-19-01. (a) Younger age peak skewed slightly older than the center of the peak. (b) Weighted mean of the older age peak.

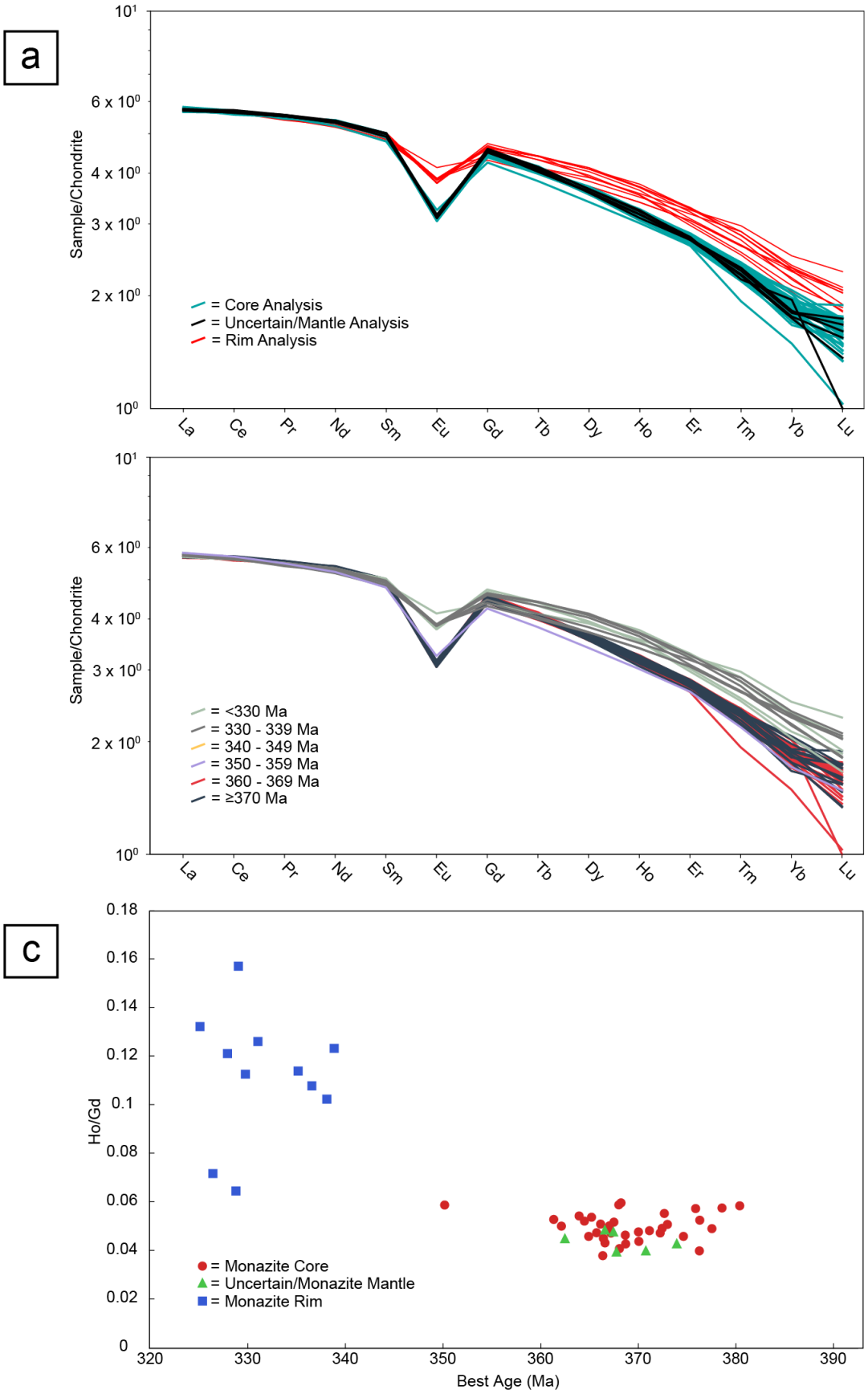
a
Sample/Chondrite
= Core Analysis
= Uncertain/Mantle Analysis
= Rim Analysis
La
Ce
Pr
Nd
Sm
Eu
Gd
Tb
Dy
Ho
Er
Tm
Yb
Lu
= <330 Ma
= 330 - 339 Ma
= 340 - 349 Ma
= 350 - 359 Ma
= 360 - 369 Ma
= ≥370 Ma
c
Ho/Gd
= Monazite Core
= Uncertain/Monazite Mantle
= Monazite Rim
Best Age (Ma)

Figure 3.41 Rare earth element plots of monazite from IP-19-01. (a) Spider diagram of monazite, color-coded by monazite zoning domain, showing a clear negative Eu anomaly with much higher magnitude in mantle and core analyses than in rims. Additionally, a clear pattern can be seen with monazite rim analyses showing more enriched HREEs than monazite mantle and core analyses. (b) Spider diagram of monazite color-coded by age. Because cores are generally older than rims, the same pattern in (a) is present when analyzed by age, with young ages showing lower magnitude Eu anomalies and more enriched HREEs compared to older ages. (c) The ratio of chondrite-normalized Ho to Gd plotted against monazite age. Older monazite cores and mantles show more depleted HREEs compared to younger rims which show more HREE enrichment.

CHAPTER 4. DISCUSSION & CONCLUSIONS

4.1 Interpretation of age data

All monazite in sample SK440 from the CHMGL thrust sheet show similar Taconic ages, and these are interpreted as recording either prograde or peak Taconic metamorphism. Though the majority of monazite analyzed in this sample are garnet inclusions, one matrix monazite grain was located within kyanite. The presence of sillimanite primarily within garnet and kyanite only outside of garnet suggests that kyanite grew in place of sillimanite during post-Taconic cooling. Therefore, the monazite located within kyanite (Fig. 3.3n) indicates that kyanite growth occurred after monazite growth, thereby constraining monazite growth to have occurred before cooling and alteration of sillimanite to kyanite. Sample BR-20-10, collected from the same thrust sheet, return three age modes. The older two age modes are interpreted as recording either prograde or peak Neoacadian metamorphism given their age ranges. Because the younger age mode comprises mostly xenotime ages and a few monazite ages, as well as due to the replacement of garnet by quartz, biotite, and plagioclase noted in this sample, this young age mode is interpreted to record xenotime growth as Y is released during garnet breakdown (e.g. Spear and Pyle, 2002). This is supported by monazite showing alteration around the rims in many instances, as well as a slight trend from more depleted HREE to more enriched HREE with younger age, which is interpreted to record the transition to garnet breakdown conditions over time. Monazite in sample BR-20-14, collected from within the BFZ, only records Taconic ages however. Though there is significant evidence for retrograde metamorphism in this sample, the monazite ages must record either prograde or peak Taconic metamorphism because monazite alteration did not appear to include an element of recrystallization to produce new ages.

Monazite from within garnet and in the matrix in sample IP-18-05 return similar ages, indicating that garnet growth occurred coeval with monazite growth. Garnet in this sample shows alteration to quartz, biotite, and plagioclase as well as enrichment of Mn near the rim that indicate resorption following garnet growth. The Neoacadian age mode recorded by monazite is therefore interpreted as prograde Neoacadian metamorphism, whereas younger xenotime growth (329 – 338 Ma) likely corresponds to the timing of

retrograde garnet resorption and alteration, as Spear and Pyle (2002) suggest that garnet breakdown can release enough Y to stabilize xenotime during retrogradation. Monazite in sample IP-20-19, collected from the Sauratown Mountains window, also return a single Neoacadian age mode. Garnet resorption textures and monazite alteration to apatite indicate retrogradation, and monazite analyses show enrichment in HREE, likely as a result of garnet resorption. Thus, monazite in IP-20-19 captures retrogradation in the Sauratown Mountains window during the Neoacadian, likely influenced by the BFZ due to its close proximity.

In the Brindle Creek thrust sheet, monazite from IP-18-09 shows a single Neoacadian age mode with a few slightly older ages. REE patterns in monazite from IP-18-09 show relative enrichment in HREE from ~410 to 365 Ma, which is interpreted as conditions prior to significant garnet growth. Monazite with ages ranging from 365 to 345 Ma show a depletion in HREE, however, which is interpreted as the timing of garnet growth. Monazite analyses with ages younger than 345 Ma show a transition towards HREE enrichment, which is interpreted as the onset of garnet resorption. Using these interpretations, the majority of monazite ages in IP-18-09 are interpreted to record Neoacadian prograde and peak metamorphism, followed by post-peak cooling. Further east in the Brindle Creek thrust sheet, monazite in IP-19-01 records both a Neoacadian and an early Alleghanian age mode in cores and rims, respectively. Monazite analyses with Neoacadian ages show depleted HREEs, which suggest that these ages record the timing of garnet growth. Additionally, garnet in IP-19-01 shows a lack of prograde growth zoning, which is interpreted to suggest that prograde growth zoning was diffused as a result of prolonged high temperatures in the IP during peak Neoacadian metamorphism. Thus, Neoacadian monazite core ages in IP-19-01 record prograde Neoacadian metamorphism. Alleghanian monazite ages in IP-19-01 show enriched HREE, however, which suggests garnet breakdown at this time. This is supported by resorption textures in garnet in IP-19-01 as well as enriched Mn and Ca in garnet rims. Therefore, monazite rims record retrograde Alleghanian metamorphism.

4.2 Integration of LASS results with P-T-t data

The CHMGL thrust sheet lies in the intersection of the Taconic and Neoacadian metamorphic cores of the southern Appalachian orogen. This is reflected throughout the CHMGL thrust sheet as Taconic metamorphism is widespread with less common, interspersed Neoacadian metamorphism. Goldberg and Dallmeyer (1997) reported garnet and hornblende Sm-Nd and Rb-Sr ages that range from 480 – 440 Ma in the CHMGL thrust sheet. From the same approximate structural level, Merschat et al. (2017) also report two metamorphic zircon U-Pb ages of 450 ± 5 Ma and 424 ± 4 Ma. Additionally, Miller et al. (2006) determined a zircon U-Pb age of 459 ± 1 Ma from eclogites in the CHMGL, interpreted as Taconic eclogite-facies metamorphism. With a concordia age of 458.8 ± 0.8 Ma and a weighted mean age of 458.2 ± 1.1 Ma (Fig. 3.4), sample SK440 records the same time for peak Taconic metamorphic event. These ages indicate that this part of the CHMGL did not experience Neoacadian metamorphism. Monazite within garnet and in the matrix show the same age range, which is interpreted to indicate that garnet growth was coeval with or subsequent to the metamorphic event recorded by monazite. Therefore, the HREE enrichment noted in monazite (Fig. 3.5) in SK440 is not interpreted to indicate garnet breakdown.

Despite the lack of any Neoacadian monazite in SK440, some Neoacadian metamorphism has affected the CHMGL thrust sheet to the northeast. North of the Grandfather Mountain window, Abbott and Raymond (1984) noted multiple metamorphic events recorded by metapelites and amphibolites in the Ashe Metamorphic suite including both Taconic and Neoacadian metamorphism (M2 and M3, respectively, of that study). Farther southwest, Merschat et al. (2017) reported metamorphic zircon rim ages of 365-338 Ma. Although these localities record Neoacadian metamorphism immediately northwest of the BFZ, both deformation and metamorphism associated with the Neoacadian orogeny are most intense near the BFZ and decrease in intensity westward (Merschat, 2009), indicating that the westernmost extent of Neoacadian metamorphism lies between the CHMGL fault system and the BFZ. Sample BR-20-10, located just northeast of the Grandfather Mountain window (Fig. 2.1), records three age peaks: one early Neoacadian peak at 372.9 ± 0.8 Ma, one slightly later Neoacadian peak

at 357.1 ± 2.0 Ma and one younger age peak of 335.1 ± 2.0 Ma (Fig. 3.10). The older two ages are similar to the published age range of Neoacadian metamorphism in the CHMGL thrust sheet, which indicates that the westernmost extent of Neoacadian metamorphism reaches at least ~10 km northwest of the BFZ in northwestern NC. Interpreting the younger age mode as recording metamorphism during cooling is also consistent with hornblende $^{40}Ar/^{39}Ar$ ages of 347 Ma and 345 Ma from the northwestern CHMGL (Levine et al., 2018, 2020) which constrain cooling of these rocks through ~550 °C at that time.

In the immediate footwall of the BFZ, monazite from sample BR-20-14 yields a single peak Taconic age distribution, with a weighted mean age of 452.8 ± 2.6 Ma and a concordia age of 461.8 ± 1.9 Ma (Fig. 3.16). Garnets in this sample are anhedral with asymmetric tails and retrograde chlorite (Fig. 3.13) indicative of greenschist retrogression following Taconic prograde garnet growth (early Alleghanian ductile reactivation of the BFZ?). Monazite REE patterns indicate relative HREE depletion (Fig. 3.17), with a slight trend towards more depleted HREE with younger ages, which may be indicative of conditions shifting towards garnet growth. This is consistent with a single older age collected from monazite within garnet (474 ± 15 Ma), which places a constraint on the maximum age of garnet growth. Because monazite ages record only Taconic metamorphism, we interpret monazite in BR-20-14 to record metamorphism during early BFZ motion. The presence of chlorite between garnet fragments indicates that this sample also records retrograde metamorphism, likely from Alleghanian reactivation of the BFZ which is known to have occurred under greenschist facies conditions.

To the southeast and structurally above the BFZ, *P-T* conditions in the Brevard thrust sheet in North Carolina have been estimated at 520 – 670 °C and 5.1 – 5.3 kbar (Bier et al., 2002), interpreted as contemporaneous with monazite and zircon growth during Neoacadian metamorphism at ~ 350 Ma. In the same region, Yanagihara (1994) obtained peak P-T conditions ranging from 625 – 700 °C and 3.5 – 8.0 kbar based on mineral assemblages and metamorphic grade as well as observations of partial melting. Monazite ages from IP-18-05, located in the immediate footwall of the BCFZ in northwestern NC (Fig. 2.1), yield a single peak distribution with a concordia age of 357.9

± 0.5 and a weighted mean age of 356.4 ± 0.7 (Fig. 3.21), which is interpreted to represent the timing of prograde metamorphism in the Brevard thrust sheet. The single monazite age mode is consistent with the interpretations of Kalbas (2003) that both sides of the BCFZ have experienced Neoacadian sillimanite grade peak metamorphism with no retrograde overprinting. Importantly, the presence of a single Neoacadian event distinguishes the Brevard thrust sheet from the CHMGL thrust sheet to the northwest, with the BFZ perhaps representing a key structural boundary during the Neoacadian, as hypothesized by Hatcher and Merschat (2006).

Despite geochronologic evidence for a single peak prograde metamorphic event, garnets in sample IP-18-05 are anhedral and show increasing Mn and decreasing Mg localized to the rim (Fig. 3.18, 3.19), and thus they have likely experienced some resorption following peak metamorphism similar to observations of Gatewood et al. (2015). Xenotime from the matrix of IP-18-05 yields an age of 329-338 Ma, which may constrain the timing of garnet breakdown. Although no hornblende $^{40}Ar/^{39}Ar$ ages have been reported from the Brevard thrust sheet in this part of North Carolina, the lack of an Alleghanian monazite age peak in IP-18-05 indicates that, at this structural level, only one prograde metamorphic event is preserved. Although matrix monazite HREE analyses show a range of relative enrichment values, in monazites with ages of 374 Ma – 342 Ma, monazite included in garnet typically shows slightly more enriched HREEs compared to matrix monazite, which may indicate that matrix monazite grew with garnet during prograde and peak metamorphism (Fig. 3.22).

At the northeastern end of the Brevard thrust sheet, the Sauratown Mountains window preserves pre-Paleozoic basement gneiss structurally beneath the IP, and these rocks have traditionally been interpreted to have experienced peak metamorphism during the Taconic orogeny at ~450 Ma (Hatcher, 1988; McConnell, 1988). However, monazite from sample IP-20-19 yields a Neoacadian age peak, with a weighted mean age of 360.2 ± 1.7 Ma and concordia age of 361.5 ± 1.3 Ma (Fig. 3.27). The anhedral shape of garnet in this sample indicates resorption (Fig. 3.33e, f), which is supported by the enrichment of HREEs shown in monazite compared to monazite HREE profiles from other samples in this study. Monazite altering to apatite (Fig. 3.25) is consistent with retrograde

conditions, as monazite has been shown to alter to apatite during low-grade metamorphism in the presence of fluids (Broska et al., 2005) or in granitic rocks under amphibolite facies conditions (Finger et al., 1998).

In the Brindle Creek thrust sheet, which is the southeasternmost thrust sheet examined in this study, monazite from sample IP-18-09 records a Neoacadian peak with a concordia age of 356.7 ± 0.7 Ma and a weighted mean age of 355.9 ± 0.9 Ma as well as a minor cluster of pre-Neoacadian ages with a concordia age of 404.5 ± 1.9 and a weighted mean age of 401.5 ± 2.5 Ma (Fig. 3.33, 3.34). Gatewood (2007) interpreted peak metamorphism in the Brindle Creek thrust sheet, near the BCFZ to have occurred between 360 and 340 Ma, which is consistent with the major peak of monazite growth recognized in IP-18-09. Also, similar to IP-18-05 on the west side of the BCFZ, this lack of younger ages in IP-18-09 is consistent with the interpretation of a single prograde metamorphic event with no retrograde overprinting on either side of the BCFZ (Kalbas, 2003). Also, some monazite grains in IP-18-09 as young as 362 Ma are included in garnet, which indicates that garnet growth began at or before this time, likely during prograde metamorphism. The lack of prograde growth zoning preserved in garnet (Fig. 3.30), however, suggests that garnet has experienced temperatures sufficiently high to allow original growth zoning to be lost to internal diffusion.

Peak *P-T* conditions are interpreted by previous studies to range from 630 – 850 °C and 4.2 – 8.7 kbar in the Brindle Creek thrust sheet (Merschat, 2003; Wilson, 2006; Gatewood, 2007). Given that garnet radii in IP-18-09 are up to 1.5 mm in length, the uppermost *T* of 850 °C would need to be sustained for only ~ 4 m.y. to completely homogenize compositional zoning (e.g., Caddick et al., 2010). However, using the timing of peak metamorphism in the Brindle Creek thrust sheet interpreted by Gatewood (2007) of 360 – 340 Ma, temperatures would need to be at or above ~775 °C for the 20 m.y. the Brindle Creek thrust sheet experienced peak *P-T* conditions to homogenize garnet zoning (e.g., Caddick et al., 2010). Below ~750 °C, the amount of time required to homogenize garnet zoning exceeds 50 m.y. (e.g., Caddick et al., 2010), indicating that it is unlikely for peak *P-T* to have remained below 750 °C for the entirety of the Neoacadian. Furthermore, hornblende $^{40}Ar/^{39}Ar$ ages near the BCFZ and near the center of the Brindle Creek thrust

sheet yield dates of ~345 Ma (Spencer et al., 2021), indicating that by this time, the central to western half of the Brindle Creek thrust sheet in NC had cooled below ~550 °C. This further constrains the duration of peak Neoacadian metamorphism from 20 m.y. interpreted by Gatewood (2007) to <15 m.y. At this length of time, models of major element diffusion in garnet by Caddick et al. (2010) suggest that peak *T* must exceed ~790 °C to completely homogenize zoning. Following peak metamorphism, retrograde *P-T* conditions of 535 – 650 °C and 4.6 – 6.7 kbar were calculated for the Brindle Creek thrust sheet (Wilson, 2006; Gatewood, 2007), likely reflecting post-peak cooling and unroofing prior to ~345 Ma.

REE compositions in monazite from IP-18-09 also supports a progression from prograde Neoacadian metamorphism to post-peak cooling for the Brindle Creek thrust sheet. Monazite analyses with ages ranging from ~410 to 365 Ma record enrichment in HREE (Fig. 3.35), which is interpreted as conditions in which no garnet growth occurred, allowing monazite to incorporate a much larger component of HREE compared to monazite growing coeval with garnet growth. Monazites analyses with ages from 365 to 345 Ma are accompanied by a progressive HREE depletion as ages get younger (Fig. 3.35). This depletion in HREE is interpreted to be the result of garnet growth that consumes HREE, limiting the availability for incorporation into monazite. However, in monazites that yield ages from 345 Ma to 330 Ma, a progressive HREE enrichment is recorded with decreasing age (Fig. 3.35), which is interpreted to be indicative of garnet breakdown during this time which released HREE into the matrix. This timing of garnet breakdown corresponds with hornblende $^{40}Ar/^{39}Ar$ dates that record cooling of the Brindle Creek thrust sheet at ~345 Ma (Spencer et al., 2021). One potential interpretation is that heat from the Brindle Creek thrust sheet was rapidly transferred to the Brevard thrust sheet upon emplacement, causing retrograde conditions to develop at high temperature in the eastern IP near the BCFZ as the western IP experienced prograde conditions.

In the eastern part of the Brindle Creek thrust sheet, near the southern border of the Newton window, Gilliam (2010) interpreted metamorphic/deformational events at 360 Ma, 345 Ma, and 330 Ma based on U-Pb metamorphic zircon and monazite ages and

suggested that both within and outside of the Newton window, peak metamorphism occurred between 360 and 345 Ma. Monazite ages from sample IP-19-01, collected near the CPS just south of the Newton window (Fig. 2.1), yield two metamorphic events with monazite growth, however the more prominent of these two events occurred at ~362 Ma which is consistent with the earliest event recognized by these previous studies (Fig. 3.39). The younger metamorphic event recorded in monazite from IP-19-01 occurred at ~324 Ma, which is consistent with the youngest metamorphic event interpreted by Gilliam (2010).

The peak Neoacadian metamorphic event documented by the monazite ages in the Brindle Creek thrust sheet was previously interpreted to have reached sillimanite-grade conditions (Merschat, 2003; Gatewood, 2007; Gilliam, 2010; Merschat et al., 2017). Gilliam (2010) calculated peak *P-T* conditions that range from 620 °C, 3.6 kbar to 710 °C, 6.3 kbar near the Newton window. In order to allow diffusion to completely homogenize garnets with radii from rim to core of ~800 μm such as those present in IP-19-01 (Fig. 3.37), modeling of major element diffusion by Caddick et al. (2010) requires *T* to exceed 710 °C for over 50 m.y., or higher temperatures for shorter lengths of time. Another possible interpretation is that garnet growth occurred over a protracted interval prior to peak Neoacadian metamorphism, which should allow a peak *T* of ~710 °C to cause a larger area of diffusion within these garnets. Regardless, the lack of compositional zoning in garnet from IP-19-01 indicates that garnet growth must have occurred during prograde Neoacadian metamorphism to allow for sufficient time at high *T* to drive complete diffusion of any original prograde growth zoning. This interpretation is also consistent with monazite REE distribution in this sample. Because garnet is a likely sink for HREEs, the depletion of HREEs from ~360 to 380 Ma in IP-19-01 (Fig. 3.41) could be interpreted as an indicator of garnet growth during this time.

Although the Neoacadian metamorphic mode is quite clear in the eastern Brindle Creek thrust sheet, the younger age mode is less prominent. Although it is generally accepted that the Alleghanian orogeny spans from approximately 330 – 260 Ma (Hatcher et al., 2007), the timing and spatial distribution of earliest Alleghanian metamorphism is uncertain. For example, some studies have interpreted ~325 Ma as the start of the

Alleghanian (e.g. Merschat et al., 2009). In the Brindle Creek thrust sheet, Merschat et al. (2017) reported U-Pb metamorphic zircon ages of 324 – 314 near the CPS in North and South Carolina. Merschat (2009) also reported a slightly discordant U-Pb metamorphic zircon age of 324 Ma from within the Newton window, indicating that Alleghanian metamorphism impacted both within and surrounding the Newton window. Metamorphism is interpreted to have reached upper greenschist to amphibolite facies conditions in the early Alleghanian then cooled to lower greenschist facies conditions by the late Alleghanian (Dallmeyer et al., 1986; Gilliam 2010; Merschat et al., 2017). Some interpret the early Alleghanian metamorphic event in the IP to involve reheating following post-Neoacadian cooling, however this early Alleghanian metamorphism may instead represent continuous cooling following the peak of Neoacadian metamorphism. Furthermore, the IP is also interpreted to have reached upper greenschist to amphibolite facies metamorphic conditions in the early Alleghanian that cooled to lower greenschist facies conditions by the late Alleghanian (Dallmeyer et al., 1986; Gilliam 2010; Merschat et al., 2017). However, hornblende $^{40}Ar/^{39}Ar$ cooling ages of 377 Ma near the BCFZ and 344 – 320 Ma in the central and eastern Brindle Creek thrust sheet have been reported, suggesting either regional cooling that progressed from the BCFZ towards the CPS following Neoacadian metamorphism or late exhumation (Spencer et al., 2021). Additionally, Merschat and Kalbas (2002) suggest that garnet in the Brindle Creek thrust sheet/eastern IP grew during a single event of prograde metamorphism.

Garnet in IP-19-01 is anhedral (Fig. 3.36) consistent with retrograde garnet resorption. This is consistent with the observation that garnet in this sample has thin rims of enriched Mn and Ca, which are likely the result of back-reaction into the rim following garnet breakdown (Fig. 3.37) (Tracy, 1982; Kohn and Spear, 2000). These thin rims in garnet suggest two possible interpretations: (1) a short time period of garnet breakdown that occurred at high temperature, allowing for rapid diffusion of released Fe, Mg, Ca, and Mn into or out of the rims, or (2) a long period of garnet breakdown that would allow for slow diffusion of major elements into and out of the rim at lower temperatures, which suggests a retrograde metamorphic event captured in young monazite ages in IP-19-01. The core of garnet in this sample also shows homogenous zoning (Fig. 3.37), indicating

that any previously recorded prograde growth zoning that may have been present has been lost due to internal diffusion of major elements.

In sample IP-19-01, the younger peak yields a concordia age and weighted mean age of 333 ± 1.3 (Fig. 3.39), which is consistent with the early Alleghanian metamorphic record in the eastern Brindle Creek thrust sheet. If prograde metamorphism and garnet growth occurred during the Alleghanian, existing garnet would develop a concentric zoning pattern, with homogenous zoning in the core from high Neoacadian temperatures and prograde Alleghanian growth in the rims. This pattern is absent from IP-19-01, as rims show retrograde zoning (Tracy, 1982, Kohn and Spear, 2000), indicating either that prograde garnet growth did not occur in the eastern half of the Brindle Creek thrust sheet during the Alleghanian, or that Alleghanian temperatures were high enough to homogenize all garnet zoning. Given a peak metamorphic age in IP-19-01 of 333 Ma as well as hornblende $^{40}Ar/^{39}Ar$ ages from a nearby sample of 320 Ma (Spencer et al., 2021), if prograde conditions occurred during the Alleghanian, they would likely be less than ~10 m.y. in duration. At 10 m.y., the modeling of major element diffusion by Caddick et al. (2010) suggests that temperatures of ≥770 °C are necessary to completely diffuse major elements in garnet with up to 800 μm radii, such as those present in IP-19-01. Furthermore, 10 m.y. of prograde conditions at these temperatures is highly unlikely given the nearby 320 Ma hornblende $^{40}Ar/^{39}Ar$ age, as this would require over 200 °C of cooling over a very short time interval. REE distribution from monazite analyses also show a continuous transition from relative depletion of HREEs to relative enrichment (Fig. 3.41), which may suggest a transition from garnet growth conditions between 380 and 360 Ma, to garnet breakdown conditions by 338 Ma. Thus, we interpret the metamorphic event with a peak at 333 Ma in monazite from IP-19-01 as recording retrograde metamorphism in the earliest Alleghanian near the CPS.

4.3 Implications for the significance of the Brevard fault zone

The BFZ represents perhaps the most significant structural boundary in the southern Appalachian orogen (Hatcher, 2001; Merschat et al., 2005; Hatcher and Merschat 2006; Hatcher et al., 2017). In the escape flow models proposed by Merschat et

al. (2005) and Hatcher and Merschat (2006), the BFZ is hypothesized to act as a relatively cold, rheologically stiff buttress that drives the orogen-normal northwest flow to the southeast, allowing the material to escape the collision zone during Neoacadian orogenesis. In the immediate footwall of the BFZ, sample BR-20-14 records greenschist facies conditions and Taconic metamorphic event (462 ± 2 Ma); no evidence of Neoacadian or younger monazite growth is preserved. This is interpreted to indicate that in this area, the footwall of the BFZ did not experience a major thermal-metamorphic Neoacadian event and was thus likely colder than the thrust sheets to the east. This interpretation is further supported by hornblende $^{40}Ar/^{39}Ar$ ages of 380 Ma reported from near Spruce Pine, NC, in the CHMGL thrust sheet as well as 496 Ma from the Grandfather Mountain window (Spencer et al., 2021).

To the north, another BFZ footwall sample (BR-20-10) does preserve a Neoacadian peak (339 ± 2, Table 1) in the monazite age distribution, indicating that the BFZ footwall does experience a Neoacadian thermal-metamorphic event to the north. However, this Neoacadian metamorphic is currently not recognized in the BFZ footwall to the south (Abbott and Raymond, 1984, M3 metamorphic event; Merschat, 2009). Given that the IP is known to have reached well into sillimanite grade metamorphic conditions during the Neoacadian (Bier et al., 2002; Merschat and Kalbas, 2002; Merschat, 2003; Wilson, 2006; Gatewood, 2007; Hatcher et al., 2007; Gilliam, 2010; Merschat et al., 2017), the record of Taconic metamorphism in the IP was likely overwritten during high-grade Neoacadian metamorphism. The fact that this has not occurred throughout the entire eastern BR, as well as the presence of Taconic ages within the BFZ, suggests that there was a significant thermal gradient across the BFZ during the Neoacadian.

Given that temperature is one of the primary influencers on rock rheology, a Neoacadian thermal gradient across the BFZ likely also creates a rheological gradient during this time. In the context of southern Appalachian channel flow, a rheological boundary at the BFZ would support the interpretations of Merschat et al. (2005) and Hatcher and Merschat (2006) that the BFZ acted as a buttress to channel flow, because of the high *T* and low viscosity requirements to maintain conditions conducive to channel

flow (Beaumont et al., 2004; Jamieson et al., 2004). A thermal and rheological boundary along the BFZ would prevent a migrating channel from intruding into the BR and instead force channel material to be forced to the southwest, the path of least resistance. This is also further supported by the observation of Taconic ages in BFZ rocks, possibly indicating that the high *T* metamorphism that removed Taconic ages from dateable phases in the IP did not reach the BFZ. The IP is known to have an apparent inversion of metamorphic isograds, with staurolite to kyanite grade metamorphism localized along the BFZ (Reed and Bryant, 1964; Griffin, 1974; Hopson and Hatcher, 1988; Bier et al., 2002; Merschat et al., 2017), further supporting this interpretation that high *T* metamorphism was more prominent towards the center of the IP than near the BFZ.

4.4 Southern Appalachian channel flow

The curved mineral lineation pattern and subsequent interpretation of flow redirection in the IP resembles the hypothesis of escape flow and orogen-parallel extrusion in the HT orogen (Clark and Royden, 2000; Merschat et all., 2005; Hatcher and Merschat, 2006; Royden et al., 2008; Zhang et al., 2010). In the HT orogen, the cause for redirection of flow remains difficult to explain. The interpretation that a reduction of erosion led to the cessation of surficial channel extrusion in the models of Beaumont et al. (2004) and Jamieson et al. (2004) is one mechanism by which orogen-normal channel flow could be forced into orogen-parallel escape flow, however more work is necessary to understand this redirection process. In the proposed southern Appalachian channel, flow redirection is suggested to have occurred from a combination of oblique collision during orogenesis and buttressing of flow from the BFZ (Merschat et al., 2005; Hatcher and Merschat, 2006), which is supported by the results of this study. Thus, buttressing of channel flow by colder, harder rocks serves as a valid mechanism by which orogen-normal channel flow can be redirected to orogen-parallel escape flow. Though there are differences between the interpreted channel flow in the southern Appalachians and in the HT orogen (e.g. oblique collision in the southern Appalachians and direct collision in the HT orogen, Larson et al., 1999), this result is particularly important for the HT orogen because a similar buttressing effect may have occurred after recent activation of the Main

Boundary and Main Frontal thrusts (Avouac, 2015), which may have caused deformation to transition towards critical wedge mechanics. In this case, accumulation of material into a wedge would have acted as a buttress to further channel flow, forcing the switch to escape flow. Though this is still a hypothesis that requires further scrutiny and testing, the conclusion that buttressing of orogen-normal channel flow is likely responsible for flow redirection in the southern Appalachian IP indicates that this conclusion may be valid in other orogenic systems.

4.5 Future research

Though this contribution places constraints on the extent of Paleozoic metamorphism in the BR and IP of northwestern NC, there remains opportunity for further study regarding southern Appalachian channel flow. For example, *P-T* conditions used to provide context for the interpretations in this study come from existing literature. Calculating *P-T* conditions using minerals from the same samples as monazite ages would allow for more accurate interpretations of monazite ages, mineral textures, and garnet compositions. Furthermore, though major element compositions were analyzed from garnet in most samples in this study, trace element analyses of garnet would be particularly useful in more accurately linking monazite compositions and ages to garnet growth and decay phases. In particular, observing Y zoning in garnet would be useful in understanding the interactions between garnet, monazite, and xenotime. Additionally, a necessary next step is to improve the quality of age mode separation in samples to quantitatively separate peaks rather than use troughs in KDE plots.

Although this study lays the groundwork necessary to test the channel flow hypothesis in the IP, it is limited in that it does not conclusively support or refute the IP being an exhumed orogenic channel. Ongoing work is being done to build upon the results of this study; notably, numerous hornblende $^{40}Ar/^{39}Ar$ ages are being analyzed from various structural positions throughout the BR and IP, which will allow for tighter constraints on the end of high temperature metamorphic conditions in each thrust sheet of importance. This will be particularly useful considering that channel flow requires high *T* for long residence times (>35 m.y.: Jamieson et al., 2004). Additionally, ongoing work

will apply quartz piezometry coupled with electron backscatter diffraction to define the stress conditions of the IP and BR. This will further test the interpretation of the BFZ acting as a buttress to flow, while also testing that the IP met stress conditions conducive to channel flow during the Neoacadian. Finally, because this study is primarily focused on the northernmost extent of the IP and the interpreted channel was redirected to flow towards the SW, further work is necessary to determine the extent of metamorphism from each major Paleozoic orogeny further south in the BR and IP. In the Alabama BR, for example, Alleghanian garnet growth has been documented (e.g., Stowell et al., 2019) suggesting differences in metamorphism during Paleozoic orogenesis along strike.

4.6 Conclusions

We present constraints on the spatial and temporal extent of Paleozoic metamorphism in the southern Appalachians of northwestern NC. The CHMGL thrust sheet records mostly Taconic metamorphism with some Neoacadian metamorphism in northwestern NC. In the southern Appalachians of northwestern NC, there is no record of Alleghanian metamorphism except near the BFZ. The Brevard thrust sheet shows Neoacadian high temperature metamorphism but almost no Taconic metamorphism despite containing examples of Taconic magmatism and being composed of similar lithology to the CHMGL thrust sheet. Therefore, unlike the CHMGL thrust sheet, the Taconic metamorphic record that was almost certainly present at one point in the Brevard thrust sheet was most likely completely overwritten by high *T* Neoacadian metamorphism. This distinguishes the Brevard thrust sheet from CHMGL thrust sheet, indicating that the BFZ acted as a thermal (and likely also rheological) boundary during the Neoacadian, with higher temperature metamorphism limited to east of the BFZ in the IP. Neoacadian metamorphism within the Sauratown Mountains window does not show the same high *T* as in the IP, suggesting that during the Neoacadian, high *T* did not penetrate fully from the IP into structurally lower units.

The Brindle Creek thrust sheet records mostly Neoacadian metamorphism, though retrograde Alleghanian metamorphism is present only near the CPS. In northwestern NC, the Brindle Creek thrust sheet supports earlier interpretations that the IP records a single

prograde metamorphic event. Emplacement of the Brindle Creek thrust sheet occurred while the thrust sheet was at very high *T*, which may have led to some aspect of heat transfer from the Brindle Creek thrust sheet to the Brevard thrust sheet upon emplacement. This is supported by a slightly earlier onset of Neoacadian metamorphism in the Brindle Creek thrust sheet than the Brevard thrust sheet, as well as garnet within the Brindle Creek thrust sheet that shows evidence of retrograde metamorphism that likely occurred at during the middle to late Neoacadian. Further research is necessary to determine if the IP satisfies conditions necessary to be considered an orogenic channel, however this study provides the groundwork for doing so by constraining the Alleghanian record primarily to the easternmost IP, allowing for future work to assess Neoacadian metamorphic conditions in the IP and BR.

REFERENCES

Abbott, R.N., Jr., and Raymond, L.A. 1984. The Ashe metamorphic suite, northwest North Carolina: Metamorphism and observations on geologic history: American Journal of Science, v. 284, p. 350–375, doi:10.2475/ajs.284.4-5.350.

Avouac, J.P. 2015. Mountain Building: From Earthquakes to Geologic Deformation, in Schubert, G, (ed.) *Treatise on Geophysics*, v. 6, p. 381-432.

Bai, D., Unsworth, M.J., Meju, M.A., Ma, X., Teng, J., Kong, X., Sun, Y., Sun, J., Wang, L., Jiang, C., Zhao, C., Xiao, P. and Liu, M. 2010. Crustal deformation of the eastern Tibetan plateau revealed by magnetotelluric imaging: Nature Geoscience, doi:10.1038/NGEO830.

Beaumont, C., Jamieson, R.A., Nguyen, M.H. and Lee, B. 2001. Himalayan tectonics explained by extrusion of a low-viscosity channel coupled to focused surface denudation: Nature, v. 414, p. 738-742.

Beaumont, C., Jamieson, R.A., Nguyen, M.H. and Medvedev, S. 2004. Crustal channel flows: 1. Numerical models with application to the tectonics of the Himalayan-Tibetan orogen: Journal of Geophysical Research, v. 109, dx.doi.org/10.1029/2003JB002809.

Bier, S.E., Bream, B.R., and Giorgis, S.D. 2002. Inner Piedmont stratigraphy, metamorphism, and deformation in the Marion–South Mountains area, North Carolina, in Hatcher, R.D., Jr., and Bream, B.R., eds., Inner Piedmont Geology in the South Mountains–Blue Ridge Foothills and the Southwestern Brushy Mountains, Central-Western North Carolina: Raleigh, North Carolina Geological Survey, Carolina Geological Society Annual Field Trip Guidebook, 19-20 October 2002, p. 65-100.

Bond, P.A., and Fullagar, P.D. 1974. Origin and age of the Henderson Augen gneiss and associated cataclastic rocks in southwestern North Carolina. Geological Society of America Abstracts with Programs. v. 6, p. 336

Bream, B.R. 2002. The southern Appalachian Inner Piedmont: New perspectives based on recent detailed geologic mapping, Nd isotopic evidence, and zircon geochronology, in Hatcher, R.D., Jr., and Bream, B.R., eds., Inner Piedmont Geology in the South Mountains–Blue Ridge Foothills and the Southwestern Brushy Mountains, Central-Western North Carolina: Raleigh, North Carolina Geological Survey, Carolina Geological Society Annual Field Trip Guidebook, 19-20 October 2002, p. 45-63.

Bream, B.R. 2003. Tectonic implications of geochronology and geochemistry of para- and orthogneisses from the southern Appalachian crystalline core [Ph. D. dissertation]: Knoxville, University of Tennessee 310 p.

Bream, B.R., Hatcher, R.D., Jr., Miller, C.F., and Fullagar, P.D. 2004. Detrital zircon ages and Nd isotopic data from the southern Appalachian crystalline core, Georgia, South Carolina, North Carolina, and Tennessee: New provenance constraints for Laurentian margin paragneisses, in Tollo, R.P., Corriveau, L., McLelland, J., and Bartholomew, M.J., eds., Proterozoic Evolution of the Grenville Orogen in North America: Geological Society of America Memoir 197, p. 459-475, doi:10.1130/0-8137-1197-5.459.

Broska, I., Williams, C.T., Janak, M., Nagy, G. 2005. Alteration and breakdown of xenotime-(Y) and monazite-(Ce) in granitic rocks of the Western Carpathians, Slovakia. Lithos 82, 71–83.

Byars, H. E. 2010, Tectonic evolution of the west-central portion of the Newton window, North Carolina Inner Piedmont: Timing and implications for the emplacement of the Paleozoic Vale charnockite, Walker Top Granite, and mafic complexes [M.S. Thesis]: Knoxville, Tennessee, University of Tennessee, M. S. thesis, 248 p.

Caddick, M. J., Konopasek, J. & Thompson, A. B. 2010. Preservation of garnet growth zoning and the duration of prograde metamorphism. Journal of Petrology, v. 51, p. 2327–2347.

Catlos, E.J., Harrison, T.M., Kohn, M.J., Grove, M., Ryerson, F.J., Manning, C.E., Upreti, B.N. 2001. Geochronologic and thermobarometric constraints on the

evolution of the Main Central Thrust, central Nepal Himalaya. Journal of Geophysical Research, B, Solid Earth and Planets, v. 106, p. 16,177-16,204.

Clark, M.C. and Royden, L.H. 2000. Topographic ooze: building the eastern margin of Tibet by lower crustal flow: Geology, v. 28, p. 703-706, doi.org/10.1130/0091-7613(2000)28<703.

Clark, M.K., Bush, J.W.M. and Royden, L.H. 2005. Dynamic topography produced by lower crustal flow against rheological strength heterogeneities bordering the Tibetan Plateau: Geophysical Journal International, v. 162, p. 575-590, doi:10.1111/j.1365-246X.2005.02580.x.

Clark, H.B., Costain, J.K., and Glover, L., III, 1978, Structural and seismic reflection studies of the Brevard ductile deformation zone near Rosman, North Carolina: American Journal of Science, v. 278, p. 419–441.

Corrie S. Kohn M.J., 2008, Trace-element distribution in silicates during prograde metamorphic reactions: Implications for monazite formation: Journal of Metamorphic Geology , v. 26, no. 4, p. 451–464, doi:10.1111/j.1525-1314.2008.00769.x.

Cottle, J.M., Larson, K.P. and Kellett, D.A. 2015. How does the mid-crust accommodate deformation in large, hot collisional orogens? A review of recent research in the Himalayan orogen: Journal of Structural Geology, v. 78, p. 119-133, dx.doi.org/10.1016/j.jsg.2015.06.008.

Cottle, J.M., Jessup, M.J., Newell, D.L., Searle, M.P., Law, R.D., and Horstwood, M.S.A. 2007. Structural insights into the early stages of exhumation along an orogen-scale detachment: the South Tibetan Detachment System, Dzakaa Chu section, Eastern Himalaya: Journal of Structural Geology, v. 29, p. 1781-1797, http://dx.doi.org/10.1016/j.jsg.2007.08.007.

Dallmeyer, R.D. 1988. Late Paleozoic tectonothermal evolution of the western Piedmont and eastern Blue Ridge, Georgia: Controls on the chronology of terrane accretion

and transport in the southern Appalachian orogen: Geological Society of America Bulletin, v. 100, p. 702-713, doi:10.1130/0016-7606(1988)1002.3.CO;2.

Dallmeyer, R.D., Wright, J.E., Secor Jr, D.T., and Snoke, A.W., 1986, Character of the Alleghanian orogeny in the southern Appalachians: II: Geochronological constraints on the tectonothermal evolution of the eastern Piedmont in South Carolina: Geological Society of America Bulletin, v. 97, p. 1329–1344.

Davis, T.L. 1993. Lithostratigraphy, Structure, and Metamorphism of a Crystalline Thrust Terrane, Western Inner Piedmont, North Carolina [Ph.D. diss.]: Knoxville, Tennessee, University of Tennessee, 245 p.

Eckert, J. O., Jr.; Hatcher, R. D., Jr.; and Mohr, D. W. 1989. The Wayah granulite-facies metamorphic core, southwestern North Carolina: high grade culmination of Taconic metamorphism in the southern Blue Ridge. Geological Society of America Bulletin, v. 101, p. 749–762.

Edelman, S.H., Liu, A., and Hatcher, R.D., Jr. 1987. The Brevard zone in South Carolina and adjacent areas: An Alleghanian orogen-scale dextral shear zone reactivated as a thrust fault: The Journal of Geology, v. 95, p. 793–806.

Edwards, M.A., Harrison, T.M. 1997. When did the roof collapse? Late Miocene north-south extension in the high Himalaya revealed by Th-Pb monazite dating of the Khula Kangri granite. Geology, v. 25, p. 543-546.

Finger, F., Broska, I., Roberts, M.P., Schermaier, A., 1998. Replacement of primary monazite by apatite–allanite–epidote coronas in an amphibolites facies granite gneissfrom the eastern Alps. American Mineralogist 83, 248–258.

Gatewood, M.P. 2007. Structure and tectonics of the northeastern Inner Piedmont from detailed geologic mapping, geochronologic, geochemical, and petrologic studies with macro-, meso-, and microstructural analyses of ductile fault zones [M.S. thesis]: Knoxville, University of Tennessee.

Gatewood, M.P., Dragovic, B., Stowell, H.H., Baxter, E.F., Hirsch, D.M. & Bloom, R. 2015. Evaluating chemical equilibrium in metamorphic rocks using major element

and Sm–Nd isotopic zoning in garnet, Townshend Dam, Vermont, USA. Chemical Geology, v. 401, p. 151–168.

Gerbault, M., Martinod, M., and Hérail., G. 2005. Possible orogeny-parallel lower crustal flow and thickening in the central Andes, Tectonophysics, v. 399, p. 59-72, doi:10.1016/j.tecto.2004.12.015.

Gilliam, W.G. 2010. Structural and Metamorphic Evolution of the West-Central Newton Window Eastern Inner Piedmont, North Carolina [M.S. thesis]: Knoxville, Tennessee, University of Tennessee, 142 p.

Goldberg, S.A., and Dallmeyer, R.D. 1997. Chronology of Paleozoic metamorphism and deformation in the Blue Ridge thrust complex, North Carolina and Tennessee: American Journal of Science, v. 297, p. 488-526, doi:10.2475/ajs.297.5.488.

Griffin Jr., V.S., 1974. Analysis of the Piedmont in northwest South Carolina. Geological Society of America Bulletin 85, 1123–1138.

Grujic, D., Hollister, L. and Parrish, R.R. 2002. Himalayan metamorphic sequence as an orogenic channel: insight from Bhutan: Earth and Planetary Science Letters, v. 198, p. 177-191.

Grujic, D., Casey, M., Davidson, C., Hollister, L.S., Kundig, R., Pavlis, T., and Schmid, S. 1996. Ductile extrusion of the Higher Himalayan crystaline in Bhutan: Evidence from quartz microfabrics, Tectonophysics, v. 260, p. 21-43.

Hatcher, R.D., Jr. 1971. Geology of Rabun and Habesham counties, Georgia: A reconnaissance study, Georgia Geological Survey Bulletin, 83-A, 1-48.

Hatcher, R.D., Jr. 1972. Developmental model for the southern Appalachians: Geological Society of America Bulletin, v. 83, p. 2735-2760

Hatcher, R.D., Jr., 1988, Sauratown Mountains window - problems and regional perspective, in Hatcher, A.D., Jr., ed., Structure of the Sauratown Mountains window, North Carolina: Carolina Geological Society Guidebook, p. 51-66.

Hatcher, R.D., Jr. 2001. Rheological partitioning during multiple reactivation of the Paleozoic Brevard fault zone, southern Appalachians, USA, in Holdsworth, R.E., Strachan, R.A., Magloughlin, J.F., and Knipe, R.J., eds., The Nature and Tectonic Significance of Fault Zone Weakening: Geological Society, London, Special Publication 186, p. 255–269.

Hatcher, R.D., Jr. 2002. Alleghanian (Appalachian) orogeny, a product of zipper tectonics: Rotational transpressive continent-continent collision and closing of ancient oceans along irregular margins, in Martínez Catalán, J.R., Hatcher, R.D., Jr., Arenas, R., and Díaz García, F., eds., Variscan-Appalachian Dynamics: The Building of the Late Paleozoic Basement: Geological Society of America Special Paper 364, p. 199–208, doi:10.1130/0-8137-2364-7.199.

Hatcher, R.D., Jr. 2005. Southern and central Appalachians, in Selley, R. C., Cocks, L. R. M., and Plimer, I. R. eds., Encyclopedia of geology, Elsevier Academic Press, Amsterdam, p. 72–81.

Hatcher, R.D., Jr., and Merschat, A.J. 2006. The Appalachian Inner Piedmont: An exhumed strike-parallel, tectonically forced orogenic channel, in Law, R.D., Searle, M., and Godin, L., eds., Channel Flow, Ductile Extrusion and Exhumation of Lower-Mid Crust in Continental Collision Zones: Geological Society, London, Special Publication 268, p. 517–540, doi:10.1144/GSL.SP.2006.268.01.24.

Hatcher, R.D., Jr., Bream, B.R., and Merschat, A.J. 2007. Tectonic map of the southern and central Appalachians: A tale of three orogens and a complete Wilson cycle, in Hatcher, R.D., Jr., Carlson, M.P., McBride, J.H., and Martínez Catalán, J.R., eds., 4-D Framework of Continental Crust: Geological Society of America Memoir 200, p. 595–632.

Hatcher Jr., R. D., Huebner, M. T., Rehrer, J. R., Acker, L. L., Fullagar, P. D., Liu, A., and Goad, P. L. 2017. Geologic and kinematic insights from far-traveled horses in the Brevard fault zone, southern Appalachians, in Law, R. D., Thigpen, J. R., Merschat, A. J., and Stowell, H. H., editors, Linkages and Feedbacks in Orogenic

Systems: Geological Society of America Memoir 213, p. 313–351, https://doi.org/10.1130/2017.1213(13)

Hodges K.V. 2006. A synthesis of the channel flow–extrusion hypothesis as developed for the Himalayan-Tibetan orogenic system, in Law R.D. Searle M.P. Godin L., eds., Channel Flow, Ductile Extrusion and Exhumation of Lower Mid-Crust in Continental Collision Zones: Geological Society of London Special Publication 268, p. 71–90.

Hopson, J.L., Hatcher Jr., R.D., 1988. Structural and stratigraphic setting of the Alto Allochthon, NE Georgia. Geological Society of America Bulletin v. 100, p. 339–350.

Jamieson, R.A., Beaumont, C., Medvedev, S., and Nguyen, M.H. 2004. Crustal channel flows: 2. Numerical models with implications for metamorphism in the Himalayan-Tibetan orogen. Journal of Geophysical Research, v. 109, http://dx.doi.org/10.1029/2003JB002811.

Kalbas, J. L., 2003, Geology of part of the southwestern Brushy Mountains, Inner Piedmont [M.S. thesis]: Knoxville, University of Tennessee, 208 p

Karabinos P. and Ketcham R. 1988. Thermal structure of active thrust belts. Journal of Metamorphic Geology, v. 6, p. 559–570.

Kohn, M. J. & Spear, F. S. 2000. Retrograde net transfer reaction insurance for pressure–temperature estimates. Geology, v. 28, p. 1127–1130.

Kylander-Clark, A.R.C., Hacker, B.R., and Cottle, J.M. 2013. Laser-ablation split-stream ICP petrochronology: Chemical Geology, v. 345, p. 99–112, doi:10.1016/j.chemgeo.2013.02.019.

Larson, K. M., Burgmann, R., Bilham, R., and Freymueller, J. T. 1999. Kinematics of the India-Eurasia collision zone from GPS measurements, Journal of Geophysical Research, v. 104, p. 1077–1093.

Levine, J. S. F., Merschat, A. J., McAleer, R. J., Casale, G., Quillan, K. R., Fraser, K. I., & BeDell, T. G. 2018. Kinematic, deformational, and thermochronologic

conditions along the Gossan Lead and Fries shear zones: Constraining the western-eastern Blue Ridge boundary in northwestern North Carolina. Tectonics, 37(10), 3500–3523. https://doi.org/10.1029/2017TC004879.

Levine J. S.F., Casale. G, McAleer, R. J., Merschat, A. J., and Powell, N. E. 2020. The Alleghanian Orogeny in the eastern Blue Ridge: Earlier and hotter than previously recognized: Geological Society of America Abstracts with Programs, v. 52, no. 6.

McConnell, K. I., 1988, Geology of the Sauratown Mountains anticlinorium: Vienna and Pinnacle 7.5 minute quadrangles, in Hatcher, A.D., Jr., ed., Structure of the Sauratown Mountains window, North Carolina: Carolina Geological Society Guidebook, p. 51-66.

Merschat, A. J., 2003, Inner Piedmont tectonics in the southwestern Brushy Mountains, North Carolina, Field and laboratory data revealing 3-D crustal flow and sillimanite I and II metamorphism [M.S. thesis]: Knoxville, University of Tennessee, 201 p.

Merschat, A.J. 2009. Assembling the Blue Ridge and Inner Piedmont: Insights into the Nature and Timing of Terrane Accretion in the Southern Appalachian Orogen from Geologic Mapping, Stratigraphy, Kinematic Analysis, Petrology, Geochemistry, and Modern Geochronology [Ph.D. dissertation]: Knoxville, Tennessee, University of Tennessee, 455 p.

Merschat, A.J., and Kalbas, J.L. 2002. Geology of the southwestern Brushy Mountains, North Carolina Inner Piedmont: A summary and synthesis of recent studies, in Hatcher, R.D., Jr., and Bream, B.R., eds., Inner Piedmont Geology in the South Mountains–Blue Ridge foothills and the Southwestern Brushy Mountains, Central-Western North Carolina: Raleigh, North Carolina Geological Survey, Carolina Geological Society Annual Field Trip Guidebook, 19–20 October 2002, p. 101–126.

Merschat, A.J., Hatcher, R.D., Jr., and Davis, T.L. 2005. The northern Inner Piedmont, southern Appalachians, USA: Kinematics of transpression and SW-directed mid-

crustal flow: Journal of Structural Geology, v. 27, p. 1252–1281, doi:10.1016/j.jsg.2004.08.005.

Merschat, A.J., Hatcher, R.D., Jr., Byars, H.E., and Gilliam, W.G. 2012. The Neoacadian orogenic core of the southern Appalachians: A geo-traverse through the migmatitic Inner Piedmont from the Brushy Mountains to Lincolnton, North Carolina, in Eppes, M.C., and Bartholomew, M.J., eds., From the Blue Ridge to the Coastal Plain: Field Excursions in the Southeastern United States: Geological Society of America Field Guide 29, p. 171–217, doi:10.1130/2012.0029(06).

Merschat, A.J., Bream, B.R., Huebner, M.T., Hatcher, R.D., Jr, and Miller, C.F. 2017. Temporal and spatial distribution of Paleozoic metamorphism in the Southern Appalachian Blue Ridge and Inner Piedmont delimited by ion microprobe U-Pb ages of metamorphic zircon, in Law, R., Thigpen, R., Merschat, A., and Stowell, H., eds., Linkages and Feedbacks in Orogenic Systems: Geological Society of America Memoir 213, p. 199–254, doi:10.1130/2017.1213(10).

Meschter McDowell, S., Miller, C.F., Fullagar, P.D., Bream, B.R., and Mapes, R.W. 2002. The Persimmon Creek Gneiss, eastern Blue Ridge, North Carolina–Georgia: Evidence for the missing Taconic arc?: Southeastern Geology, v. 41, p. 103–117.

Miller, B.V., Fetter, A.H., and Stewart, K.G. 2006. Plutonism in three orogenic pulses, eastern Blue Ridge Province, southern Appalachians: Geological Society of America Bulletin, v. 118, p. 171–184, doi:10.1130/B25580.1.

Miller, B.V., Stewart, K.G., and Whitney, D.L. 2010. Three tectonothermal pulses recorded in eclogite and amphibolite of the eastern Blue Ridge, southern Appalachians, in Tollo, R.P., Bartholomew, M.J., Hibbard, J.P., and Karabinos, P.M., eds., From Rodinia to Pangea: The Lithotectonic Record of the Appalachian Region: Geological Society of America Memoir 206, p. 701–724, doi:10.1130/2010.1206(27).

Miller, C.F., Hatcher, R.D., Jr., Ayers, J.C., Coath, C.D., and Harrison, T.M. 2000. Age and zircon inheritance of eastern Blue Ridge plutons, southwestern North

Carolina and northeastern Georgia, with implications for magma history and evolution of the southern Appalachian orogen: American Journal of Science, v. 300, p. 142–172, doi:10.2475/ajs.300.2.142

Nelson, K.D., Zha Nelson, K.D., Zhao, W., Brown, L.D., Kuo, J., Che, J., Liu, X., Klemperer, S.L., Makovsky, Y., Meissner, R., Mechie, J., Kind, R., Wenzel, F., Ni, J., Nabelek, J., Leshou, C., Tan, H., Wei, W., Jones, A.G., Booker, J., Unsworth, M., Kidd, W.S.F., Hauck, M., Alsdorf, D., Ross, A., Cogan, M., Wu, C., Sandvol, E. and Edwards, M. 1996. Partially molten middle crust beneath southern Tibet: A synthesis of Project INDEPTH results: Science, v. 274, p. 1684–1688, doi:10.1126/science.274.5293.1684.

Odom, A.L., and Fullagar, P.D., 1973. Geochronologic and tectonic relationships between the Inner Piedmont, Brevard zone, and Blue Ridge belts, North Carolina: American Journal of Science, v. 273-A, p. 133-149.

Raimondo, T., Collins, A.S., Hand, M., Walker-Hallam, A., Smithies, R.H., Evins, P.M., and Howard, H.M. 2009. Ediacaran intracontinental channel flow: Geology, v. 37, no. 4, p. 291–294, http://dx.doi.org/10.1130/G25452A.1

Reed, J.C., Jr., and Bryant, B. 1964. Evidence for strike-slip faulting along the Brevard zone in North Carolina: Geological Society of America Bulletin, v. 75, p. 1177–1196, doi:10.1130/0016-7606(1964)75[1177:EFSFAT]2.0 .CO;2.

Roper, P.J. & Dunn, D.E. 1973. Superposed deformation and polymetamorphism, Brevard zone, South Carolina. Geological Society of America Bulletin, 84, 3373-3386.

Roper, P.J. and Justus, P.S. 1973. Polytectonic evolution of the Brevard fault zone: American Journal of Science, v. 273A, p. 105-132.

Royden L.H., Burchfiel B.C., van der Hilst R.D. 2008. The geological evolution of the Tibetan Plateau: Science, v. 321, p. 1054–1058 doi:10.1126/science.1155371.

Russell, G.S., Russell, C.W., Farrar, S.S., 1985. Alleghanian deformation and metamorphism in the eastern North Carolina Piedmont: Geological Society of America Bulletin, v .96, p. 381–387.

Searle, M. P., and Szulc A. G. 2005. Channel flow and ductile extrusion of the High Himalayan slab: The Kangchenjunga-Darjeeling profile, Sikkim Himalaya, J. Asian Earth Sci., v. 25, p. 173–185.

Sinha, A. K. & Glover, L., III, 1978: U-Pb systematics of zircons during dynamic metamorphism - a study from the Brevard Fault zone. Contributions to Mineralogy and Petrology, v. 66, p. 305–310.

Sinha, A. K., Hewitt, D. A., and Rimstidt, J. D., 1988, Metamorphic petrology and strontium isotope geochemistry associated with the development of mylonite: an example from the Brevard fault zone, South Carolina: American Journal of Science, v. 288, p. 155–147.

Spear, F. S, and Pyle J. M. 2002. Apatite, monazite, and xenotime in metamorphic rocks. See Kohn et al. 2002, p. 293–335

Spencer, B. M., Thigpen, J. R., Merschat, A., Powell, N. E., McDonald, C. S., 2021, Deciphering the "Footprint" of the Neoacadian Metamorphic Event in the Southern Appalachians: Insights from $^{40}Ar/^{39}Ar$ Geochronology in the Eastern Blue Ridge and Inner Piedmont of North Carolina, Geological Society of America Abstracts with Programs, v. 53, no. 2.

Stacey J.S., Kramers J.D. 1975. Approximation of terrestrial lead isotope evolution by a two-stage model: Earth Planet Sci. Lett., v. 26, p. 207-221.

Stevens, L.M., Baldwin, J.A., Cottle, J.M., & Kylander-Clark, A.R.C. 2015. Phase equilibria modelling and LASS monazite petrochronology: P–T–t constraints on the evolution of the Priest River core complex, northern Idaho. Journal of Metamorphic Geology, v. 334, p. 385-411. doi: 10.1111/jmg.12125

Stowell, H.H, Schwartz, J.J., Ingram, S.B. III, Madden, J., Jernigan, C., Steltenpohl, M., Mueller, P. 2019. Linking metamorphism, magma generation, and synorogenic

sedimentation to crustal thickening during Southern Appalachian mountain building, USA. Lithosphere, v. 11, no. 5, p. 722-749.

Sun, S.-s., & McDonough, W. F. 1989. Chemical and isotopic systematics of oceanic basalts: implications for mantle composition and processes. Geological Society, London, Special Publications, v. 42, no. 1, p. 313-345. doi:10.1144/gsl.Sp.1989.042.01.19

Tracy, R.J., 1982. Compositional zoning and inclusions in metamorphic minerals. In: Ferry, J.M. (Ed.), Characterization of Metamorphism through Mineral Equilibria, Rev. Mineral., vol. 10, pp. 355 – 397.

Trupe, C.H., Stewart, K.G., Adams, M.G., Waters, C.L., Miller, B.V., and Hewitt, L.K. 2003. The Burnsville fault: Evidence for the timing and kinematics of southern Appalachian Acadian dextral transform tectonics: Geological Society of America Bulletin, v. 115, p. 1365–1376, doi:10.1130/B25256.1.

Unsworth, M. J., Jones, A. G., Wei, W., Marquis, G., Gokarn, S. G., Spratt, J. E. and the INDEPTH-MT Team. 2005. Crustal rheology of the Himalaya and southern Tibet inferred from magnetotelluric data: Nature, v. 438, p. 78–81, doi:10.1038/nature04154.

Vermeesch, P. 2018. IsoplotR: a free and open toolbox for geochronology. Geosci. Front. https://doi.org/10.1016/j.gsf.2018.04.001.

Wilson, C. G. 2006. Origin and tectonic evolution of the southern Appalachian Neoacadian crystalline core: Evidence from the geology of the Gilreath 7.5-minute quadrangle, North Carolina [M.S. thesis]: Knoxville, University of Tennessee, 219 p.

Yanagihara, G. M., 1994, Structure, stratigraphy, and metamorphism of a part of the Columbus Promontory, North Carolina [M.S. thesis]: Knoxville, University of Tennessee, 214 p.

Yu, Q.-Y., Bagas, L., Yang, P.-H., & Zhang, D. 2019. GeoPyTool: A cross-platform software solution for common geological calculations and plots. Geoscience Frontiers, v. 10, no. 4, 1437-1447. doi: 10.1016/j.gsf.2018.08.001

Zhang, P.Z., Shen, Z., Wang., M., Gan, W., Burgmann, R., Molnar, P., Wang., Q., Niu, Z., Sun., J., Wu. J., Hanrong, S. and Xinzhao, Y. 2004. Continuous deformation of the Tibetan Plateau from global positioning system data: Geology, v. 32, p. 809-812, doi:10.1130/G20554.1.

Zhang Z.J., Yuan X.H., Chen Y., Tian X.B., Kind R.N., Li X.Q., Teng J.W. 2010. Seismic signature of the collision between the east Tibetan escape flow and the Sichuan Basin: Earth and Planetary Science Letters, v. 292, p. 254–264, doi:10.1016/j.epsl.2010.01.046.

VITA

Nicholas Edwin Powell

Born: Cary, North Carolina

From: Fuquay Varina, North Carolina

Education

B.S. Geology (2019)

Appalachian State University, Boone, NC

Experience

Graduate Teaching / Research Assistant

UK Structure and Geodynamics Lab

Department of Earth and Environmental Sciences

University of Kentucky, 40506

Undergraduate Teaching / Research Assistant

Department of Geological and Environmental Sciences

Appalachian State University, 28608-28607